Abiotic Methane Formation at the Dun Mountain Ophiolite, New Zealand

---

A THESIS SUBMITTED IN PARTIAL FULFILMENT

OF THE REQUIREMENTS FOR THE DEGREE OF

Master of Science in Geology

AT THE

DEPARTMENT OF GEOLOGICAL SCIENCES

UNIVERSITY OF CANTERBURY

by Joanna Frances Pawson

UNIVERSITY OF CANTERBURY

2014

Frontispiece

“I may not have gone where I intended to go, but I think I have ended up where I needed to be.”

- Douglas Adams, *The Long Dark Teatime of the Soul*

Abstract

The production of hydrogen (H_2) and methane (CH_4) related to olivine hydration (i.e. serpentinization) is considered a major contributor to abiotic hydrocarbon synthesis on Earth. Recent discoveries have highlighted the importance of low temperature (<100°C) serpentinization at continental peridotite outcrops. Such sites produce substantial fluxes of abiotic CH_4 from gas seeps and/or springs. A limited number of studies in the southern hemisphere offer research on low temperature abiotic hydrocarbon synthesis in natural ultramafic environments, though large areas of exposed ophiolite are prevalent. This study assesses the origin and flux of CH_4 and related water-rock interactions from a previously undiscovered site in the Dun Mountain Ophiolite Belt (DMOB), located at Red Hills, New Zealand. Methane emissions from a hyper-alkaline (pH >11.6) and reduced spring of calcium hydroxide (Ca^{2+}-OH^-) type waters near the Maitlands Fault were between 730 to 17,000 mg $m^{-2}day^{-1}$. The $\delta^{13}C$ and δD values of CH_4 emitting from this spring are consistent with CH_4 of abiotic origin ($\delta^{13}C$: -32.7 ‰ VPDB, δD: -363 ‰ V-SMOW). Hyper-alkaline fluids emitting from the spring are concentrated in dissolved CH_4 (2.2 mg/L) and H_2 (0.7 mg/L) and display $\delta^{13}C_{CH4}$ signatures consistent with other sites worldwide. Extensive and localised carbonate precipitation occurs at the hyper-alkaline Ca-rich spring. Isotopic evaluation of carbonate nodules are kinetically fractionated with ^{13}C and ^{18}O depletions up to 30.8 ‰ and 9.3 ‰, respectively. This disequilibrium between the mineralogy and interacting fluids and gases represents a potential habitable environment for microorganisms. Porous, layered carbonates located on the outer edges of the hyper-alkaline spring are the result of atmospheric CO_2 interaction with magnesium bicarbonate (Mg^{2+}-HCO_3) and Ca^{2+}-OH^- hyper-alkaline waters. The precipitation of these carbonates offers potential insight towards low temperature CO_2 sequestration. Additionally, various forms of Fe-rich amorphous material precipitate in association with Mg^{2+}-HCO_3 type waters at the Red Hills. The identification of bacteria and diatoms within this material offers supporting information regarding microbial survival in metal-rich, reduced environments. This multidisciplinary study demonstrates the interconnected nature of geological, biological and atmospheric interactions in ultramafic environments at low temperature on Earth.

Acknowledgements

I would like to extend a huge thank you to my primary supervisor Dr. Chris Oze, who has not only provided a wealth of knowledge but has sustained an unwavering, contagious passion for science and discovery. His support, patience and drive have provided much needed direction throughout my degree. To Dr. Travis Horton for sharing his diverse knowledge, for always having his door open to his students, no matter how busy he is. To Dr. Giuseppe Etiope, whose efficiency and wisdom have saved me too many times to mention. I am immensely appreciative of this support, from all areas of the globe.

I would like to acknowledge all of the technical staff on the first floor, especially Rob Spiers, Kerry Swanson, Sasha Baldwin and Matt Cockcroft, who found the equipment I needed no matter how strange the request. Also, thank you to the chemistry magicians Rob Stainthorpe and Sally Gaw and to Craig Galilee from biology, for some solid interdepartmental assistance beyond obligation.

A massive thanks to my field mules Josh Smaill, Matt Linton and Cam Asher for taking time out of their busy schedules to chase 'rock farts'. Thanks to Noel Win and Sean Freeman, for unprecedented technical IT and diatom support. A special thank you to Simon Bloomberg, for showing me the joys of the Li-cor back when this project was just twinkle in Chris's eye. And to Matt Hanson, my gas chemist encyclopaedia, for his patience in explaining even the simplest theories to me, and providing technical support beyond his duties.

To Mike Johnston and Paul Denton, who provided me with key information and initial inspiration on the Red Hills geology/history. To the kiwi tramping man, who pointed me in the right direction during preliminary field investigations. Without his acute observations I may not have found methane in the Red Hills. I hope that one day he may stumble upon this thesis and feel adequately appreciated.

I am extremely grateful for the generous funding provided to me by the Ngai Tahu Research Centre and to John Kapa and Anna Kelley from the Maori Development team for helping me out in more ways than I could have asked. Also, I would like to show my appreciation to the department of geological sciences, the Mason Trust and the office of AVC Māori for providing a substantial contribution towards undertaking my field research/analyses and presenting my findings in San Francisco.

Thank you to my best friends, my rocks, Jules and Frith, who have kept me grounded and active, and always encouraged a ‘mental health’ ski day when it was much needed. To my family, who over the years have backed me through thick and thin, not only in my studies. To my Dad, for some tight proof reading on very short notice, and for excellent chemical/mathematical guidance. A special thank you to my loving compañero Craig, for providing sustenance during all-nighters in the lab, and for dealing with my crazy ways when times were tough.

And finally, I wish to dedicate this to my incredible grandmother Rachael, who has the kindest soul I have ever encountered. We all miss you immensely.

Table of Contents

List of Tables

List of Figures

1 Introduction

The production of abiotic methane (CH_4) has been observed at mid ocean ridges and terrestrial peridotites, submarine and terrestrial ophiolites, intrusions and orogenic massifs worldwide (Etiope et al. 2011; Etiope et al. 2013a; Giggenbach & Lyon 1990; Boschetti et al. 2013; Morrill et al. 2013; Sanchez-Murillo et al. 2014; Etiope et al. 2013b; Kelley et al. 2005). One major pathway for abiotic CH_4 formation is through the process of serpentinization (i.e. the hydrolysis of ultramafic material). Serpentinzation produces hydrogen (H_2), which is then available to react with a variety of carbon sources (e.g. CO, COOH, CO_2) to produce CH_4 via Fischer Trope/Sabatier type processes (Proskurowski 2010; Etiope & Sherwood Lollar 2013) or potentially via direct synthesis (Oze & Sharma 2005; Boschetti et al. 2013; Etiope et al. 2013b).

Minerals and gases evolved during serpentinization are temperature dependent. High temperature serpentinization is common in mid-ocean environments, primarily driven by seawater-rock-magma interactions (Früh-Green et al. 2004; Holm & Charlou 2001). Studies relating to high temperature serpentinization suggest that the rate of serpentinization and H_2 production is at a maximum between 200 - 315ºC and becomes severely inhibited at temperatures below 150ºC (McCollom & Bach 2009). Additionally, the increased reaction kinetics of these high temperature systems provide a favourable environment for the abiotic synthesis of CH_4 (McCollom 2013). Alternatively, low temperature serpentinization occurring in off-axis mid-ocean ridge hydrothermal systems (e.g. Kelley et al. 2005) and terrestrial/obducted ophiolites are equally as prevalent and may provide a major geochemical route for H_2 and CH_4 production, albeit at less thermodynamically and kinetically favourable conditions (e.g. Marques et al. 2008; Etiope et al. 2013b).

Low temperature (<100 ºC) ultramafic rock and water interactions offer insight towards CH_4 formation on both present-day and early Earth. Additionally, these types of interactions may be relevant to the release of CH_4 that may be occurring on other planets such as Mars (Etiope et al. 2012; Wray & Ehlmann 2011; Schulte et al. 2006; Schoell & Etiope 2011; Oze & Sharma 2005). Laboratory experiments assessing low temperature serpentinization (Neubeck et al. 2011; Neubeck et al. 2014; McCollom 2013) have constrained potential thermodynamic and mineralogical controls on H_2 and concurrent CH_4 production. These experiments assess the variation in H_2 production through serpentinization by varying temperature and

mineralogical controls, attempting to imitate realistic environmental conditions. Field observations (e.g. Etiope et al. 2013a; Etiope et al. 2013b; Conrad et al. 2013; Hyndman & Peacock 2003; Sanchez-Murillo et al. 2014; Morrill et al. 2013) have begun elucidating the dynamic principles regarding these controls in the natural environment. Further field studies in low temperature terrestrial ultramafic environments are pertinent in developing a clearer model of the complexities involved in hydrocarbon formation during serpentinization.

The Dun Mountain Ophiolite Belt (DMOB) at the Red Hills, Nelson Lakes, New Zealand, is a relatively unaltered ultramafic body currently undergoing low temperature sepentinization. This is a type locality for the rock classification 'dunite', and compared with other obducted ophiolites it is predominantly unserpentinized, displaying alteration only in faulted zones (Johnston 1990; Davis et al. 1979; Lauder 1965). Although previous research has observed serpentinization systems at a geologically related site in south-western Fiordland (Cardace & Hoehler 2014; Giggenbach & Lyon 1990; Wood 1972), no reported studies regarding gas and/or fluid chemistry in the Nelson Lakes region have been completed. The comparatively un-weathered/unaltered state of the ophiolite presents well exposed and defined ophiolitic structures making this an opportune location for analysis of CH_4 production via present day low temperature serpentinization.

Here we report the first occurrence and seepage of CH_4 at the Dun Mountain Ophiolite Belt (DMOB) located at Red Hills. Preliminary discussions are offered examining the potential controls on CH_4 production. Exploration of the environmental processes affecting H_2 production and concurrent CH_4 synthesis may provide field evidence to support existing laboratory conclusions. Carbon dioxide and CH_4 flux in the field are measured using closed chamber accumulation methods. The isotopic analysis of these gases are investigated to assess their origin and to allow comparison with other international studies. The isotopic composition, dissolved gas content and metal concentrations of water that has interacted with the ultramafic body are assessed to provide insight to the connectivity of water-rock interactions. Additionally, the dynamics of carbonate and iron oxide precipitation related to hyper-alkaline fluids are explored; specifically examining their affect on hydrocarbon synthesis. Overall, this multi-tiered approach aims to provide a detailed evaluation of gas-water-rock synergies in an ultramafic system.

2 Objectives

The objectives of this research are to report CH_4 existence and seepage in the Dun Mountain Ophiolite, and to evaluate the controls on CH_4 formation in this kind of natural environment, as summarised in Table 2-1. Ultimately, these objectives will test the hypothesis that the DMOB will provide an ample source of abiotic CH_4 via low T serpentinization reactions.

Table 2-1: Research questions and approach

Research Question	**Approach**
Is there CH_4 and H_2 formation related to serpentinizaton in the Red Hills? If so, how much and what is its origin?	• Gas flux survey using closed chamber accumulation methods • Isotopic investigation of CH_4, CO_2 and H_2 • Observe spatial distribution of gas emissions
What are the potential mineralogical and structural controls on CH_4 release?	• Agglomeration of numerous geologic maps to assess the structures and substrate present in the area • Measure gas flux along transect lines crossing major and minor fault lines
How is serpentinization reflected in the geochemical character of the fluids at the Red Hills?	• Water sampling at numerous sites in the Maitlands Stream, at sources and exits of tributary flows, in isolated tarns and at localised discharging springs • Chemical analysis of these fluids, specifically using field data (i.e. pH, Eh), ICPMS and isotopes • Spatial mapping of data to observe potential water-rock interactions
What are the temporal effects of gas flux and fluid movement? Is there seasonal variation?	• Undertake two flux surveys, in March and July. Assess potential effects of climatic variation on gas flux and fluid flow
What is the nature of biologic and geologic precipitates?	• Analyse amorphous biologic material using biochemistry, 16RSNA sequencing, XRF and diatom identification. • Analyse geologic material using microscopy, SEM / backscatter electron imaging and SEM-EDS element quantification.
How does the flux and signature of gases in the Red Hills compare with previously investigated terrestrial ophiolite outcrops?	• Detailed literature reviews and assuring similar manipulation of data – allowing visual comparison of results
How do ultramafic soils influence the isotopic signature of vegetation in the Red Hills? Do C3 or C4 type plants dominate? Does this impact the isotopic signature of gases emitted?	• Sampling of various dominant plant species for isotopic analyses • Categorise plant type using published available data

3 Background and Review

3.1 Geologic Setting of the Red Hills Complex

The Dun Mountain Ophiolite Belt (DMOB) is a major geologic feature of New Zealand, outcropping in the north (Nelson) and south (Fiordland) of the South Island (Figure 3.1). These two segments have been separated by ~480 km of dextral strike slip motion from the Alpine fault (Wellman 1948). The Nelson segment extends southwards from d'Urville Island ~145 km to its truncation at the Wairau fault near St Arnaud (Robinson et al., 1996). The Red Hills massif is at the southern end of this segment, and at ~110 km^2 represents the largest outcrop of ultramafics in New Zealand (Christensen 1984). Red Hills represents the widest section of the DMOB at 8 km, rarely exceeding 1 km in width elsewhere. It has an inferred thickness of ~4 km (Malahoff 1965) and is crosscut and bound by numerous faults along which serpentinization is common. The north to northeast trending feature divides well-exposed sedimentary deposits on either side. The layered ultramafics are separated from the Permian aged Pelorus Group on the east by the Patuki Mélange, which is 2.5 km wide. In the west, limestones and sandstones of the Maitai group uncomformably overlie mafic deposits of the DMOB (Figure 3.2) .

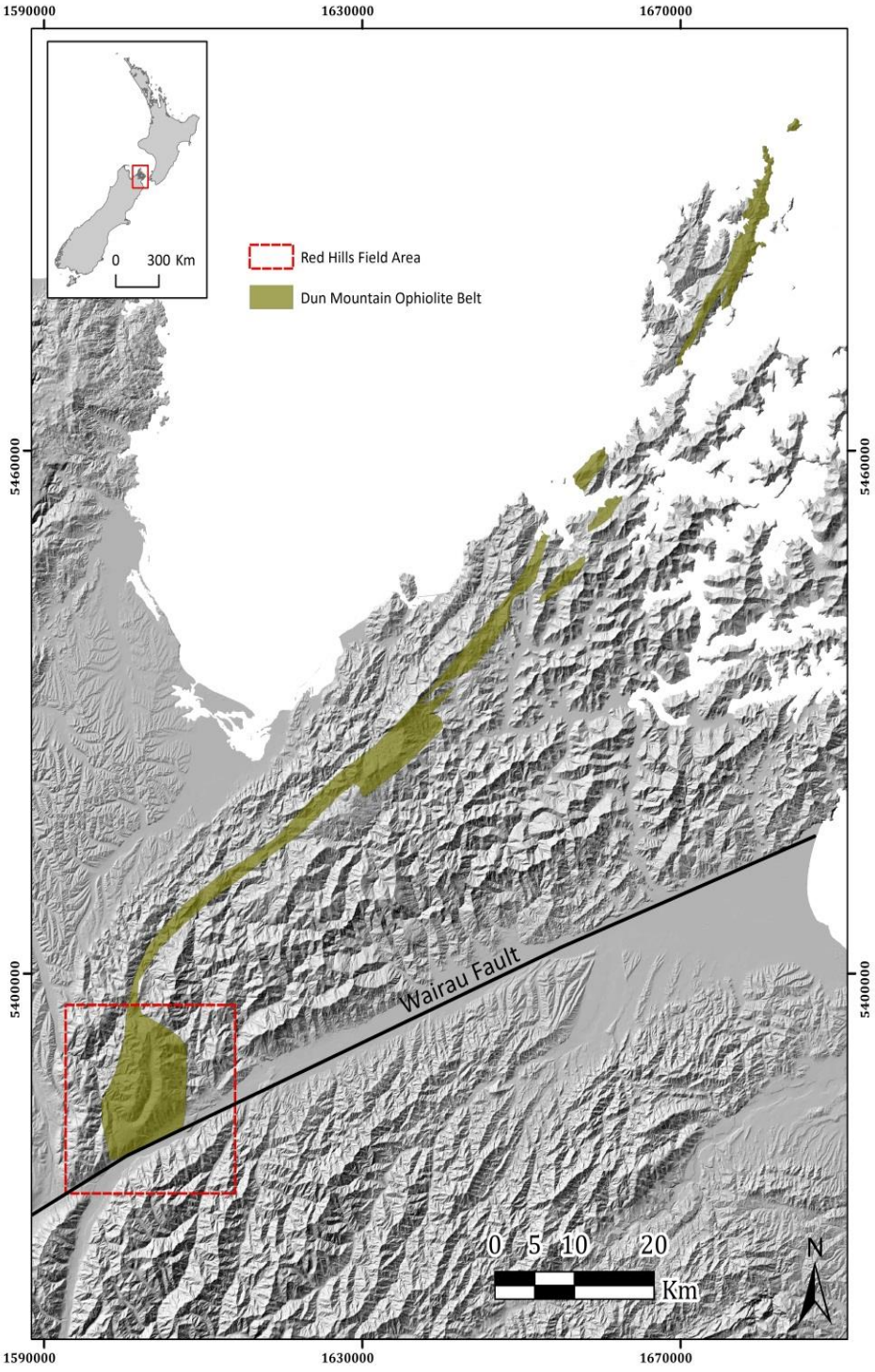

Figure 3.1: The Dun Mountain Ophiolite Belt (in green) outcrops in the north of the South Island, NZ. The field sampling location is outlined in red.

The DMOB is subdivided into the Dun Mountain Ultramafic Group (outcropping in the east) and the Lee River Group (outcropping in the west, Figure 3.2). These two groups vary significantly in thickness and composition, and are in faulted contact (Davis et al., 1979). The Dun Mountain Ultramafic Group has a layered east to west sequence including: protoclastic harzburgite, harzburgite, dunite, layered pyroxenite and layered pyroxenite with gabbro-sills (Davis et al., 1979). The general mineralogy of typical harzburgites and serpentinized harzburgites in the Red Hills as observed by Hunter (1977) and Sivell & McCulloch (2000) is summarized in Table 3-1.

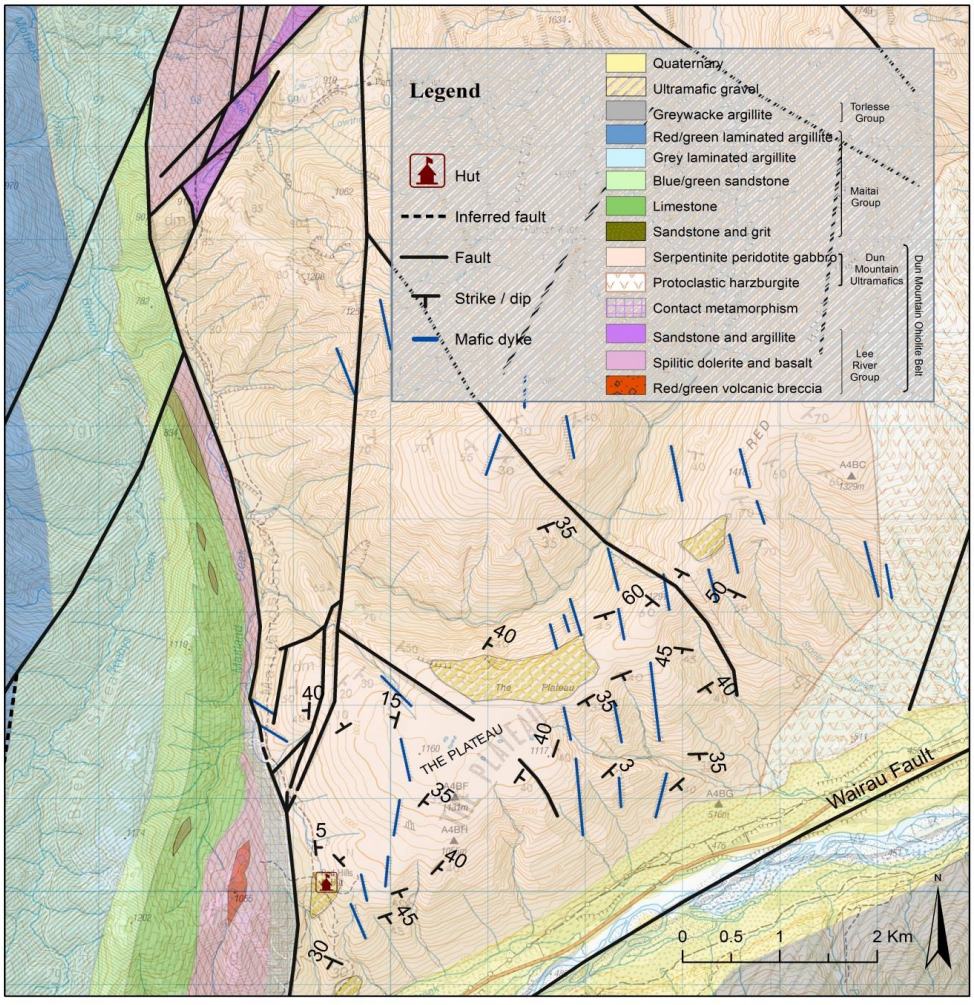

Figure 3.2: The geology of the Red Hills complex, as adapted from Walcott (1969) and Johnston, (1982), shows extensive faulting and is intruded by numerous mafic dikes. The field sampling area is located west of The Plateau.

Table 3-1: Weight % of oxides and general mineralogy for harzburgites and serpentinized harzburgites of the Red Hills

Oxide	**Harzburgite %**	**Serpentinized Harzburgite %**
SiO_2	43.61	40.28
$Al2O_3$	1.06	0.96
FeO	8.04	3
MnO	0.14	0.11
MgO	44.08	37.77
CaO	1.35	0.06
Na_2O	0.02	0.1
K_2O	<0.0005	0.01
Cr_2O_3	0.44	-
NiO	0.27	-
TiO_2	-	0.01
Fe_2O_3	-	5.71
P_2O_5	-	0.01
H_2O+	0.33	12.27
H_2O-	0.03	-
Total	99.34	100.29
Reference	(Hunter 1977; Davis et al. 1979)	(Sivell & McCulloch 2000)
Mineralogy of Ultramafics		
Major ultramafics	Harzburgite	-
Minor ultramafics	Dunnite	-
Olivine end member	Forsterite (95)	-
Orthopyroxene end member	Enstatite (89)	-
Plagioclaise end member	Anorthite (96)	-
Serpentine polymorph	Lizardite	-
Main Catalytic minerals	Wairauite	-
	Awaruite	-
	Chromite	-

The Lee River Group includes the gabbro intrusive complex of the Tinline formation at the base (missing in the Red Hills due to faulting; Davis et al., 1979), ranging toward diabases and basalt sheets of the Glennie formation at the top (Johnston 1982). The Tinline formation is poorly exposed, and consists of NNE-NE striking, steeply dipping intrusive sills. The base of the Tinline formation is generally in faulted contact with the Dun Mountain Ultramafic Group. The Glennie formation consists of dark, greyish green massive spilitic basalt and has a gradational contact with the underlying gabbros of the Tinline formation.

The DMOB is incised with numerous steeply dipping mafic dykes, generally striking north/south. Many of the dykes are clustered in a sector just north of The Plateau (Figure 3.2) and range in thickness between 1.5 and 18 meters (Walcott 1968). The cross cutting relationships with the anticlinal micro folded limbs into which they intrude suggests they post-date folding events such as the Rangitata Orogeny (Walcott 1968). These dykes range in composition from hornblende and pyroxene microgabbros to diaschistic rocks banded with segregated felsic and mafic minerals from within the microgabbros. The primary minerals consist of plagioclase, augite, hypersthene and magnetite. Chemical analysis undertaken by Davis et al. (1979) indicates that the dykes are chemically similar to the gabbros and basalts of the Lee River Group (low K-theolites with high Na_2O content). This data along with metamorphic character analysis of the dykes from Walcott (1968) suggests the dyke system intruded the Red Hills ultramafic massif whilst it was still hot, supplying magma to the mafic part of the ophiolite.

Copper, gold and platinoid minerals have been mined to varying degrees in the Red Hills (Johnston 1982). Chromite is present as scattered grains within the unserpentinized dunite and harzburgite of the Dun Mountain Ultramafic Group and was mined in a number of areas in the early 1860's, albeit on a small scale. Easily accessible areas such (e.g. Hackets creek; Serpentine Valley) have been entirely worked and prospecting has suggested little remaining chromite of economic quantities.

The Red Hills massif is extensively faulted by a north/north east striking complex. The Wards Pass fault separates the anticlinal structure of the DMOB from the layered sediments in the east, and the Wairau fault (a branch of the Alpine Fault) truncates the ophiolite sequence in the south, giving way to sandstone/mudstone sequences of the Torlesse Group (Figure 3.2). These two faults provide the majority of displacement in the Red Hills, however, numerous smaller faults are present. Northeasterly striking faults down throwing to the east cut the Maitai and upper Lee River Group deposits in the western area. These are observed as crush zones in the field, often containing serpentinite intrusions. The northern boundary of the Red Hills complex is dictated by faults of a similar character, exposing comparable shear zones as observed in the Motueka River.

Physical structures within the Red Hills complex provide diverse environments for an optimal range of gas flux analysis. At The Plateau (Figure 3.2) the ultramafic outcrop displays a unique depressed concave structure, encouraging constant exposure of the unserpentinized minerals to meteoric water and thereby promoting water-rock interactions.

The numerous faulted crush zones within the complex allow comparative observations of a more altered (i.e. serpentinized) area. Multiple geologic units are in faulted contact within a small area, making perpendicular transects an ideal method for examining the effects of gas flow from different origins and via different structural pathways.

3.2 Serpentine Soils

Red Hills serpentine soils are high in cobalt (Co), manganese (Mn), chromium (Cr), magnesium (Mg) and nickel (Ni) - elements toxic to many plant species (Lee et al. 1975; Lee & Hewitt 1982). Robinson et al. (1996) have indicated that mainly higher levels of Ni and Mg are accountable for the dramatic vegetation change between geologic soil boundaries in the Red Hills, with only specialized endemic species and stunted flora growing in the serpentine barrens. Especially high Mg levels cause inhibition of Ca uptake from the plants (via substitution of divalent molecules) limiting essential macronutrients (Robinson et al. 1996; Oze et al. 2004). Also, ultramafic soils tend to be shallow and susceptible to erosion, which is unfavorable for vegetation growth and stability. Essentially, these are atypical soils, which promote very specific vegetation growth. The enriched metal content of the soils provides a unique habitat, which may be exploited by certain microbial communities within the soils and by vegetation growing above them. These biota, both on and in the soils may be a factor capable of modifying gas, water and mineralogical analyses at the soil-water interface (e.g. isotopic signatures, concentration of gases or metal content in solids).

3.3 Serpentinization, H_2 and CH_4 Formation

During serpentinization olivine and/or pyroxene minerals undergo hydrolysis whilst interacting with water, forming serpentinite minerals (e.g. chrisotile, lizardite and antigorite), magnetite and di-hydrogen as observed in the equation:

$$3FeMgSiO_4 + 3H_2O_{(aq)} = Mg_3Si_2O_5(OH)_4 + SiO_{2\,(aq)} + Fe_3O_4 + H_2 \qquad \textbf{Eqn. 1}$$

The H_2 produced during this exothermic reaction is then available to reduce carbon species such as CO, COOH and CO_2 to form CH_4 in what is known as Fischer Trope type (FTT) synthesis. The term FTT broadly refers to the consumption of CO and/or CO_2 and the production of CH_4 and longer chain (liquid) hydrocarbons from the reactions:

$$CO_{2\,(aq)} + [2+(m/2n)]\ H_2 = (1/n)\ C_n\ H_m + 2H_2O \qquad \textbf{Eqn. 2b}$$

$$(2n + 1)\ H_2 + n\ CO \rightarrow C_nH_{(2n+2)} + n\ H_2O \qquad \textbf{Eqn. 2c}$$

FTT reactions are the most common mechanism for CH_4 production in low temperature natural environments, especially in ultramafic settings (Boschetti et al. 2013; McCollom 2013; Etiope & Sherwood Lollar 2013; Mccollom & Seewald 2006; Proskurowski 2010) due to the complementary conditions such as moderate temperatures (<400ºC), reducing environments and an abundance of catalytic metal alloys (Ni, Cr) and Fe oxides .

Methane may be formed from the direct reduction of CO_2 with aid from catalytic transition metals (such as Ni, Cr, Pt, Pd) by the faster one step Sabatier (methanation) process (Proskurowski 2010; Etiope & Sherwood Lollar 2013):

$$CO_2 + 4H_2 = CH_4 + 2H_2O \qquad \textbf{Eqn. 3}$$

or more rigorously by the two-step reverse water-gas shift reaction:

$$CO_2 + H_2 = CO + H_2O \qquad \textbf{Eqn. 4a}$$

$$CO + 3H_2 = CH_4 + H_2O \qquad \textbf{Eqn. 4b}$$

The Sabatier reaction is thermodynamically favoured at low temperatures (<100 °C, Proskurowski 2010). Whilst reactions proceed slowly at these temperatures, the potential for significant accumulation and release of hydrocarbons over geologic timescales is notable, as observed at the Chimaera ophiolitic seep in Turkey where reactions proceed at temperatures of ~50ºC and CH_4 emissions exceed 150 tons / year (Etiope et al. 2011).

In FTT reactions (such as the Sabatier reaction), CH_4 is not formed directly by serpentinization but through reactions between H_2 from peridotite hydration (serpentinization) and CO_2 from the atmosphere or meteoric water. In contrast, some studies have suggested a direct synthesis of abiotic CH_4 through CO_2 saturated waters, as field observations of H_2 depleted and CH_4-rich fluids are made (Boschetti et al. 2013; Etiope et al. 2013a; Oze & Sharma 2005; Sachan et al. 2007). Furthermore, Suda et al. (2014) suggest that abiotic CH_4 is

produced directly from H_2O without mediation by H_2, implying CH_4 production directly from the hydration of olivine, not from the FTT process.

Several other processes have been shown to contribute to CH_4 and longer hydrocarbon formation without following the common FTT methanation mechanism. The presence of CH_4-rich fluids in gabbroic inclusions of the South West Indian Ridge suggests large potential reservoirs for hydrocarbons in mid-ocean ridge hydrothermal systems (Kelley & Frtih-green 1999). Also in sulfur-rich environments where FTT catalysts are less efficient (Proskurowski 2010; Cody et al. 2000), reactions between carbon monoxide (CO) and methanethiol (CH_3SH) in the presence of metal sulfide mineral catalysts have been shown induce chain growth, forming compounds such as acetic acid (CH_3COOH) (Huber & Wächtershäuser 1997). These results offer a substantially wider range of environments in which abiotic CH_4 may be produced, where conditions hosting abundant H_2 may not be an essential component to the process.

3.4 Catalysts

Abiotic CH_4 production via FTT synthesis varies kinetically over different temperatures and pressures, but is particularly dependent on interaction with catalytic species such as spinels, (general formula $A^{2+}B^{3+}{}_2O^{2-}{}_4$, where A and B are separate metal species) which provide a reactive surface promoting electron transfer from interacting water molecules. Chromite ($FeCr_2O_4$), magnetite (Fe_3O_4) and awaruite (Ni_3Fe), which are often present in ultramafic rocks, have been observed as especially strong catalysts for CH_4 production (Oze et al. 2012; Neubeck et al. 2014). Additionally, molybdenum sulfide (MoS_{2+}), nickel sulfide (NiS) and tungsten sulfide (WS_2) have been observed as active FTT catalysts (Holm et al. 2014). These species have only been observed as active catalysts (in a laboratory time scale) in high temperature reactions (>200ºC). The only catalysts observed to be active within the temperature range of continental serpentinization (i.e. <100ºC) are rhodium (Rh) (Jacquemin et al. 2010) and ruthenium (Ru) (Thampi et al. 1987). Experimental analyses from Etiope & Ionescu (2014) found Ru to be an effective catalyst for CH_4 production at room temperature (20-25ºC) offering important implications for Ru-bearing chromite within ultramafics of terrestrial serpentinite systems.

Serpentinization generally relates to the hydrolysis and transformation of the ferromagnesian minerals olivine [$(Mg,Fe)_2SiO_4$] and pyroxene [$(Mg,Fe)SiO_3$]. In olivine-rich ultramafics, the presence of Ni is common, encouraging the formation of various Ni-Fe alloys, which act to

catalyze the synthesis of CH_4 and other hydrocarbons via FTT synthesis. In contrast, pyroxene-rich ultramafics in principle produce the catalyst magnetite (Fe_3O_4) during serpentinization. However, recent experiments by Klein et al. (2013) observe that pyroxene-rich ultramafics preferentially produce more ferrous iron-rich serpentine (e.g. Fe-bearing brucite), allowing less Fe^{2+} available for oxidation and magnetite – a known catalyst for H_2 production. Because the formation of H_2 during serpentinization is strongly correlated to the amount of Fe^{2+} available for oxidation, this incorporation, along with the concurrent obstruction of magnetite formation, results in less H_2 and concurrent CH_4 production. The formation of specific catalysts and resultant effect on hydrocarbon synthesis is, therefore, highly dependent on the parent material of the ultramafic body.

3.5 Serpentinization and Temperature

Abiotic CH_4 production can originate from several geologic environments on Earth. High temperature magmatic / hydrothermal systems in volcanically active areas have received significant scientific attention and are thought to emit 3-7 Mt per year of CH_4 (Etiope 2012). It must be noted that considerable fractions of CH_4 in geothermal areas may not be abiotic, but biotic (thermogenic), due to thermal alteration of organic matter in the sediments involved in geothermal fluid circulation (Etiope et al. 2007).

Abiotic synthesis by water-rock interactions within ultramafic geology (i.e. serpeninization and FTT / Sabatier reactions) are likely to emit more CH_4 to the atmosphere when compared with magma degassing, but quantities are currently unknown (Etiope & Sherwood Lollar 2013). As observed in Figure 3.3, these occur within a wide temperature window (25-500ºC) in varying environments within the Earth's lithosphere with a resulting range in hydrocarbon production capacity. Many studies regarding FTT and Sabatier reactions focus on high temperature (>100ºC) ultramafic environments such as peridotite hosted hydrothermal systems (Schwarzenbach et al. 2013) and submarine mid-ocean ridges (Fruh-green et al. 2004) as the high temperatures promote faster reaction rates and lower kinetic barriers. However, these environments are not likely to support microbial life and are a much rarer occurrence than exposed low temperature ultramafic serpentinizing systems. The reaction kinetics at these systems are theoretically much slower at lower temperatures (<100ºC) and up until recently may have been overlooked as a source of hydrocarbon production on Earth. New research, however, suggests that CH_4 formation may be enhanced by low temperature catalytic species such as Ru (Etiope & Ionescu 2014). New research on low temperature serpentinization reactions has the potential to expand the known environments capable of

producing CH_4 and therefore drastically expand known environments where such reactions can support microbial life.

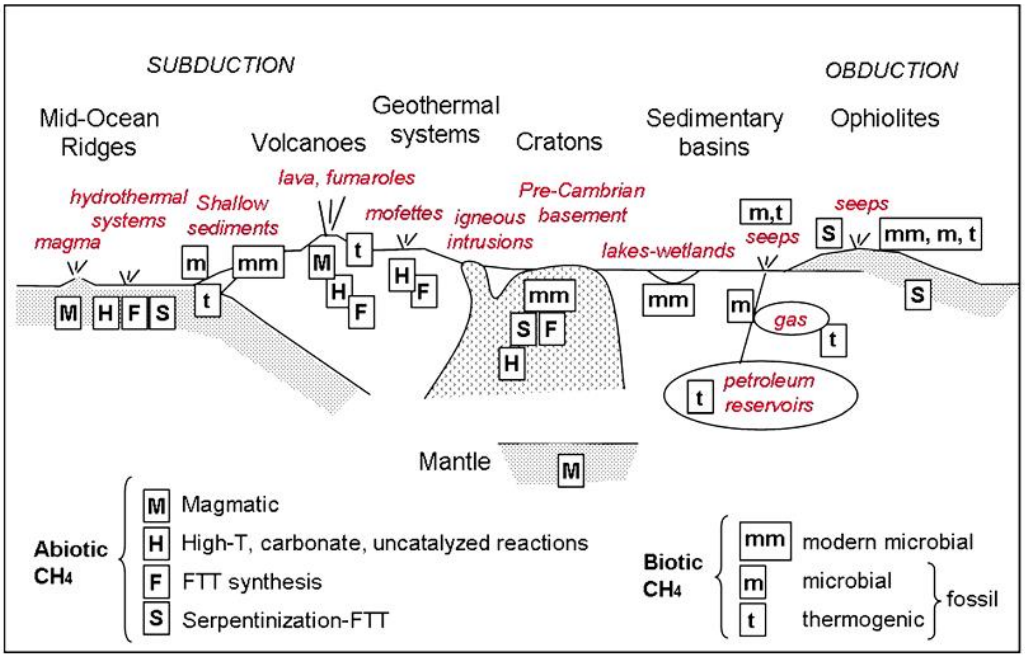

Figure 3.3: Examples of abiotic CH_4 occurrences from Etiope & Sherwood Lollar (2013). High-T, carbonate and uncatalyzed reactions (H) refer to high-temperature to processes (>200 °C) as observed in Appendix 1, equations 1-4. Fischer-Tropsch Type (FTT) synthesis (F) can be independent of serpentinization or associated with serpentinization of ultramafic rocks (S).

The role of temperature regarding CH_4 and H_2 production is well defined by McCollom & Bach (2009) who suggest that peak H_2 synthesis occurs at temperatures between 200 – 300 ºC (at 35 MPa). At temperatures below ~150ºC reaction kinetics are shown to be slow and the incorporation of Fe^{2+} species into Fe-bearing brucite results in limited H_2 production (see previous section). Mayhew et al. (2013) and Neubeck et al. (2014) conducted multiple experiments monitoring H_2 production from reacting ultramafic minerals at a range of temperatures between 30 - 100ºC. Both studies suggest that at low temperatures the presence of spinels and other catalysts have the greatest influence on H_2 production. It was expected that Fe^{2+} content in relation to the substrate type (e.g. pyroxenite / peridotite) would largely affect H_2 production in varying low temperature experiments <100ºC; however, results indicated that the presence of spinels such as magnetite and chromite aid in electron transfer with adsorbed water molecules on the mineral surface, resulting in oxidation of metals (e.g. Fe^{2+}) and concurrent catalyzed H_2 production. In a more recent experiment, Etiope & Ionescu (2014) present the first laboratory evidence of CH_4 production (previous studies focus on the preliminary step of H_2 production) via FTT synthesis at temperatures between 20-90ºC in

ultramafic material. As previously stated, this has demonstrated that extensive CH_4 can form at low temperatures (e.g. ~20 ºC) in the presence of an Ru catalyst, which is sometimes found in chromite bearing rocks such as harzburgite. It should be noted that experiments relating to catalytic (e.g. Ru) effects in a laboratory environment proceed on a timescale of weeks to months. Alternative catalysts such as chromite, awaruite and magnetite, although far less effective at lower temperatures (<200ºC) are substantially more abundant in ultramafic environments and are likely to be effective on a longer (i.e. geologic) time scale.

Low temperature lab experiments are accompanied by a number of recent field studies, which aid in developing a realistic overview of serpentinization systems in the natural environment (e.g. Etiope et al. 2013a; Etiope et al. 2013b; Boschetti et al. 2013; Morrill et al. 2013; Conrad et al. 2013; Frost et al. 2013; Sanchez-Murillo et al. 2014). The Chimaera gas seep in Turkey represents the largest abiotic gas seep on Earth releasing a total of ~150-190 t yr^{-1} of CH_4 from over 50 gas vents over a 5,000 m^2 ophiotlite outcrop (Etiope et al. 2011). Micro seepage (i.e., diffuse exhalation of methane from the ground) at this site ranges from 68 to 1,040 mg $m^{-2}d^{-1}$ and macro seepage occurs at 50-100 t yr^{-1}, with a $\delta^{13}C$-CH_4 value of -12 ‰ (VPDB). At the Orthrys ophiolite in Greece, soils surrounding hyper-alkaline springs emit CH_4 at ~100-1000 mg $m^{-2}d^{-1}$ with a $\delta^{13}C$-CH_4 value ranging from −27‰ to −37.3‰ (Etiope et al. 2013a). At the serpentinizing peridotites in Genova, Italy fluxes of 40 to 50 g m^{-2} day^{-1} were measured above hyper-alkaline waters with a $\delta^{13}C$- CH_4 value of -9 ‰. Average $\delta^{13}C$-CH_4 values at the Cedars, California, vary from -56‰ at GP to -62‰ suggesting a more mixed microbial/thermogenic origin. Large variation is observed in the fluxes and isotopic signatures of published field studies, illustrating the complex nature of CH_4 and H_2 formation during serpentinization in the natural environment. Although laboratory experiments offer useful information regarding the controls of CH_4 formation, further field studies are required to constrain a typical range of isotopic signatures and to provide measured CH_4 flux from terrestrial low temperature ophiolite systems.

4 Materials and Methods

Sampling

4.1 Sample Sites and Materials

Field analyses were conducted over two trips, one in April (summer) and one in July (winter), 2014. Hereafter, either 'summer' or 'winter' will specify the season of the data. Sampling locations for gas, water, rock and amorphous material analyses are displayed in Figure 4.1.

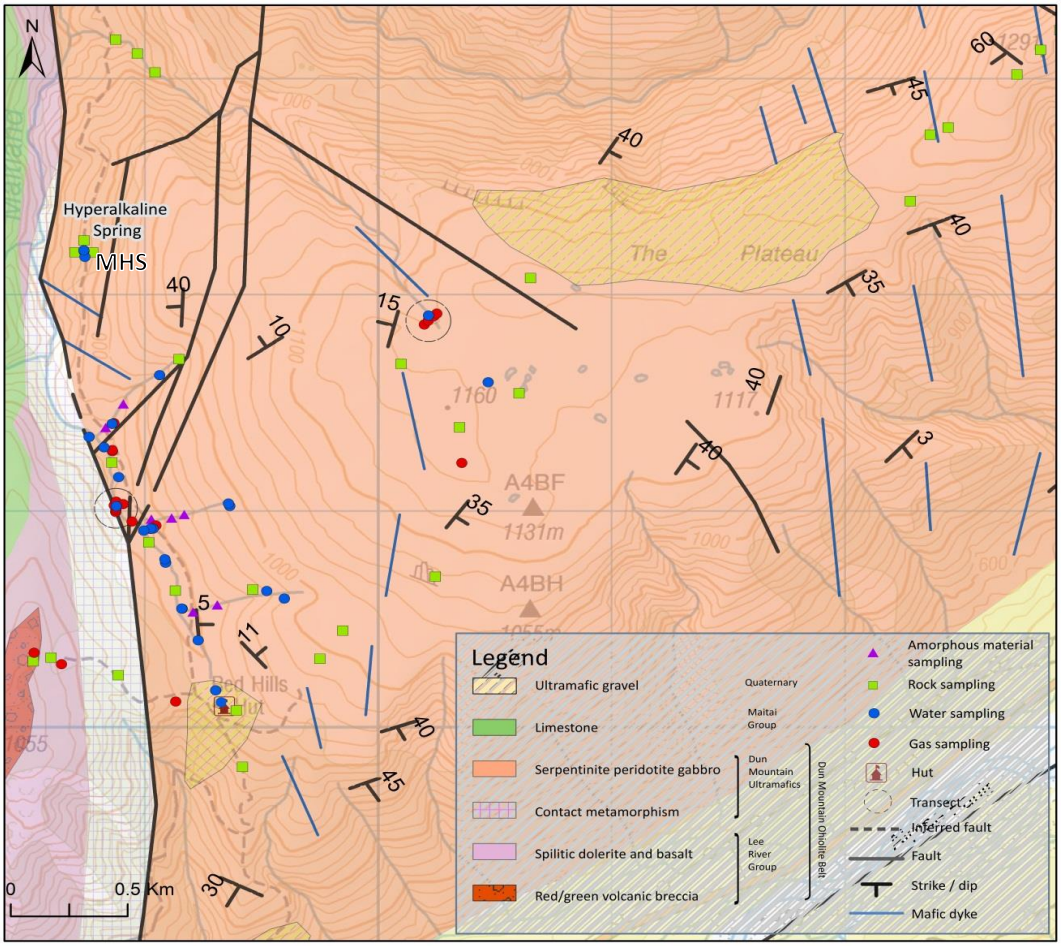

Figure 4.1: Sampling locations for the collection of amorphous material, rocks, water and gas in the Red Hills. Areas which were sampled as transects are specified with a dotted grey circle. A larger overview of the area and its geology can be viewed in Figure 3.2.

During summer, twenty-six sites were visited to analyse the flux, concentration and $\delta^{13}C$ values of CO_2 and CH_4 in the Red Hills. Water samples were taken from eighteen sites for cation content and isotopic analyses. Rock samples were collected at 30 sites. Summer

sampling occurred after a long period of stable warm weather (>10 days with no precipitation). Two sites were revisited in winter during a shorter period of stable cold weather (>3 days with no precipitation) utilizing different sampling methods for both replicate and alternate analyses of gas flux and dissolved gas in water. Amorphous material (as observed in Figure 4.2 A and B) was also collected from 7 sites during winter sampling.

Figure 4.2: Images A and B show the sampling methods of amorphous materials. Image C shows the method used for water sampling at site MHS (see Figure 4.1 for locations).

The sampling area covered a topographically and geologically diverse 2 km^2 area proximal to the Red Hills hut. Due to the large, steep and occasionally densely vegetated sampling area spot sampling was often the most appropriate method; however, transect lines between 10 m and 30 m were set up in two separate areas and measured at 5 m intervals perpendicular to faults and areas of structural/vegetation change (transect locations observed in dotted circles in Figure 4.1). Previous studies have concluded that most hyper-alkaline springs emitting abiotic CH_4 are situated along faults or shear zones (Etiope et al. 2013a; Johnston 1990), therefore, to increase the likelihood of detecting alteration gases many sampling locations were situated in proximity to faults. Locations were also chosen by visual clues such as lack of vegetation and the presence of highly altered and/or serpentinized materials.

Soil temperature was measured within 10 cm of accumulation chamber footprint at each site with a 10 cm Center 370 RDT thermometer, which has an accuracy of ± 0.1 °C. Ambient air temperature and barometric pressure were recorded at every site. To minimise variations in gas flux, sampling was constrained to meteorologically stable and dry conditions according to recommendations by Lewicki et al. (2005).

4.2 Gas (CO_2 and CH_4) Flux Measurements

Soil gas flux of CO_2 was measured in the field using the closed system accumulation chamber method (Livingston & Hutchinson 1995; Figure 4.3 and Figure 4.4), with a West Systems LI-820 infrared CO_2 gas analyzer (sensitivity range of 0 - 20,000 ppm, company reported accuracy of 3%). More details on use can be found in Chiodini et al., (1998). This machine was equipped with a WS-HC-IR CH_4 detector with a sensitivity range of 10,000 ppm and a detection limit of 60 ppm. This sensor was used for in-field measurements at some sites during the summer, but during the winter the flux values were below the detection limits of the sensor. As a result, concentration measurements were analysed in the laboratory concurrently with isotopic measurements (see section 4.6).

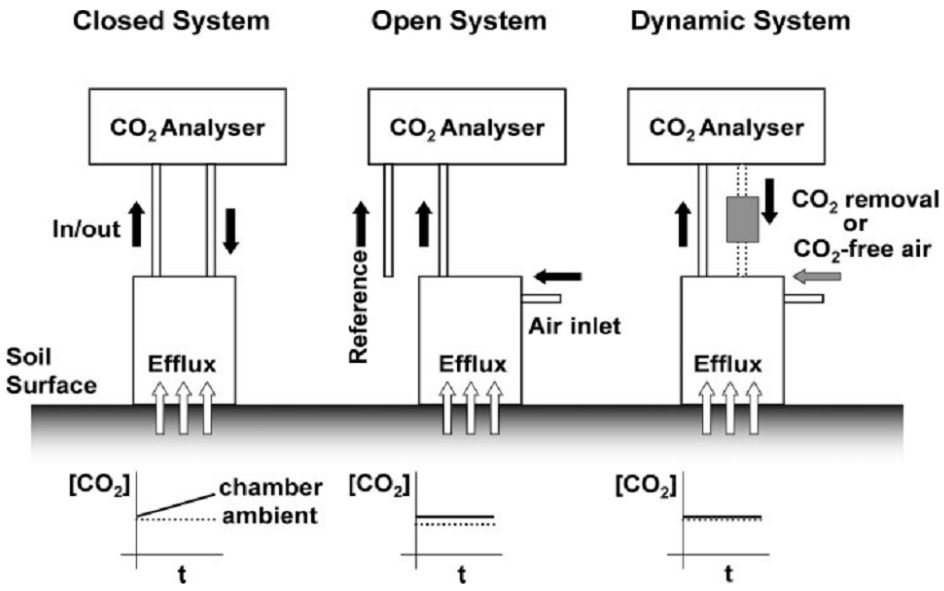

Figure 4.3: A schematic illustration of a closed system chamber of gas sampling compared to open and dynamic systems from Midwood & Millard (2011).

Samples of 35 mL were extracted from the chamber at 10, 20 and 30 minute intervals using a gas tight 50 mL syringe, according to methods described in Parkin et al. (2003). A sample of atmospheric air was taken daily to simulate time 0. These were immediately injected into 12mL exetainer vials, creating over pressurisation allowing extraction of ~20 mL for analysis.

Vials were pre-flushed with either helium (for IRMS analysis) or nitrogen (for CRDS analysis), sealed with grey butyl rubber septa and stored in refrigeration before and after sampling.

The field sampling in winter returned to the hyper-alkaline site (Figure 4.1) and utilized different methods. Pre evacuated 20 mL crimp top vials with PTFE/butyl rubber stoppers and aluminium seals were inserted with 30 mL chamber gas at accumulation times of 0, 1, 2, 5 and 10 minutes in order to provide more detailed information in a shorter time period.

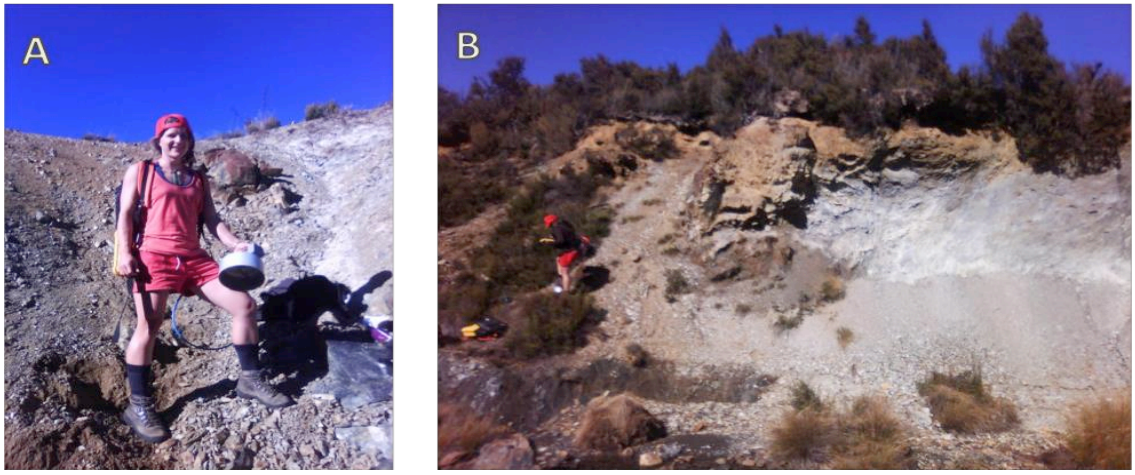

Figure 4.4: Gas sampling with closed system chamber method using the West Systems gas detector. A gas mixer is observed inside the chamber in image A, and the method of deployment during gas accumulation is observed in image B. Both images display extensively sheared geology adjacent to the Maitlands Stream.

4.3 Water Sampling for Metals, H_2O Isotopes and Hydrochemical Analyses

Water samples of 50 mL were taken from surface waters in the Red Hills for metal concentration and analysis of O and H isotopes. The source and middle of each contributing stream to the Maitlands were sampled, as was the Maitlands stream at various locations above and below tributaries within a 1500 m section (Figure 4.1). Care was taken to minimise contamination by wearing gloves and using fresh unused gloves vials, needles, filters and sterilised high-density polyurethane containers at each site. The Eh, pH, temperature and conductivity were all measured on site using a Mettler Toledo SevenGo Duo pro pH/Ion/Cond with meter heads, Mettler Toledo Inlab ® Expert Pro-ISM-IP67 pH 0-14, 0-100ºC and Mettler Toledo Inlab® 738 ISM Conductivity NTC 30kΩ 0.01-1000mS/cm, 0-100ºC. The pH meter was calibrated daily using standard pH 4.01 and 7.00 buffer solutions.

During winter sampling, site MHS was specified as a site of special interest due to the high CH_4 flux determined during intial (summer) field sampling. For dissolved gas analyses, water

samples were collected at site MHS in borosilicate glass bottles and treated with 10 µl of 50% w/v $ZnCl_2$ per mL of water sample to reduce biologic activity and prevent microbial oxidation (Figure 4.2 C).

4.4 Amorphous Material Sampling

Amorphous material in quantities ranging from 3 – 50 grams was scraped from sites specified in Figure 4.1. This material often seeped from near-surface soil horizons, which the streams / rivers had cut into and exposed. The sample tool was a 20cm stainless steel elongate spatula, which was sterilised before and after sampling using alcohol wipes. Using an open flame, the spatula was also heated until red hot to aid in sterilisation after each sample was taken. Material was stored in high-density polyurethane plastic containers, and a separate snap lock bag to contamination. Following sampling, this material was stored in a -80 ºC freezer until testing commenced.

4.5 Rock Sampling

Rock samples were extracted using a rock hammer and stored in snap lock bags. Sample sites are presented in Figure 4.1. Rocks for isotopic analyses were only collected from site MHS. Types of rock collected ranged from harzburgite, serpentinite, gabbro, micorgabbro dikes, volcanic breccia, basalt, quartz veins, carbonate nodules and porous travertine deposits. The majority of these were made into standard thin sections for mineralogical and textural analyses. Representative samples of harzburgite, serpentinite and carbonates were made into polished thin sections for SEM-EDS work.

Analyses

4.6 Concentration of Accumulated Gas

The concentration of CO_2 was measured in-field using the West Systems LI-820 infrared CO_2 gas analyzer at all sites, however the CH_4 was only able to be measured in-field at site MHS, where fluxes were above the detection limits of the WS-HC-IR CH_4. For all other sampling sites this detector was inappropriate for the low CH_4 flux (detection limit 60ppm). Subsequently, CH_4 values were back-calculated using CO_2 as a tracer gas (accounting for changes in concentration due to sampling) with CRDS equipment. The LI-820 CO_2 detector and WS-HS-IR CH_4 detector were calibrated before use for both CO_2 and CH_4 with appropriate standard gases in accordance to West System specifications.

Concentrations of CO_2 and CH_4 were further analysed at the University of Canterbury SABRE lab using cavity ring down spectroscopy (CRDS) (Picarro G2201-i, run in simultaneous CH_4 / CO_2 measurement mode) with a guaranteed spec range of 380 – 2,000 ppm (CO_2), 10 – 500ppm (CH_4) in high dynamic range mode and 1.8 – 12ppm (CH_4) in high precision mode. Concentration precision for this instrument is rated at 200 ppb + 0.05 % (CO_2), 5 ppb + 0.05 % (CH_4) in high precision mode and 50 ppb + 0.05 % [CH_4] in high dynamic range mode.

Fluxes were calculated using methods described in the West Systems 8.2 release handbook. The accumulation chamber factor (A.c.K) was calculated using the equation:

$$K = \frac{86400 \cdot \mathrm{P}}{10^6 \cdot R \cdot T_k} \cdot \frac{V}{A} \qquad \textbf{Eqn. 5}$$

where P is the barometric pressure (mBar), R is the gas constant 0.83 bar L $K^{-1}mol^{-1}$, T_k is the air temperature (K), V is the chamber volume (m^3) and A is the chamber inlet area (m^2). The A.c.K factor is then multiplied by the flux rate (ppm sec^{-1}) as viewed on the West Systems hand held palm pilot to calculate the flux in mol^{-1} m^2 day^{-1}. To calculate the flux in mg m^2 day^{-1} this value is then multiplied by 1,000 and the molecular mass of the gas in question (CO_2 or CH_4).

4.7 Concentration of Dissolved Gas in Solution

Gas in solution was extracted using headspace equilibration methods as described in Etiope (1997). A 60 mL syringe was filled with 30mL of sample fluid, leaving 30mL of headspace. A three-way valve was attached to the needle to minimise leakage whilst the sample was shaken vigorously for 5 minutes at room temperature. Headspace gas was then injected into a pre-evacuated and nitrogen flushed vial, and analysed using CRDS methods (Picarro G2201-i).

The initial concentration of gas in solution (C_s) was calculated using the equation:

$$C_s = (C_G \times B) + (C_G - C_A) \times \left(\frac{V_G}{V_L}\right) \qquad \textbf{Eqn. 6}$$

where C_G is the gas concentration, B is the Bunsen solubility coefficient, C_A is the the gas concentration in atmospheric air and VL and VG are the volumes of the liquid and headspace (Etiope 1997).

4.8 Isotopic Analyses

4.8.1 Gas

Isotopic composition of CO_2 were analysed at the University of Canterbury Stable Isotope Laboratory using a Thermo Scientific GasBench II connected to a Delta V+ gas isotope ratio mass spectrometer under continuous flow conditions, which is accurate to <0.10‰ based on repeated analysis of NBS-19 and NBS-19 certified reference materials.

Isotopic precision is <0.16‰ for $\delta^{13}C_{CO2}$, <1.15‰ for $\delta^{13}C_{CH4}$ in high precision mode and < 0.55‰ for $\delta^{13}C_{CH4}$ in high dynamic range mode.

Background atmospheric $\delta^{13}C_{CH4}$ values and CH_4 concentrations were obtained from an average of 6 data points taken at Baring Head (North Island, NZ) in 2013, from the National Oceanic and Atmospheric Administration (NOOA) Earth System Research Laboratory (ESRL) which is publicly available at (http://www.esrl.noaa.gov).

To establish the origin of measured CH_4 (abiotic or biotic), the ratio differences between the two carbon isotopes ^{13}C and ^{12}C are determined using the following equation relative to the PDB limestone (PeeDee Belemnite) standard.

$$\delta^{13}C = \left(\frac{\left(\frac{^{13}C}{^{12}C}\right) sample}{\left(\frac{^{13}C}{^{12}C}\right) standard} - 1 \right) \times 1000\ ‰ \qquad \textbf{Eqn. 7}$$

Although strict values evolve with developing studies, current ranges of $\delta^{13}C_{CH4}$ values are suggested in Etiope & Schoell (2014). Generally biotic values are < –55 ‰ for microbial sources and range between –55 and –25 ‰ for thermogenic sources (note that biotic CH_4 can either be microbial or thermogenic; see section 3.5). Values of abiotic CH_4 generally range between –37 and –45 ‰. To better distinguish the origin of CH_4, the δD_{CH4} (%VSMOW) is plotted as a function of $\delta^{13}C_{CH4}$. General boundaries of microbial, thermogenic and abiogenic signatures have been adopted using such plots as observed in Figure 4.5 (Whiticar 1999; Etiope et al. 2011).

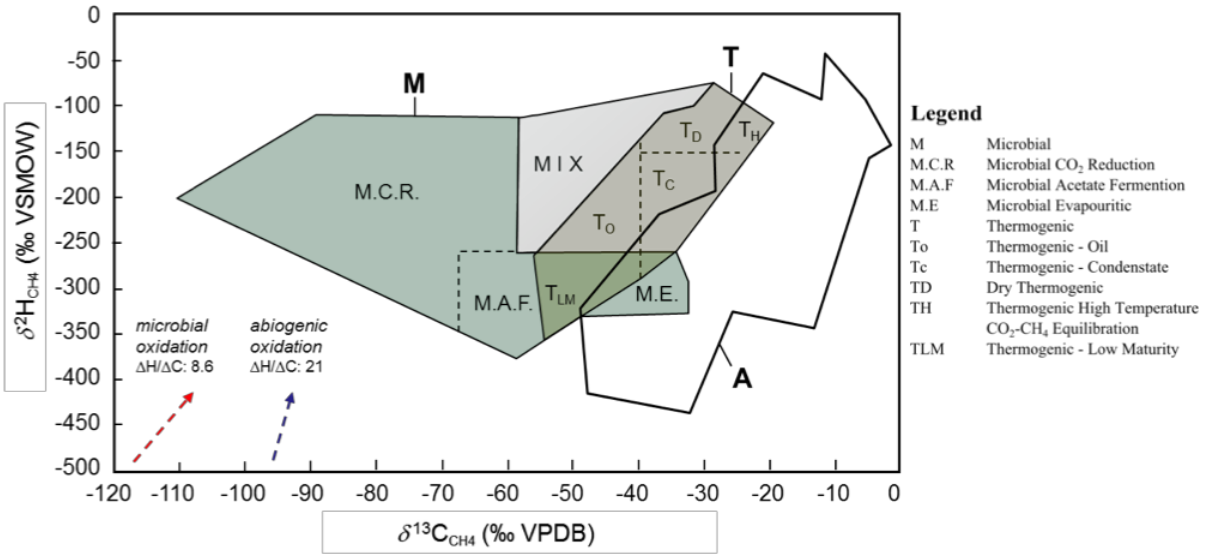

Figure 4.5: Isotopic boundaries of CH_4 - updated after Schoell, 1988; Hunt, 1996; Etiope et al., 2013; Etiope and Sherwood Lollar, 2013; Etiope and Schoell, 2014. These plots distinguish general boundaries of microbial (M), thermogenic (T) and abiogenic (A) methane.

4.8.2 Dissolved Gas in Solution

Isotopic analyses of $\delta^{13}C_{CO2}$ and $\delta^{13}C_{CH4}$ were analysed using CRDS techniques on the Picarro G2201-i, run in simultaneous CH_4 / CO_2 measurement mode as in section 4.8.1

For comparative results, duplicate samples were run for $\delta^{13}C_{CO2}$ and $\delta^{13}C_{CH4}$ values, with the addition of analyzing deuterium isotopes (δD) of CH_4 at the Victoria University Biogeochemistry School of Earth and Ocean Sciences (British Columbia, Canada). This analyses used a MAT 253 mass spectrometer with a Conflo IV interface, Trace GC Ultra, and GC Isolink Gas samples which were introduced onto a GSQ PLOT column (0.32mmID, 30m)

using a Valco 6-port valve and sample loop. After chromatographic separation, components were passed through an oxidation (1030 °C) or pyrolysis (1400 °C) reactor and water trap before passing to the Conflo interface.

In-house CH_4 standards of known isotopic composition were also run to allow calibration to the VPDB ($\delta^{13}C$) and VSMOW (δD) scales. Results for $\delta^{13}C$ are accurate to ±0.2 ‰, and ±3 ‰ for δD.

4.8.3 Water

Vials for isotopic analysis of water were filled and capped underwater to avoid any headspace that may allow isotopic fractionation. $\delta^{18}O$ and δD were analysed at the University of Canterbury Stable Isotope Laboratory using a Picarro Liquid Water Isotope Analyser (LWIA) 1000 series. Two µl of sample fluid were injected at least 6 times, discarding the first two due to the memory affect. The standard deviation and mean were taken of the remaining 4 injections. The δO^{18} and δD values were normalized to the VSMOW SLAP (southern latitude Antarctic precipitation) scale. Quality control (Q_c) and quality assurance (Q_a), or the reproducibility of the data, was determined through analysis of GISP (Greenland Ice Sheet Precipitation) Tel 1, Tel 2, Tel 3 and Tel 4 reference water standards.

4.8.4 Carbonates

Carbonate precipitates were collected from within the hyper-alkaline spring at site MHS (Figure 4.1). Samples were reacted with 103% phosphoric acid to produce CO_2, which was analysed for $\delta^{13}C$ and $\delta^{18}O$ values at the University of Canterbury Stable Isotope Laboratory using a Thermo Scientific GasBench II connected to a Delta V+ gas isotope ratio mass spectrometer, identical to methods stated previously. Three extractions were taken from the porous carbonate as observed in Figure 5.1, labeled ‘Exterior’, ‘Interior White’ and ‘Interior Beige’.

The processing of this isotopic data required specific calculations to allow comparison with carbonates from other hyper-alkaline systems worldwide. This involved calculating the ideal versus actual fractionation between both carbon and oxygen isotopes during the precipitation of carbonates at site MHS. Ideal isotopic fractionation factors were calculated to represent equilibrium conditions during the formation of carbonates in hyper-alkaline waters.

Equations from Bottinga (1966) were utilised for this purpose. Equilibrium carbon fractionation used the equation:

$$1000 \ln \propto_C = -3.2798 + \left(1.0611 \times \frac{10^4}{T}\right) - \left(1.8034 \times \frac{10^5}{T^2}\right) \quad \textbf{Eqn. 8}$$

and equilibrium oxygen fractionation used the equation:

$$1000 \ln \propto_O = -2.4612 + \left(7.6663 \times \frac{10^3}{T}\right) - \left(2.9880 \times \frac{10^6}{T^2}\right) \quad \textbf{Eqn. 9}$$

where α is the fractionation factor and T is temperature in °K.

4.8.5 Amorphous Material

The $\delta^{13}C$-CO_2 values of the amorphous material was measured using a Costec 4010 elemental combustion system (ECS) connected the Delta V+ isotope ratio mass spectrometer. The combustion reactor of the ECS is run at 900ºC, and the reduction reactor at 650ºC. 1-5mL of sample was tested under ultra-high purity (UHP) helium flow at a rate of 100 mL / minute. Samples were normalized to IAEA-CH-3 and NBS 22 certified reference materials.

4.8.6 Vegetation

Isotopic signature of the dominant plant species in the Red Hills was determined using a Costec 4010 elemental combustion system (ECS) connected the Delta V+ isotope ratio mass spectrometer - identical to the isotopic analyses of amorphous material in section 4.8.5. One mg of sample was run of 9 different species (observed in Appendix 7) which were collected in air-tight bags using gloves and stored in refrigeration prior to analysis.

4.9 Water Analyses for Metal Content Using ICP-MS

The concentration of various metals (Mg^{2+}, Fe^{2+}, Ca^{2+}, Al^{3+}, K^+, Cr, Mn, Co, Ni, Cu, Zn, As) in fluids from Red Hills was determined using inductively coupled plasma mass spectrometry (ICP-MS) analysis at the University of Canterbury Chemistry department with an Agilent 7500 Series ICP-MS with Octopole Reaction System. Fluid samples were filtered to 0.45µm in the field to remove particulate matter and were acidified by adding 0.05mL per 50mL (0.1%) of 70% ultra-pure nitric acid to ensure stability and comparability with calibration

standards. Duplicates were taken every 10 samples for quality control (Qc). Every 20 samples a triplicate was taken for spiking in the lab, another Qc measure to ascertain the accuracy of the analysis instrument.

4.10 Amorphous Material Analyses - Processing and Characterisation

To analyse for potential bacteria within the amorphous material, samples were cultured nutrient agar at 20, 25 and 30º C at the microbiology department, University of Canterbury. Cultured samples were analysed microscopically by trained staff, followed by Gram stain testing (details can be found in Bartholomew & Mittwer, 1952), which was undertaken for preliminary biological identification. Samples of interest were then sequenced using 16SRNA at the Department of Biological Sciences, University of Canterbury.

The amorphous material was processed for diatom analysis by firstly drying samples for 2 days in a 50ºC oven. Organic matter was then removed by reacting samples with 20 mL of 27% hydrogen peroxide (H_2O_2). These were left to digest for 1–3 days at room temperature, adding measured amounts of H_2O_2 until samples were unreactive. Carbonate was then removed by adding 10 mL of 32% hydrochloric acid (HCL) and gently heating. These were then cooled, transferred into a centrifuge tube and diluted up to 45 mL using filtered water. After centrifuging at 3,000 rpm for 5 minutes the liquid was then poured off and replaced with filtered water. This process was repeated five times in order to remove the acid digestion chemicals from the sample.

In order to remove sand-sized material, the samples were then shaken vigorously for 15 seconds in closed centrifuge containers, left to stand for 45 seconds and the remaining suspension poured into a clean tube and retained. This process was repeated, and followed by a clay removal process. Samples were again made up to 45 mL with filtered water and six drops of sodium hexametaphosphate was added. The sample was then shaken and centrifuged at 1800 rpm for 3 minutes, after which cloudy liquid was discarded. This process was repeated seven times until liquid was clear, and then centrifuged at 3,000 rpm for five minutes. Slides were then prepared using a combination of the pipette and evaporation method. Samples were re-suspended in 5 mL of filtered water a drop pipetted onto a pre-warmed coverslip on a hot plate. Two samples were prepared on separate coverslips for each microscope slide. The first received one drop of sample fluid, and the second received two (to double the concentration of diatoms). Both were then diluted with enough filtered water to disperse the sample evenly across the slide. Slips were then heated gently until all the water

was evaporated, then lifted and inverted onto a pre-warmed microscope slide on which two drops of Naphrax had been added for adhesion. Slides were then left to bubble (as toluene evaporates from the Naphrax) and harden. These were then sealed with base coat colourless nail polish and any excess Naphrax was removed using a sharp knife.

4.11 Mineralogy and Petrography

A Leica DM2500P petrographic microscope was used at 10x magnifications to view the mineralogy and textures of 15 standard 30µm polished, uncovered thin sections. Samples ranged from ultramafic unserpentinized materials, to carbonate precipitates of hyper-alkaline springs. Images were captured of both hard rock thin sections and diatoms using a DFC 295 Camera.

Carbon coated thin sections were made to view carbonate and ultramafic material using a JEOL JSM 7000F field emission high resolution scanning electron microscope (SEM) analysis with an energy dispersive X-ray spectroscopy (EDS) attachment at the University of Canterbury. Irregular samples were dried for ~ 7 days in a 90° oven and mounted onto resin stands to provide natural surface mineralogical information of carbonate nodules. Images were captured of the surfaces of these irregular samples using both EDS and cold stage backscatter electron (Robinson) attachments.

5 Results

5.1 In-field observations

The Red Hills area consists of a large up-thrust plateau of unserpentinized ultramafic material, which is in faulted contact with younger sedimentary units of the Maitai Group. The Maitlands Stream traces this fault line upon which serpentinization is common. Following topographic controls, fluid flow runs from The Plateau (elevation 1160 m) down toward the Maitlands Stream (elevation ~860 m). Although equal sampling resolution was initially intended at both The Plateau and near the Maitlands Stream, surface features indicative of potential serpentinization activity were typically close to fault zones near the Maitlands and tributary streams, therefore more attention was dedicated to these areas.

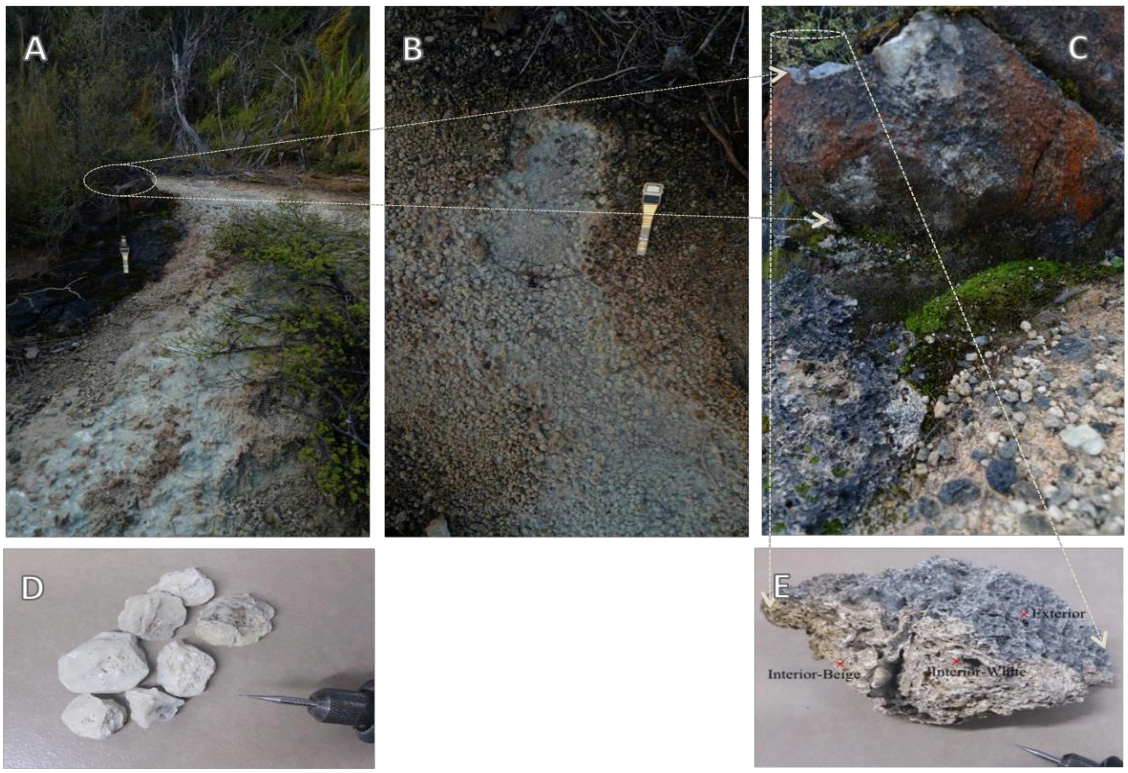

Figure 5.1: Carbonate precipitates at the hyper-alkaline site MHS. Image A, C and the circle outlined in E represent different scales of a porous older carbonate deposit adjacent to the hyper-alkaline spring. Image D shows the small fresh carbonate nodules precipitating from within the water, observed in image B, which is where the spring discharges. A drill piece (measuring 40mm long) is provided for scale in D and E. The watch for scale in A and B is 22cm full length (image A) and 15cm half length (image B).

Spot sampling of gas analyses was completed at 25 different locations with 1 location, named the Maitlands Hyper-alkaline Spring (MSH), emitting CH_4 in concentrations above background. Results focus on emissions at MSH, and the CH_4 and CO_2 flux of all other sites can be observed in Appendices 2 and 3. The MHS, observed in Figure 5.1, is situated on the main walking track ~100 m elevation above the Maitlands Stream. The spring emits a flow of approximately 0.5 L/s from a localised ~1 m^2 area. It seeps ultrabasic waters (pH 11.6) in which sporadic bubbling was observed during summer field sampling. Carbonates precipitate within the reduced waters in the form of nodules and amorphous deposits.

Throughout the field area a variety of amorphous material was observed seeping from cracks, fissures and soils horizons. In some steep river valleys of more resistant geology (i.e. north of hyper-alkaline site MHS), a white milky seep frequently emits from small fractures in the rock (Figure 5.2) and seeps into surface waters without forming obvious precipitates.

Figure 5.2: Calcite seeps from Mg-HCO_3 type waters. These are more predominant in steeper river valleys of higher flow.

In other areas of gentler gradient, where underlying geology is less brittle and more easily eroded, weathered and sheered, a range of amorphous materials seep from the walls above small stream flows. Variations include a beige/cream amorphous deposit, precipitating in brittle terraces both above and within the water (Figure 5.3 A). More commonly a red species covered with a rainbow oil-like sheen seeps from the soil horizon of the eroded streambed. This often forms in conjunction with a black, magnetic crispy amorphous precipitate (Figure

5.3 B and C). These beige, red and black precipitates are furthermore referred to as 'amorphous material'.

Figure 5.3 : Amorphous material precipitating from Mg^{2+}-HCO_3 type waters in tributary streams to the Maitlands River (**Figure 4.1**). Temperature probe in image A is 10 cm length. Image A is an amorphous carbonate/magnesium precipitate. Image B is a red amorphous material with a rainbow-like sheen. Image C is a black brittle precipitate which shows magnetic properties.

5.2 Gas

5.2.1 Concentration and Flux of Seeping Gas

Numerous studies in ultramafic environments have suggested the importance of faulting and other permeable physical structures (e.g. stream beds, geologic contacts) in the transport of fluids and gases (e.g. Marques et al. 2008; Etiope et al. 2013a). In light of these observations, two gas sampling transects were conducted perpendicular to: 1) the Maitlands Stream Fault and 2) a tributary stream on The Plateau (transects observed running west to east in Figure 4.1). Figure 5.4 plots the concentration of CH_4 (purple) and CO_2 (green) developed in the closed-chamber at points along the transect line for both locations at 15 minutes (dotted line) and 30 minutes (solid line) accumulation time. Results show a maximum CH_4 concentration of 2.6 ppm at the Maitlands Stream Fault, and 2.1 ppm at The Plateau. Minor concentration increases are observed at transect distance 10-20 m on the Maitlands Stream Fault, and at 60 m on The Plateau. Although no obvious deviations from background flux are observed on these particular transects, the complexities associated with permeability at fault zones means that these results are considered inconclusive.

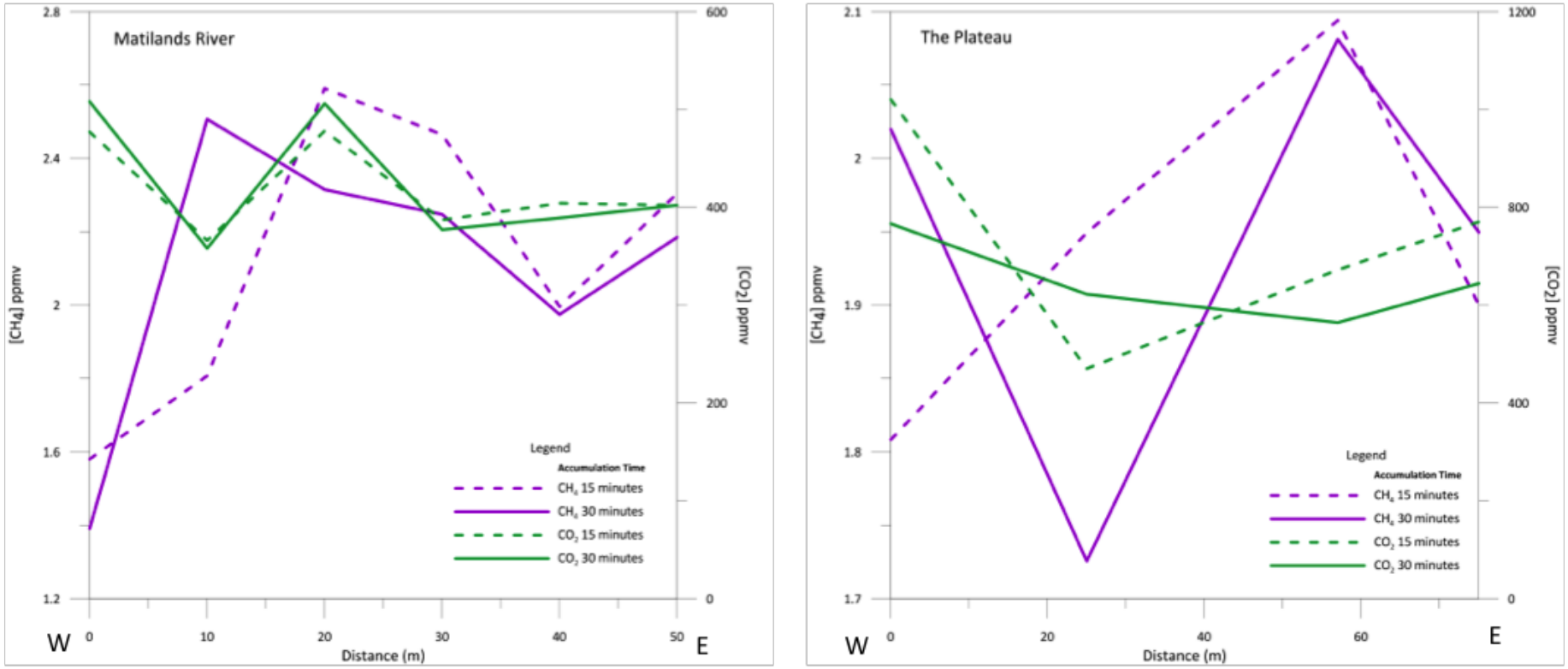

Figure 5.4: Transect lines at the Maitlands River (A) and The Plateau (B) show CH_4 (purple) and CO_2 (green) emissions at 15 (dotted line) and 30 (solid line) minutes accumulation time. Locations of the transects, which run west to east, can be observed in Figure 4.1.

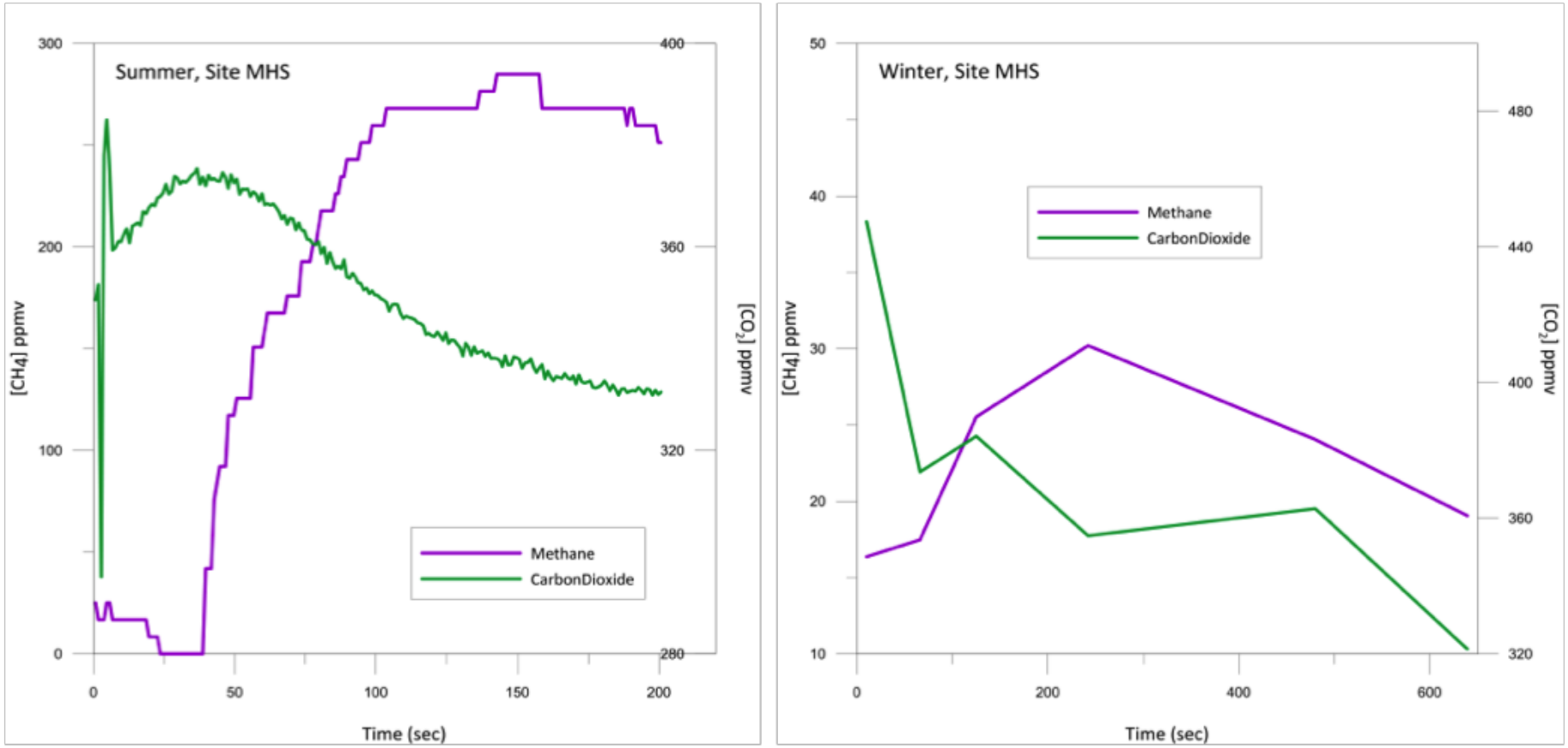

Figure 5.5 : Flux variation of CH_4 and CO_2 from summer (April) to winter (July), 2014. During summer, emissions of CH_4 were much higher, and the trend of increasing CH_4 and decreasing CO_2 is much more evident. Concentrations of CH_4 reach a peak of 285 ppm. In contrast during winter, concentrations of CH_4 were too low to detect on the WS-HS-IR CH_4 detector (detection limit 60ppm). As a result, 5 extractions were taken from the accumulation chamber and measured in the lab (using a Picarro G2201-i) to determine CO_2 and CH_4 concentrations as plotted here.

In contrast, results from spot sampling show active degassing at MHS, with a CH_4 flux of 17,031 mg m^{-2} day^{-1} in summer and 734 mg m^{-2} day^{-1} in winter. In Figure 5.5, the change in concentration of CH_4 and CO_2 in the closed chamber is plotted as a function of time for summer and winter field visits.

During summer, the CH_4 concentration increases by 209 ppm over 55 seconds, and in winter increases by 37 ppm in 242 seconds. Notable seasonal variation is evident in these results. The CH_4 detection limits of the WS-HS-IR CH_4 detector are 60 ppm, therefore, emissions at site MHS were unable to be measured in the field during winter low fluxes. Consequently, the graph built during winter sampling uses 6 accumulation chamber extractions over a 10 minute time period (as for isotopic analyses), which were later measured for CO_2 and CH_4 concentrations using CRDS methods in the lab. The resulting graph has a lower resolution of data points compared with that made from summer sampling, which plots measurements in one second frequencies from the West Systems gas analyser.

Table 5-1: Gas analyses at site MHS, and averaged data of all other sites visited in the Red Hills during summer and winter. Site MHS was the only site revisited in winter for gas analyses. For analyses at all other sites refer to Figure 4.1.

Gas Analyses	Average MHS Summer	Average MHS Winter	Average All Other Sites
$\delta^{13}C$ - CH_4	-33.0	-35.1	-44.8
$\delta^{13}C$ - CO_2	-5.9	-13.3	-14.4
$\delta^{18}O$ - CO_2	-10.5	-	-9.2
[CH_4] ppm	180.1	26.6	2.1
[CO_2] ppm	264.0	445.8	535.6
Flux (g $Fm^{-2}day^{-1}$)	17031.3	734.1	7.5

5.2.2 Isotopes of Seeping surface Gas

Figure 5.6 plots the δC^{13}-CH_4 against 1/concentration of CH_4. The atmospheric CH_4 signature is represented in blue as published by ESRL (publicly available at: http://www.esrl.noaa.gov). Seasonal variation is evident in data from both summer and winter sampling at site MHS. This site shows the highest concentration and least negative δC^{13}-CH_4 value, plotting in the upper left of the graph. The data shows a span of values with the δC^{13}-CH_4 becoming less negative with increasing CH_4 concentration.

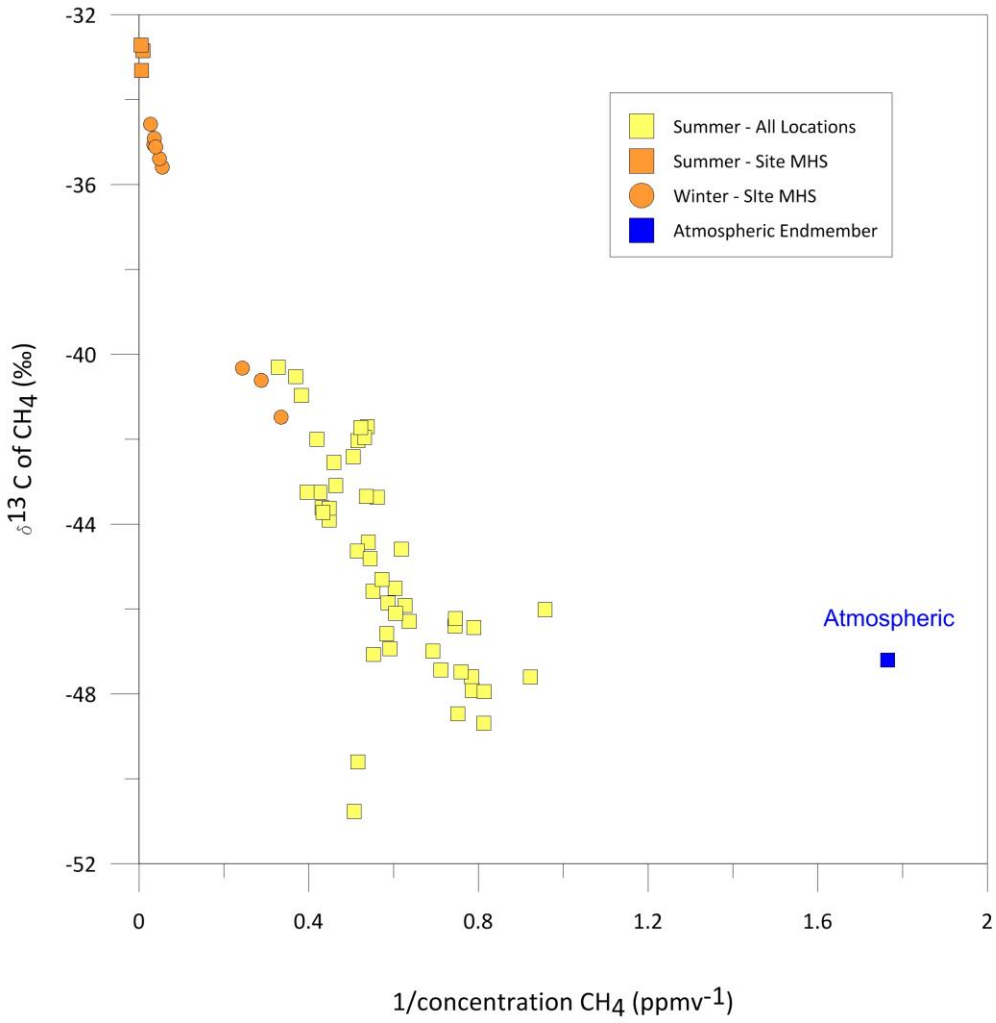

Figure 5.6: The δ^{13}C-CH_4 (‰) plotted against 1/[CH_4] in $ppmv^{-1}$ for all gas samples in the Red Hills. High fluxes of CH_4 are in the top left corner as produced by site MHS.

The δC^{13} values of CO_2 are plotted against 1/[CO_2] in Figure 5.7. Representative δC^{13}-CO_2 signatures of atmospheric (ESRL), geothermal (Sharp 2007) and biogenic (Whiticar 1999) origin are plotted for comparison. The majority of samples taken for this study display a linear correlation between biotic and atmospheric CO_2. In contrast, the low concentrations of CO_2 at site MHS plot in discreetly in the top right of the graph representing the most positive isotopic values. Values from site MHS are isolated from the three represented environmental signatures.

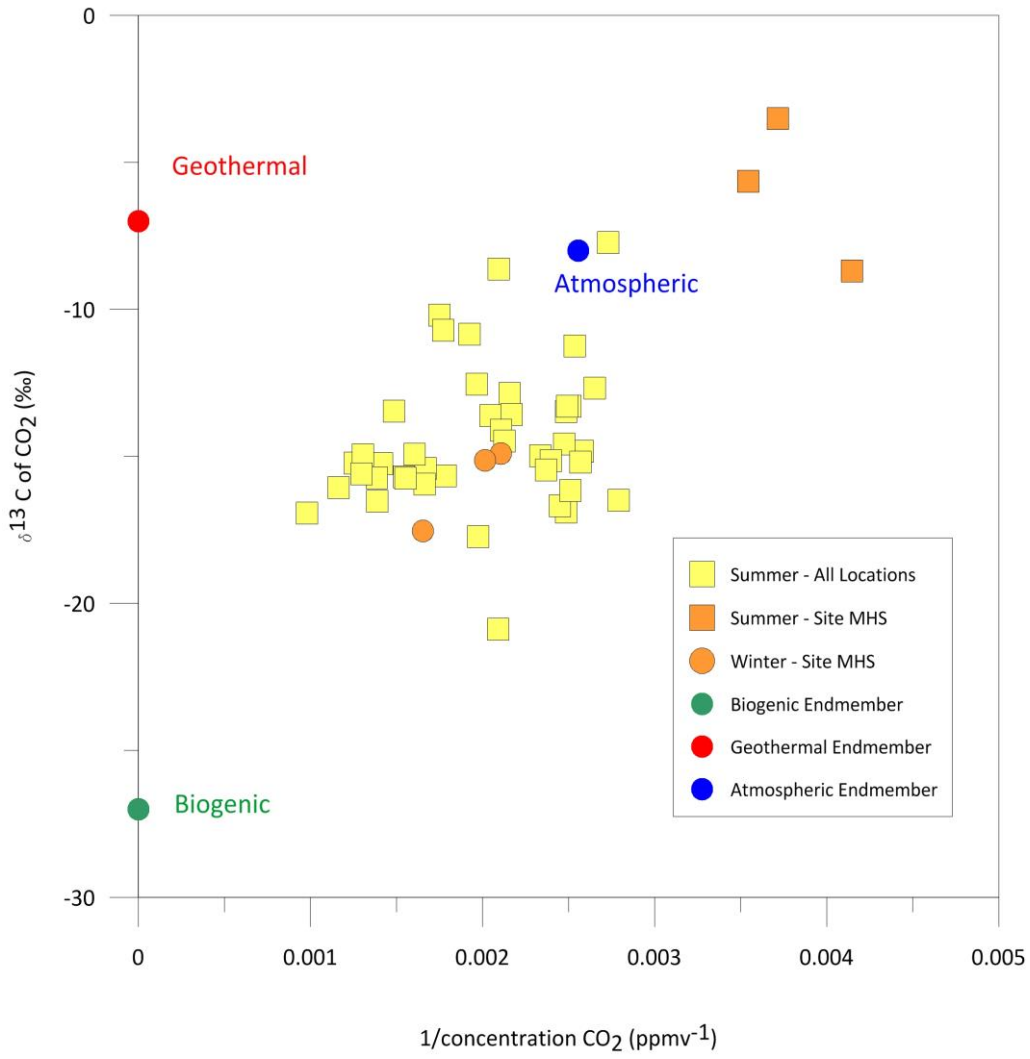

Figure 5.7 : The δC^{13}-CO_2 (‰) plotted against 1/[CO_2] in $ppmv^{-1}$ for all samples in the Red Hills. Environmental end members of biogenic, geothermal and atmospheric CO_2 are plotted for comparison.

5.2.3 Concentration of Dissolved Gas in Solution

Water samples for dissolved gas analyses at site MHS were extracted during winter fieldwork, where the ambient temperature was 10.4 °C and the water temperature was 7.4 °C. Concentration and isotopic values can be observed in Table 5-2. These are averages from three duplicate samples analysed at Victoria University Biogeochemistry School of Earth and Ocean Sciences (Canada). The CH_4 concentration of gas extracted from water measures 2.2 mg/L, CO_2 is 0.3 mg/L, and H_2 measures 0.7 mg/L.

Table 5-2 : Concentration and isotopic signatures of gas extracted from water at site MHS. Results are from laboratory analyses at Victoria University Biogeochemistry School of Earth and Ocean Sciences (Canada).

Concentration of Dissolved Gas - Winter (mg/L)	
CH_4	2.2
H_2	0.7
CO_2	0.3
Isotopes of Dissolved Gas – Winter (‰)	
δC^{13}-CH_4 (VPDB)	-37
δC^{13}-CO_2 (VPDB)	-23
δD-H_2 (V-SMOW)	-773
δD-CH_4 (V-SMOW)	-363.5

5.2.4 Isotopes of Dissolved Gas in Solution

As presented in Table 5-2, the $\delta^{13}C_{CH4}$ averaged -37 ‰ (VSMOW) and the $\delta^{13}C_{CO2}$ averaged -23 ‰ (VPDB). Figure 5.8 (adapted from Etiope & Lollar (2013a)) plots the values of $\delta C^{13}{}_{CH4}$ and δD-$_{H2}$ of dissolved gases in fluids from the Red Hills, and from other world-wide ultramafic environments. The boundaries suggested for volcanic-geothermal systems, alkaline rock intrusions and crystalline shields are drawn in with dotted lines. The signature of the gases at the Red Hills plots closely to the one other study undertaken in New Zealand at Poison Bay, Fiordland (Giggenbach & Lyon 1990). These values plot in the abiotic zone, which is drawn based on numerous previous studies. In particular, these values expand the boundaries suggested so far for land-based serpentinization.

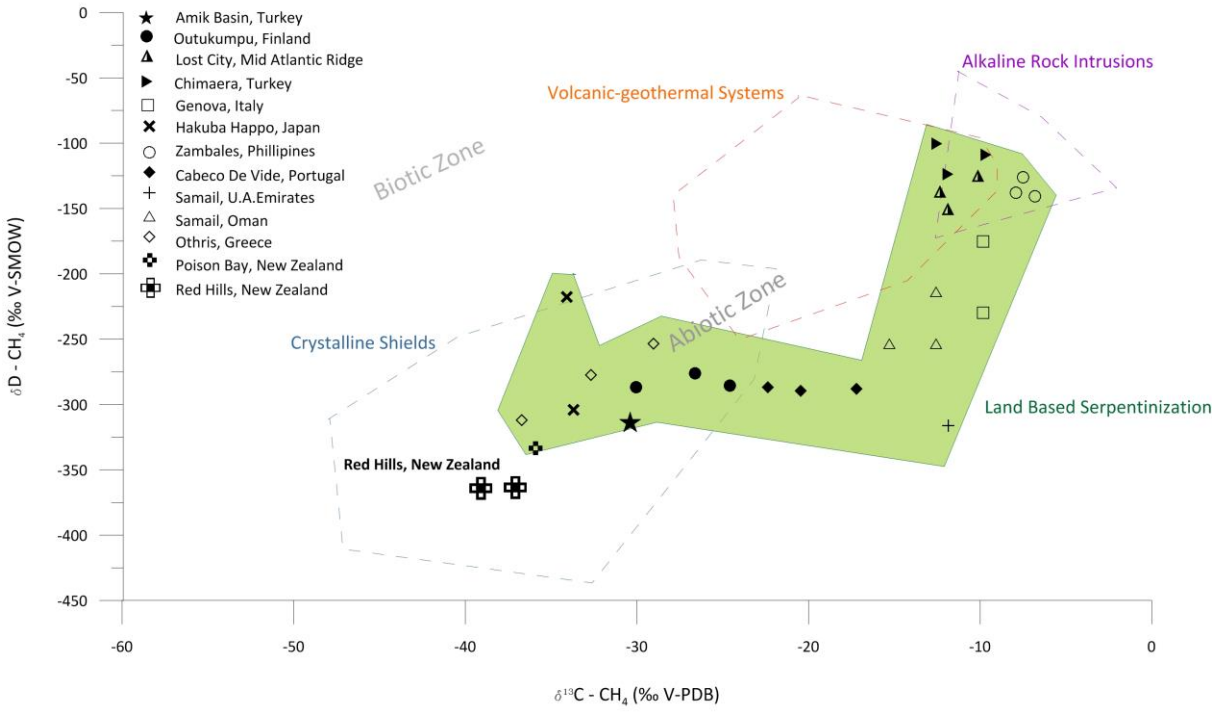

Figure 5.8 : The isotopic signature of CH_4 in the Red Hills, compared with worldwide studies. The signature sits outside the line of land based serpentinization as it is currently drawn. Data is summarized from multiple sources: Amik Basin, Turkey (Yuce et al. 2014); Outukumpu, Finland (Nyyssönen et al. 2014); Lost City, Mid Atlantic Ridge (Fruh-green et al. 2004); Chimaera, Turkey (Etiope et al. 2011); Genova, Italy (Boschetti et al. 2013); Hakuba Happo, Japan (Suda et al. 2014); Zambales, Phillipines (Abrajano et al. 1989); Cabeco De Vide, Portugal (Etiope et al. 2013b); Samail, Oman (Fritz et al. 1992); Orthris, Greece (Etiope et al. 2013a); Poison Bay, New Zealand (Giggenbach & Lyon 1990) and Red Hills, New Zealand (this study).

5.3 Water

5.3.1 Cation Analyses

Table 5-3 (general water chemistry) and Figure 5.9 provide a summary of the waters collected in the Red Hills. These are categorised into three different groups based on collection location: surface water, tarn water, and a hyper-alkaline spring. Surface water (plotted in green) represents all moving surface flow, from the Maitlands and tributary streams. Tarn water (plotted in purple) represents the isolated mountain ponds, which are not fed by rivers or streams. Hyper-alkaline water (plotted in orange) represents the basic spring at site MHS.

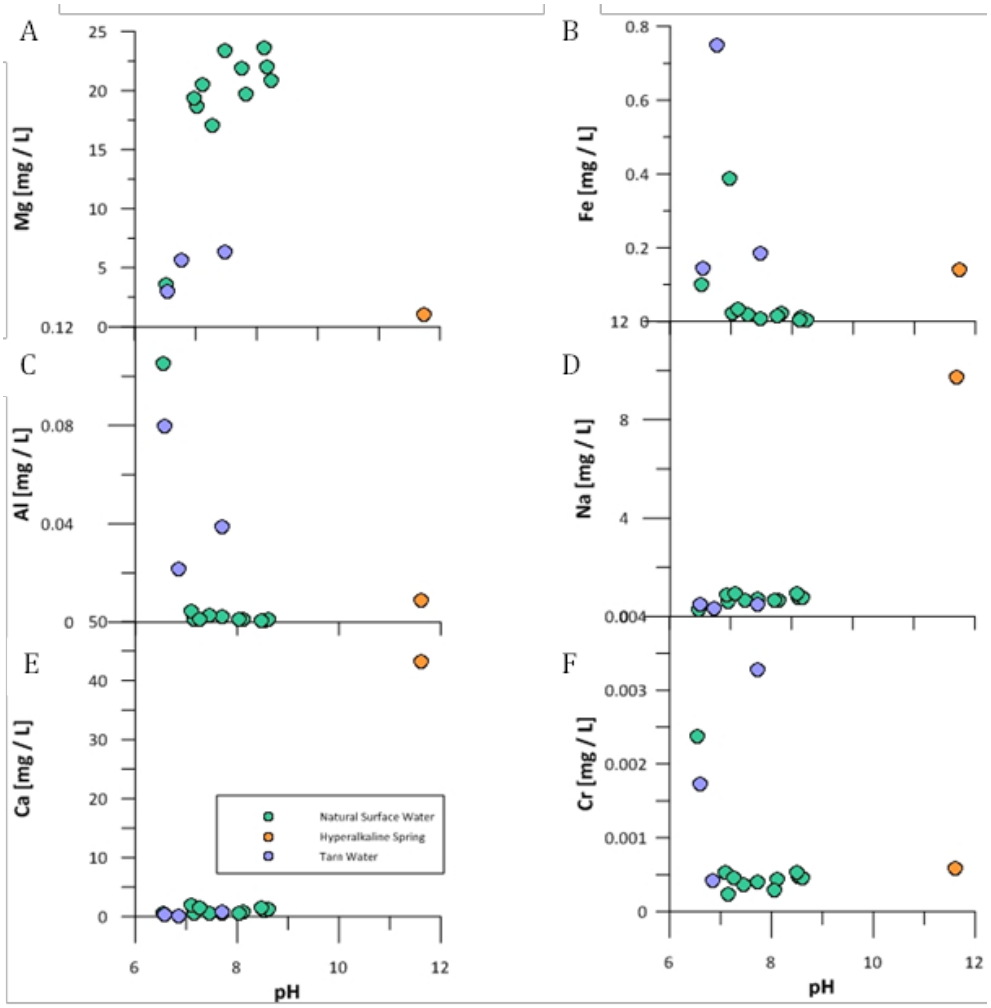

Figure 5.9: Total metal concentrations ($Ca^{2+,}$ Al^{3+}, Mg^{2+}, Fe^{2+}, Cr, Na^{+}) of the three water groups (surface, hyper-alkaline and tarn water) plotted against pH.

An average value of surface and tarn waters was taken and only one hyper-alkaline site was analysed. Figure 5.9 plots the total metal concentrations (Ca, Al, Mg, Fe, Cr, Na) of these three water groups against the pH. Surface waters are slightly higher than neutral at pH 7.8. They have an average Eh of -0.04 volts and are low in Ca, Na, Al and Fe. They are variably high in Cr and concentrated in magnesium. Tarn waters are the most acidic, with an average pH of 6.9. They have an average Eh of 0.01 volts, and are generally low in Mg, Ca and Na and concentrated in Al, Fe and Cr.

The hyper-alkaline waters are geochemically isolated from all other fluids, with a pH of 11.6 and an Eh measuring -0.25 volts. They show depletion in Mg, Al and Cr and display high concentrations of Ca (43 ppm), and moderate concentrations of Na (3.71 ppm).

The categorisation of tarn, surface and hyper-alkaline spring water is relevant for all but one sample. In Figure 5.9 images A, B, C and F, one sample of surface water displays qualities

similar to tarn water. This sample was collected at the highest elevation near The Plateau (Figure 4.1) representing the source water for a creek and is situated within 20 m to an isolated tarn.

Table 5-3 : Chemical and isotopic analysis of the 3 different kinds of waters present in the Red Hills. Dissolved gas analyses were undertaken only on hyper-alkaline waters of site MHS

Water chemistry	Hyper-alkaline Spring	Surface Waters (average)	Tarn Waters (average)
Temperature (°C)	10.80	11.70	11.60
Eh (V)	-0.25	-0.04	0.01
pH	11.62	7.80	6.90
Ca (mg/L)	43.20	1.00	0.32
Mg (mg/L)	1.00	18.40	8.60
K (mg/L)	0.74	0.07	0.07
Al (mg/L)	0.01	0.02	0.06
Fe (mg/L)	0.18	0.06	0.26
Isotopes			
$\delta^{18}O_{H2O}$ (‰ V-SMOW)	-9.36	-7.48	-4.38
δD_{H2O} (‰ V-SMOW)	-62.80	-50.74	-36.48

5.3.2 Isotopes of Water

The isotopic signatures ($\delta^{18}O_{H2O}$ vs. δD_{H2O}) of surface, tarn and hyper-alkaline spring water are displayed in Figure 5.10 in relation to the global meteoric water line (GWML). The values of surface and hyper-alkaline waters at the Red Hills plot closely to the GMWL; however, two data points from separate tarns on The Plateau and at the head of the Maitlands valley (Figure 4.1) plot distinctly to the right of the GMWL displaying more positive (enriched) $\delta^{18}O_{H2O}$ and δD_{H2O} values.

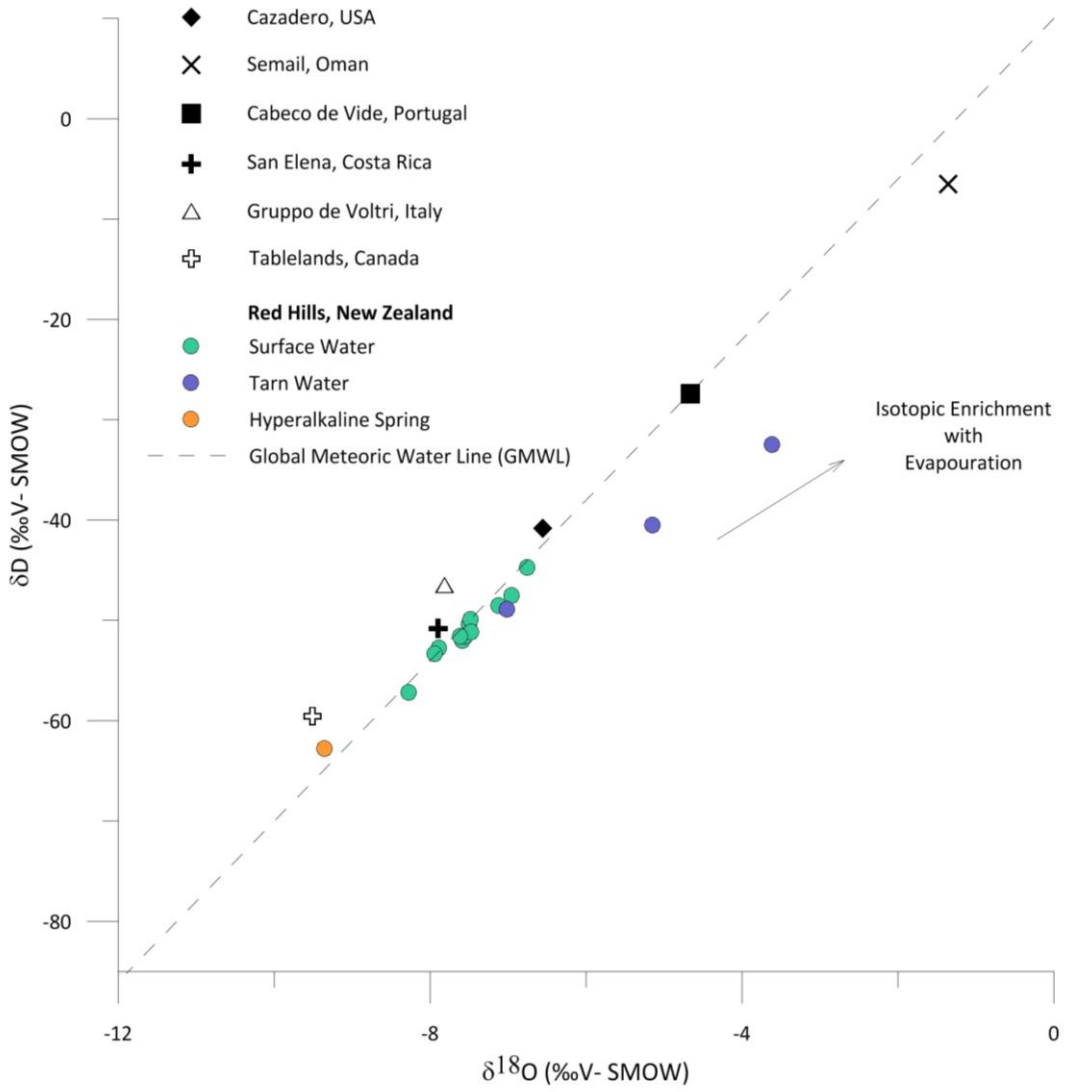

Figure 5.10 : The δO^{18} and δD values of hyper-alkaline (orange), surface (green) and tarn (purple) waters at the Red Hills, plotted next to the global meteoric water line (GMWL, in grey). An evaporation enrichment trend is observed in the surface and tarn waters. Other values from ultramafic systems in both temperate (e.g. USA, Italy, Canada) and arid (e.g. Oman, Portugal, Costa Rica) are plotted for comparison from summarized data in Sanchez-Murillo et al., (2014).

The surface waters display a moderate trend of isotopic enrichment (i.e. more positive isotopic values) with travel distance from the source waters to the Maitlands Stream. Waters from site MHS, although plotting in line with the GMWL, represent a different signature to other waters, offering much more negative values. The mean stable isotopic compositions of surface waters from other ophiolite systems in a range of climatic environments are plotted for comparison. Sites with arid climates (e.g. Oman) display less negative signatures. Those in more temperate climates plot more negative values, such as Canada and Italy. External data is summarized from Sanchez-Murillo et al. (2014).

5.4 Solids

5.4.1 Ultramafics

5.4.1.1 Mineralogy and Petrography

Petrological images of ultramafics and mafics of the Red Hills in Figure 5.11 show varying degrees of alteration in thin section. Images on the left are in plane polarised light, and those on the right are in cross polarised light. Heavy fracturing occurs within the unserpentinized harzburgite as observed in images A and B. An altered plagioclaise grain is evident within a micro-gabbro dike in images C and D. Many samples display abundant chromite grains (opaques) as observed within the heavily fractured harzburgite of samples E and F. Mesh textures are common in serpentinized samples along with extensive alteration as observed in images G and H. An unidentified oxide (observed as a black opaque elongate) has precipitated within a vein in images I and J, a serpentinized harzburgite sample.

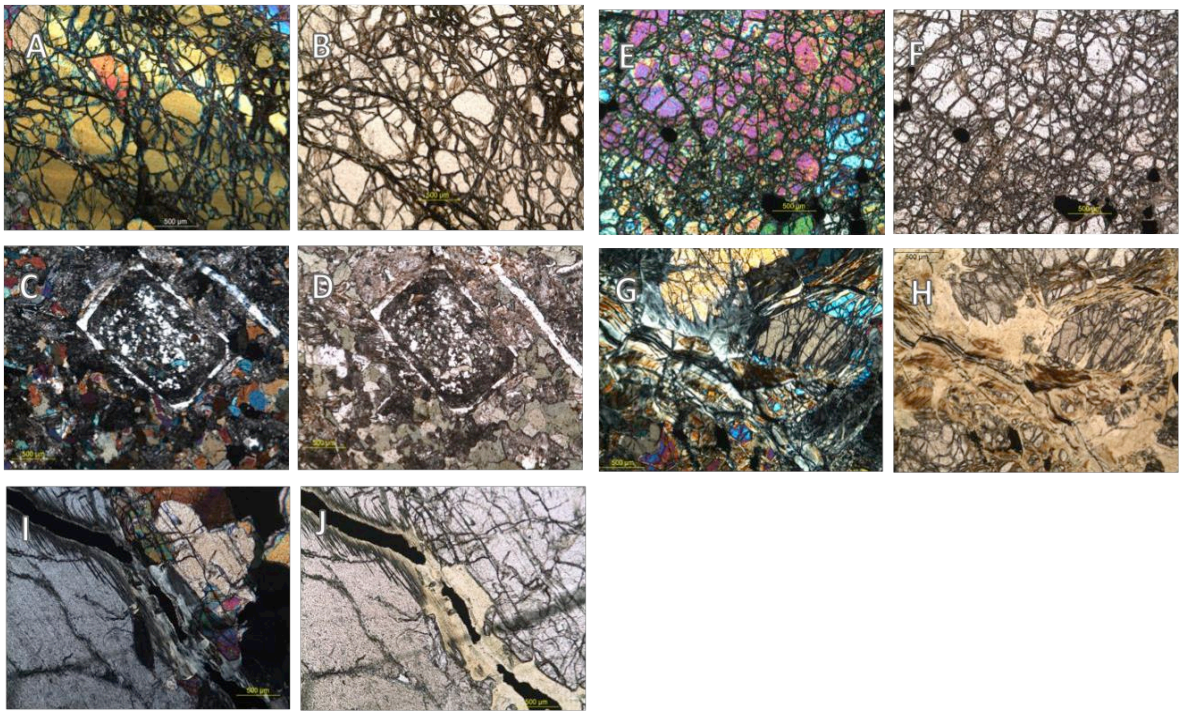

Figure 5.11 : Petrographic images of samples in the Red Hills. Images A, C, I, E and G are in cross polarised light, and images B, D, J, F and H are in plain polarised light. Identification of samples are as follows: A and B – fractured dunite; C and D – an altered plagiocliase crystal within a mafic dike; E and F – fractured dunite with numerous chromite grains; G and H – serpeninised dunite; I and J – elongate opaque precipitate within a serpentinised harzbugite.

5.4.1.2 SEM – Imaging

SEM imaging with a backscatter electron filter of harzburgite at 300 x magnification in Figure 5.12 A and B shows a highly resistant and fractured grain measuring 0.2 mm in length within a harzburgite sample. These grains are brighter with a backscatter electron (image B) filter, signifying a denser material. The shape and density of this grain suggest the presence of chromite.

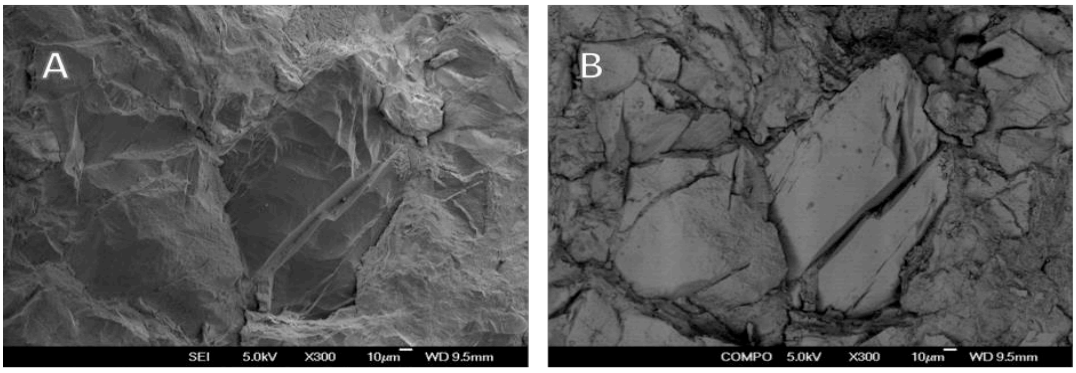

Figure 5.12: SEM imaging of chromite grains within harzburgite (A and B). Images on the left are using standard SEM settings, and those on the right use the backscatter detector.

5.4.1.3 SEM – EDS

Table 5-4 summarises the elemental composition of plotted areas (specified in Figure 5.13) within a harzburgite sample as measured using SEM-EDS. Analysis of the groundmass shows percentages of Mg, Fe, O and Si representative of a predominantly forsterite composition ($Fo_{0.9}$, $Fa_{0.1}$). Analyses of the oxides grains within this sample confirm the presence of the chromite spinel ($FeCr_2O_4$).

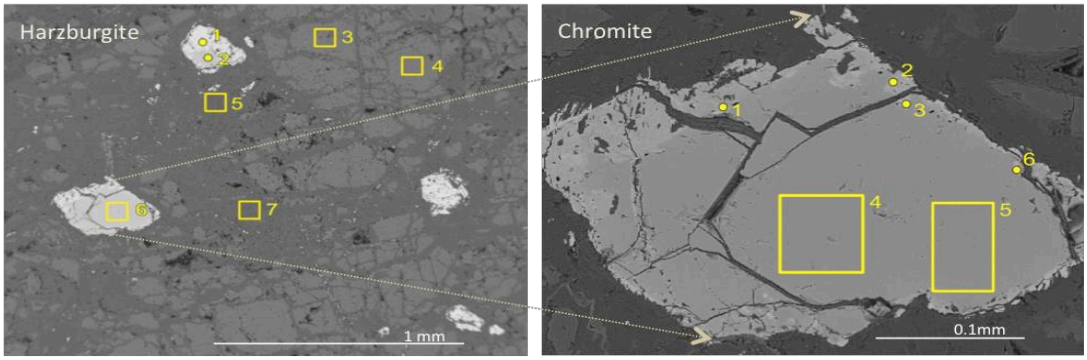

Figure 5.13 : Elemental analysis using SEM-EDS techniques of Harzburgite from the Red Hills. The chromite grain (right) is magnified and analysed in more detail from the harburgite sample (left). Elemental composition and interpretative mineral assignments for spot and area analyses are displayed in Table 5.4.

Table 5-4 : Weight percent of oxides within harzburgite of the Red Hills as analysed using SEM techniques. Refer to Figure 5.13 for areas of analyses.

Sample	Point Ref #	Oxide Weight %					Mineral Description
		MgO	SiO_2	Al_2O_3	Cr_2O_3	FeO	
Harzburgite	1	2.6		1.4	50	46.1	Chromite
	2	8.7		15.6	50.5	25.2	Chromite
	3	48.5	42.7			8.9	Forsterite (Fo 0.9, Fa 0.1)
	4	48.6	41.9			9.4	Forsterite (Fo 0.9, Fa 0.1)
	5	48	47.5			4.5	Forsterite (Fo 0.9, Fa 0.1)
	6	8.8		14.9	50.9	25.4	Chromite
	7	48.8	44.4			6.8	Forsterite (Fo 0.9, Fa 0.1)
Oxides within Harzburgite	1	6	0.5	12.1	47.5	33.9	Chromite
	2	2.3	0.3	0.4	46.1	51	Chromite
	3	3.3	0.3	4	47.7	44.7	Chromite
	4	8.3		14.8	52.6	24.3	Chromite
	5	8.8	0.5	14.2	51	25.5	Chromite

5.4.2 Carbonates

5.4.2.1 Mineralogy and Petrography

Petrological investigation of carbonates in Figure 5.14 shows varying crystalisation patterns between the two carbonates. Images A and B are of Carbonate 1, which is a younger small (~2 cm long) carbonate nodule precipitating from within hyper-alkaline waters (see nodules in Figure 5.1 D) of site MHS.

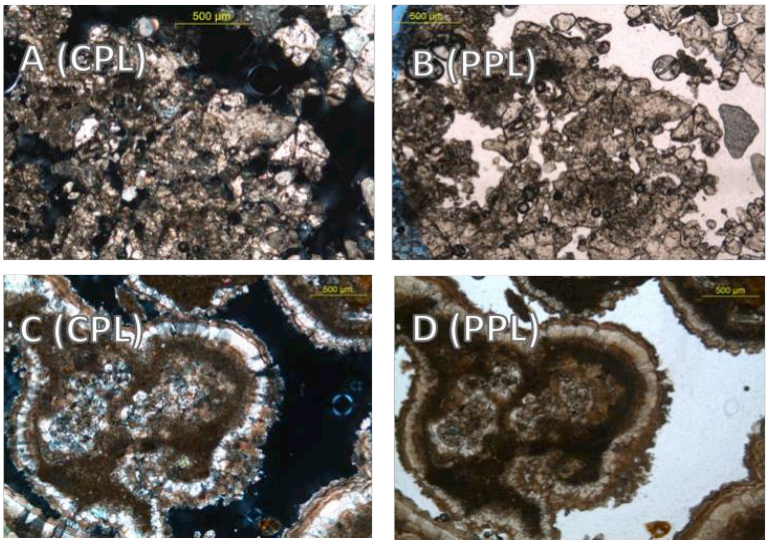

Figure 5.14 : Calcium carbonate deposits at hyper-alkaline site 2.11. Images on the left are in cross polarised light, and those on the right are in plain polarised light. Carbonate 1 (A and B) is one of many small (~4cm x 3cm) carbonate nodules precipitating from within the basic waters of site MHS (refer to Figure 5.1 B and D). Carbonate 2 is a porous older deposit found on the edges of MHS. Refer to Figure 5.1, image A, C and E to observe both carbonate forms.

Carbonate 1 displays calcium carbonate-like qualities (e.g. high birefringence; Figure 5.14, image A) in thin section, precipitating in a homogenous crystalline style. In contrast, Carbonate 2, observed in images C and D, precipitates in distinctive layers of white, beige and brown. This sample is a porous older deposit extracted from a large rock adjacent (not submerged) to the hyper-alkaline spring at site MHS.

5.4.2.2 SEM Imaging

Figure 5.15 shows SEM imaging of Carbonate 1 (younger nodules) at site MHS. Images with SEI labelled on the black band (bottom of image) are taken with the SEM, and those with COMPO use the backscatter detector, which makes heavier elements appear brighter during imaging. Microbes are present in varying abundances on mineral surfaces, as observed in images A and B, at 16,000 × magnification, measuring ~1 µm in length. Evidence of microbial habitation is shown in images C and D, where filaments/fibres stretch across the length of the sample. Both imaging methods are used on the same sample area for comparison, showing elemental (i.e. brightness) and textural differences between carbonate crystallisation and thread remnants of biologic activity. Two different crystal types are observed in image D; type 1 is smaller and hexagonal in habit; type 2 is blockier and provides a base habitat for which the type 1 crystal grows. Image E displays layering within the nodules, with finer crystallisation occurring between layers of a blockier fractured carbonate. A closer view of this blocky crystallisation is shown in image F.

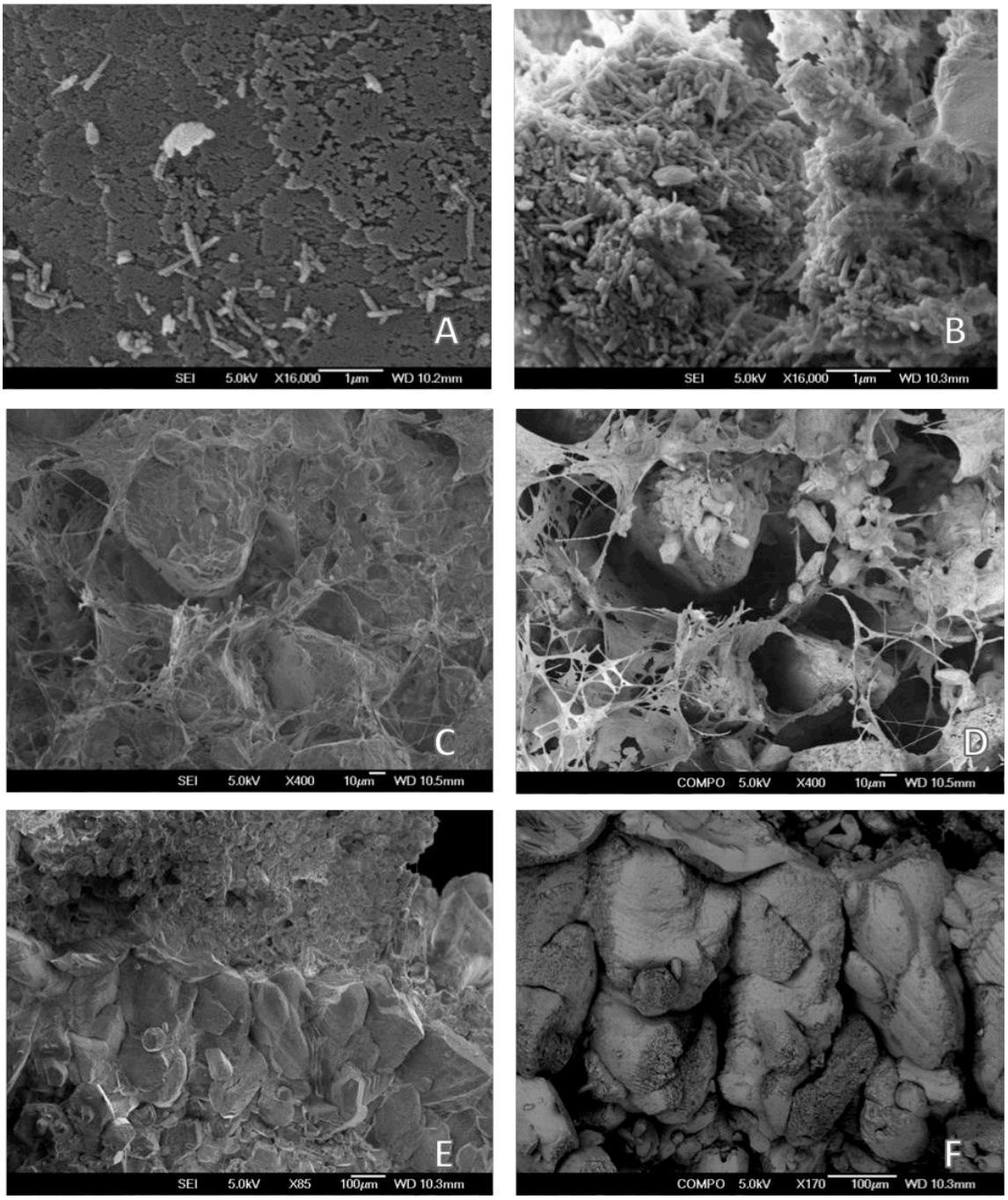

Figure 5.15 : SEM imaging of carbonate nodules at site MHS (images of the protolith *in situ* can be observed in **Figure 5.1** image B and D). Note the different scales. Images D and F (those with COMPO scribed in the image strip) are taken with a backscatter detector, which makes denser minerals / elements appear brighter. All other images use standard SEM functions.

5.4.2.3 SEM-EDS

In Figure 5.16 the areas which were analysed using SEM-EDS are displayed. Both Carbonate 1 (younger small nodules) and Carbonate 2 (older porous deposit) from site MHS were investigated. General observation of imaging alongside EDS analyses shows a notable difference in composition between the two samples. Carbonate 1 has a composition

consisting entirely of calcium carbonate. In contrast, Carbonate 2 shows varying compositional layers, from calcium carbonate to a more Mg-rich layer, which as observed in Table 5-5, shows mineralogical proportions most similar to forsterite (Mg_2SiO_4). This layering is also observed in the mineralogy of Figure 5.14, images C and D.

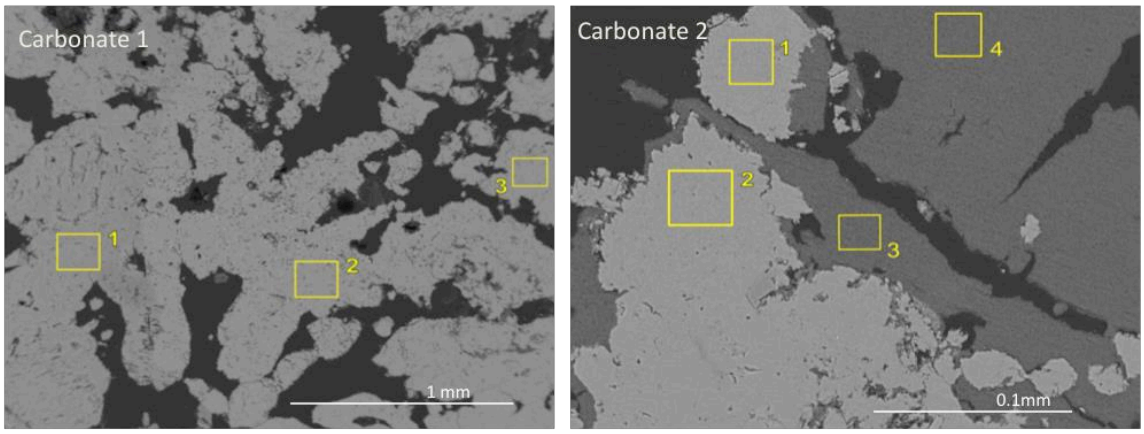

Figure 5.16: Elemental analysis using SEM-EDS techniques of two separate carbonate samples. These can be observed in-situ in Figure 5.1. Carbonate 1 is a fresh small nodule precipitating in hyper-alkaline waters (Figure 5.1, image B and D), and Carbonate 2 is an older, more porous sample adjacent to site 2.11 (Figure 5.1, image A, C and E). Elemental composition and interpretative mineral assignments for area analyses are displayed in Table 5-5.

Table 5-5 : Weight % of oxides within carbonates of the Red Hills as analysed using SEM techniques. Refer to Figure 5.16 for areas of analyses.

Sample	Point Ref #	Oxide Weight %						Mineral Description
		CaO	MgO	SiO_2	$Al2O_3$	FeO	Cl	
Carbonate 1 Fresh Nodule	1	99.2	0.7		0.1			Vaterite / calcite
	2	99.7	0.3					Vaterite / calcite
	3	100						Vaterite / calcite
Carbonate 2 Porous Older Carbonate	1	100						Vaterite / calcite
	2	100						Vaterite / calcite
	3		42.7	49.2		7.2	0.9	Forsterite (Fo 0.9, Fa 0.1)
	4		42.4	49.3		8.3		Forsterite (Fo 0.9, Fa 0.1)

5.4.2.4 Isotopes

Isotopic values of $\delta^{18}O_{CaCO3}$ and $\delta^{13}C_{CaCO3}$ from the two forms of carbonates are summarised in Table 5-6 and plotted in comparison with carbonates of other ultramafic systems in Figure 5.17.

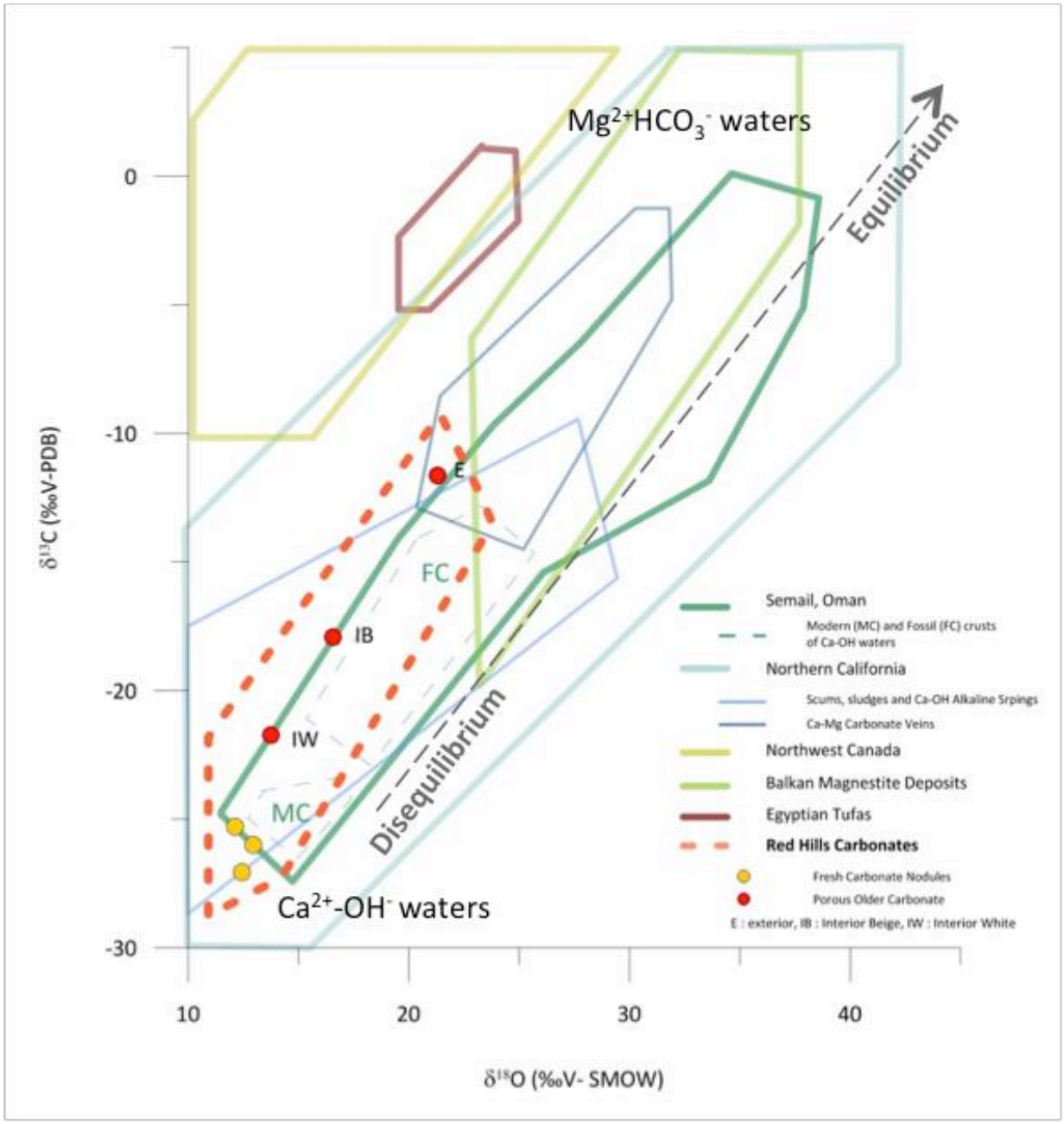

Figure 5.17 : The isotopic signature of two different forms of carbonates observed at site 2.11 in the Red Hills, compared with other carbonates from ultramafic systems world-wide. Data plots closely to that of northern California. The areas of $Mg^{2+}HCO_3^-$ and Ca^{2+}-OH^- waters are shown, including a trend line of the evolutionary process between the two. Modified from Kelemen et al. (2011).

The 'Fresh Carbonate Nodules' refer to Carbonate 1 and the 'Porous Older Carbonates' refer to Carbonate 2. Carbonate 2 uses data extracted from three sampling locations within the rock in Figure 5.1, images C and E. These sampling points are specified as 'Interior Beige', 'Interior White' and 'Exterior'. This rock was removed from a massive deposit situated adjacent to the hyper-alkaline spring at site MHS - presumably an older deposit. 'Fresh Carbonate Nodules' (viewed in-situ in Figure 5.1 B) display an average $\delta^{13}C_{CaCO3}$ value of -

26.1 (‰V-PDB) and an average $\delta^{18}O_{CaCO3}$ value of 12.9 (‰V-SMOW). All three samples measure closely to this average. In contrast, the isotopic signatures of different areas within the 'Porous Older Carbonate' show a linear trend of increasing of $\delta^{18}O_{CaCO3}$ and $\delta^{13}C_{CaCO3}$ values from the interior to the exterior of the sample. Also, the isotopic values of the Older Porous Carbonate are much higher than the Fresh Carbonate Nodules. All Red Hills carbonates plot in a similar zone to 'sludges' and 'scums' from Ca-OH alkaline springs in Northern California (Neil & Barnes 1971).

Table 5-6 : Isotopic analyses of carbonate samples. Exterior, Interior White and Interior Beige refer to three zones of extraction on a hand specimen named Carbonate 2 (C2) from site MHS. Small Nodules refer to Carbonate 1 (C1), which are ~2 cm long deposits precipitating from within hyper-alkaline water (Carbonate 1).

Carbonate Sample	Image Reference	$\delta^{13}C$ (‰V-PDB)	$\delta^{18}O$ (‰V-SMOW)
Exterior (C2)	5.2 A & B	-11.6	22.0
Interior White (C2)	5.2 A & B	-21.7	14.2
Interior Beige (C2)	5.2 A & B	-17.9	17.1
Small Nodule (C1)	5.2 C & E	-27.1	12.8
Small Nodule (C1)	5.2 C & E	-26.0	13.4
Small Nodule (C1)	5.2 C & E	-25.3	12.5

5.4.3 Amorphous Material

5.4.3.1 SEM Imaging

SEM imaging of amorphous magnetic material shows varying degrees of microbial habitation. This sample can be observed *in situ* in Figure 5.3, image C. SEM observations in Figure 5.18 C and D, show tube structures measuring ~70 μm in length. These tubes are longer than most bacteria (~1 μm in length), but may represent remnant structures left my microbial action, such as worm tubes. Certain areas are more concentrated in these trace structures, as observed in images E and in greater magnification in image F. Here the microbial structure measure ~90 μm in length.

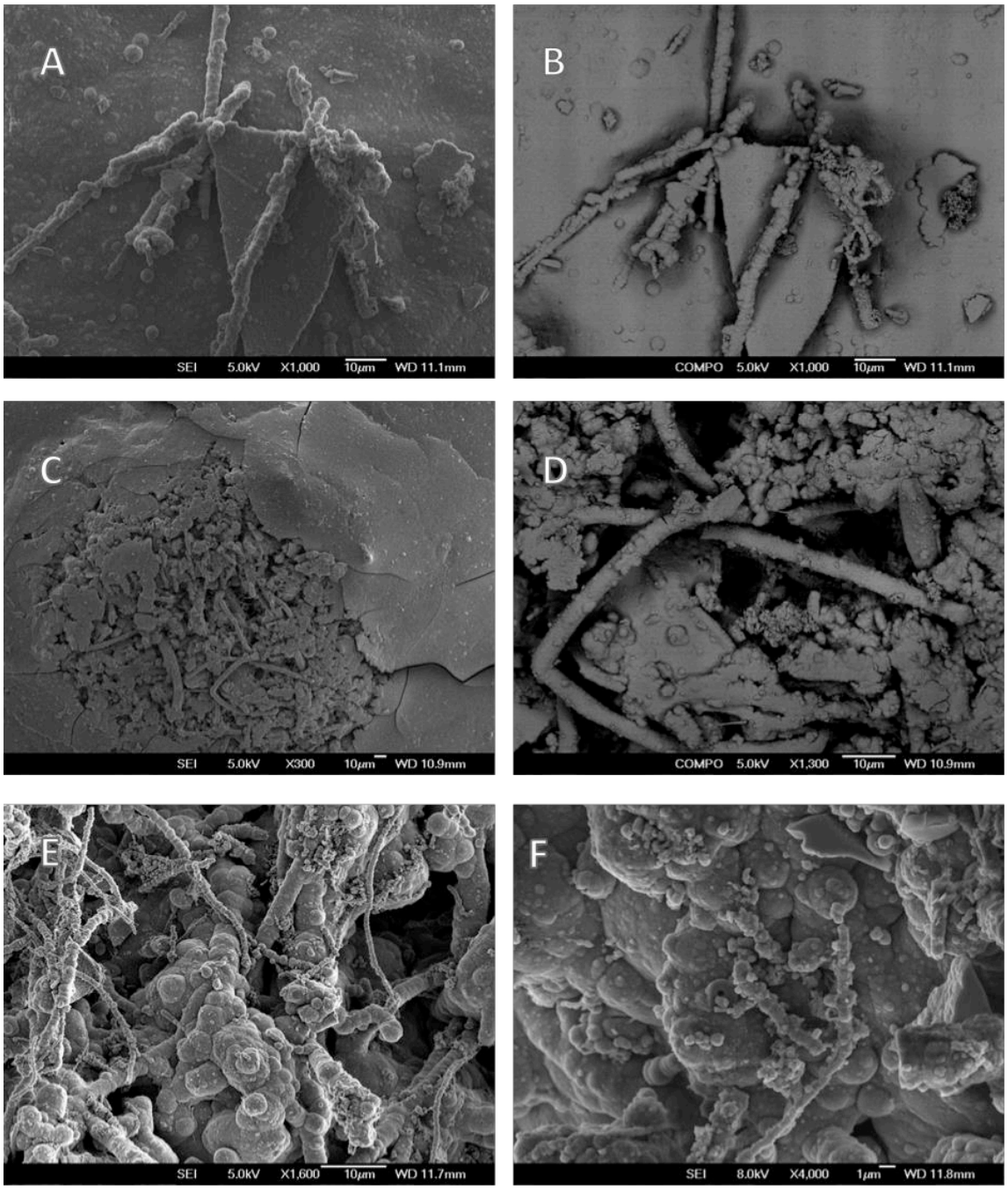

Figure 5.18: SEM imaging of black brittle amorphous material as observed in situ in Figure 5.3 C. Microbial remnant structures are present near crystalline edges (A and B) and in concentrated zones (C and D). D is a magnified image of C, note the scales. Spheroid crystal formations are evident in E and F, with microbial filaments ~20 μm concentrated on the mineral surface. Images on the left use standard SEM settings and those on the right use the backscatter detector, with the exception of F, which is a standard SEM image.

5.4.3.2 Isotopes

Table 5-7 summarises isotopic data from different forms of amorphous material. The red material, often associated with an oily sheen surface, has an average $\delta^{13}C$ value of -27.9 (‰ V-PDB). This is similar to the amorphous brittle black material, with a signature of -27.4. In

contrast, the white amorphous material produces a notably different $\delta^{13}C$ value of -18.9. It also shows a significantly higher carbon content at 12.3 %, compared with 2.9 to 8.1 % of amorphous red material and 2.1 % of the amorphous brittle black material.

Table 5-7 : Isotopic analyses of amorphous material observed in Figure 5.3.

Sample Name	Sample Description	$\delta^{13}C$ (‰ V-PDB)	% Carbon
2.2B	Amorphous red	-28.1	2.9
2.3A	Amorphous red	-27.7	8.1
2.3B	Amorphous white material	-18.9	12.3
2.3C	Amorphous brittle black	-27.4	2.1

5.4.3.3 Biology and DNA Sequencing

After culturing different samples of amorphous materials at varying temperatures, preliminary Gram staining identified a Gram-positive or Gram-negative organism. Falling into either category determines chemical and physical properties within the cell wall of the organism allowing the differentiation of bacterial species into these two main groups. A positive gram test stains the cell walls purple, and a negative gram test stains pink. After this preliminary diagnostic, samples could be sequenced using 16-RSNA – the results of which are summarised in Figure 5.19. The majority of samples (A → D) are different bacterial species which survive within the red amorphous material as observed in Figure 5.3 B. Image E is an isolated bacterium from black brittle amorphous material, observed in Figure 5.3 C. All bacteria have been cultured at different temperatures (stated on image). Species observed in images A and B have been isolated and cultured at 25 degrees. They are pink, determining a Gram-negative test and have been identified as *Pseudomonas fluorescens* (A) and *Janthinobacterium lividum* (B). Image C and D show a Gram-positive (purple) test result, and are identified as *Flavobacterium* sp (C) and *Bacillus cereus* (D). The purple stained bacterium in image E signifies a Gram-positive test result and is identified as *Staphylococcus epidermidis*.

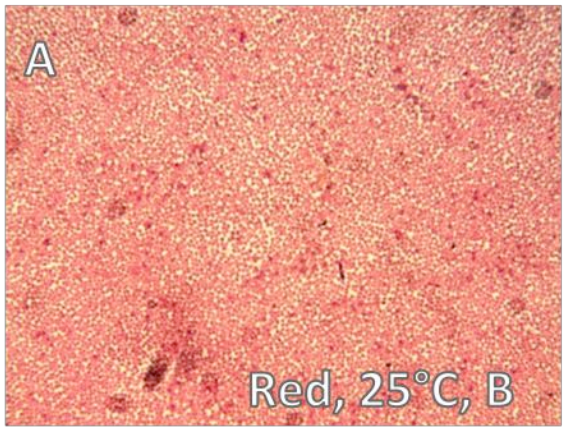

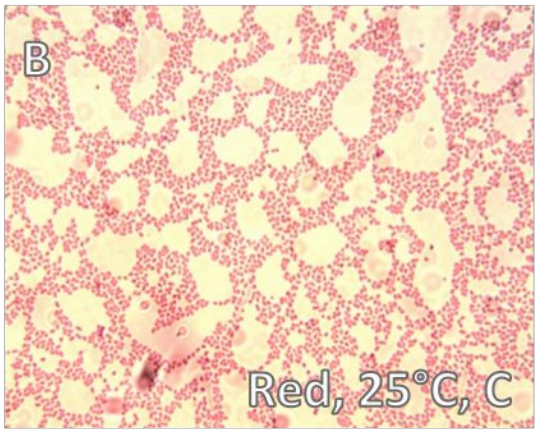

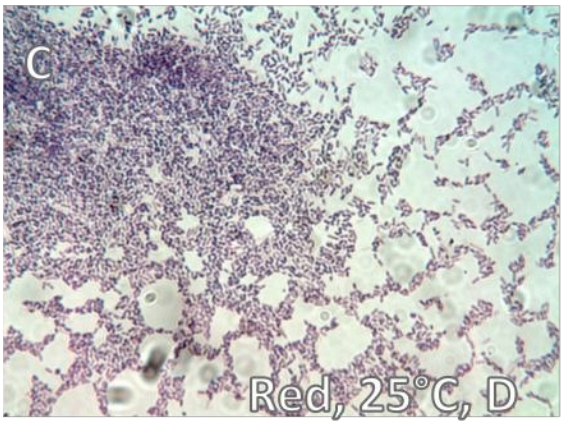

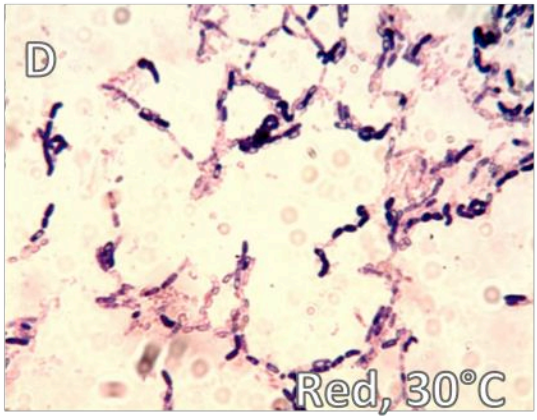

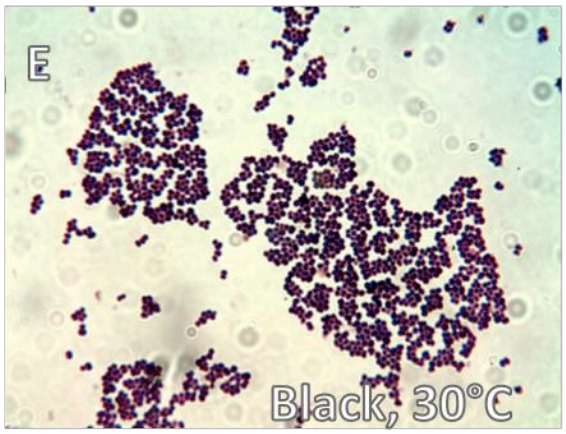

Image ID	Bacterial ID
A	*Pseudomonas fluorescens*
B	*Janthinobacterium lividum*
C	*Flavobacterium* sp
D	*Bacillus cereus*
E	*Staphylococcus epidermidis*

Figure 5.19: Cultured amorphous material from red amorphous material (labeled 'Red') and black brittle amorphous material (labeled 'Black'), observed insitu in Figure 5.3 B and C respectively. The temperature of cultivation is labeled on each image. These are sequenced for bacterial identification in the associated table. The different coloured samples represent a staining from the Gram test, where purple staining signifies a Gram-Positive response, and pink signifies a Gram-Negative response.

Diatoms are present within amorphous material of Figure 5.3 B, image B. Figure 5.20 defines the genre (and some species) of these specimens to be *Cymbella* (A) and *Navicula* (B). Other diatoms present within this sample are observed in Appendix 5. It is assumed that these species were living within the amorphous material during precipitation.

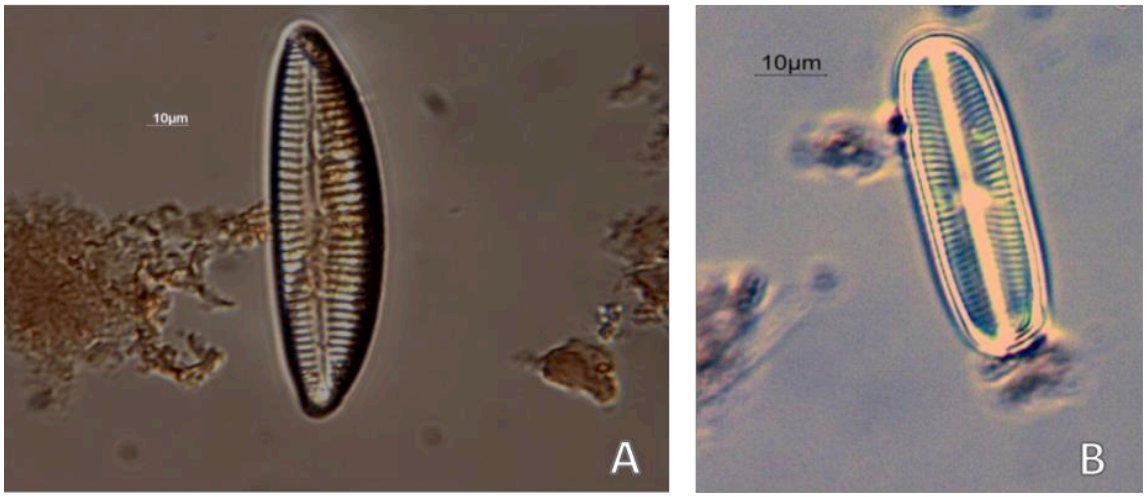

Figure 5.20: Diatom species present within amorphous material as photographed in Figure 5.3B. Genre are identified as A: Cymbella (similar to species affinis), B: Navicula (similar to species ignoa var. palustris).

5.4.3.4 *XRF Analyses*

Two types of amorphous material were analysed using XRF techniques; a red precipitate with a shiny rainbow oil-like sheen ('Red Shiny') and a black brittle magnetic precipitate which often occurred in conjunction with the former. Of the red material, which was abundant in many areas of the Red Hills (especially in summer), samples from two localities were tested. As observed in Table 5.8 this precipitate is mostly iron oxide (71.8 - 72.7 %), with minor amounts of silicon dioxide (7.5 - 10.1 %). The black brittle precipitate shows a similar composition, with slightly less iron oxide (67.8 %) and a higher percent of magnesium oxide (4.6 %). The concentration of chromium oxide in this black sample is notably high, at 1984 ppm. Sulfur is present in all samples, most concentrated in the Red Shiny precipitate (189-291 %).

Table 5-8 : XRF analyses of both black and 2 samples of red amorphous material, which is observed in situ in Figure 5.3.

Amorphous Material	Oxide Weight %										Elemental Concentration (ppm)	
	SiO_2	TiO_2	Al_2O_3	Fe_2O_3	MnO	MgO	CaO	Na_2O	LOI	Total	Cr_2O_3	S
Red Shiny	7.5	0.0	<0.2	72.7	0.1	0.2	0.7	<0.1	14.9	99.0	132.0	291.0
Red Shiny 2	10.1	0.0	<0.2	71.8	0.2	1.8	0.2	<0.1	14.9	99.0	423.0	189.0
Black Brittle	10.4	0.0	0.6	68.7	0.2	4.6	0.6	<0.1	14.0	99.6	1984.0	88.0

5.4.4 Vegetation

The plant species sampled in the Red Hills are all of C_3 type vegetation. Table 5-9 summarises the isotopic values, which are categorised as C_3 type using data from Sharp (2007). The region provides ideal conditions for C_3 plant species, which are typically present in areas with more arid summers, and are favoured at higher latitudes such as those in the Red Hills. Sample images are presented in Appendix 7 with associated isotopic values.

Table 5-9: $\delta^{13}C$ - CO_2 values from representative vegetation samples in the Red Hills

Sample	$\delta^{13}C$ (‰ V-PDB)	Sample	$\delta^{13}C$ (‰ V-PDB)
A	-28.09	F	-25.40
B	-29.94	G	-32.12
C	-29.43	H	-31.42
D	-26.86	I	-30.49
E	-29.76	J	-29.50

6 Discussion

6.1 Gas-Water-Rock Interactions in the Red Hills

The discovery of an abiotic CH_4-bearing seep at a localised hyper-alkaline spring (site MHS) confirms that present day active serpentinization is occurring in Red Hills. Analyses of the flux, its isotopic signature and the geochemical nature of interacting waters and precipitates at this site represents the first study of its kind in the southern hemisphere. This discussion will explore the results obtained from surface measurements, offering insight toward processes occurring at depth.

Methane emissions at site MHS total 17,031.3 mg m^{-2} day^{-1} in summer (March) and 734 mg m^{-2} day^{-1} in winter (July). Measured low fluxes during winter sampling may be a result of climatic controls (i.e. permafrost conditions, see Appendix 5) acting to inhibit near surface permeability and seepage of gas-rich fluids. The sporadic bubbling observed during summer sampling also suggests that the seepage of gas may be highly variable on a much shorter time scale, and that winter sampling occurred during a quiescent de-gassing period. Measurements taken over a larger timescale could determine if such variation is coincidental or truly seasonal in nature.

The temperature of CH_4 formation as a result of serpentinization is 69 °C. This was calculated from measured δD-CH_4 and δD-H_2 values (Table 5-2) using experimentally determined geo-thermometry equations in Horibe & Craig (1995), with an error of ±10–15 °C and assuming a system in equilibrium. It is possible that the low temperature H_2O–CH_4–H_2 system is not in isotopic equilibrium; therefore calculated temperatures are reflective of when the fluid was last in isotopic equilibrium. Additionally, as detailed in Proskurowski et al. (2006), the slower reaction kinetics in these low temperature environments creates complexities in the equations. Further study in low temperature environments is required to increase the robustness of these geothermometry calculations.

The isotopic signature of CH_4 is consistent with other worldwide abiotic CH_4-bearing sites (Figure 5.8), where gases are formed from radiocarbon-free C (i.e. ^{14}C content of zero) and are therefore assumed to originate from old, deep systems >50,000 years old (Etiope & Schoell 2014). Although the C is ancient, the depth and age of CH_4 formation remains

unknown. Observations regarding potential gas and gas-rich fluid pathways in the subsurface provide insight to these processes.

Other studies (e.g. Marques et al. 2008; Etiope et al. 2013a) have stated that CH_4-bearing Ca^{2+}-OH^- springs are typically located at or near faults, which act as conduits for upwelling deep aquifer water. Hyper-alkaline seeps are commonly observed in areas of high relief, and are often adjacent to a faulted ultramafic geological contact near a stream or river. The environment at which seepage occurs at the Red Hills is consistent with these sites. It was therefore hypothesised that fault and shear zones would concentrate gas movement due to ease of permeability; however as observed in Figure 5.4, gas emissions in the Red Hills do not directly utilise structural subsurface weaknesses. Transects across a major fault line (at the Maitlands Stream, now referred to as the Maitlands Fault) and an eroded permeable creek bed (on The Plateau) showed little deviation from background CH_4 values. It is very likely that these transects oversimplified the situation by assuming that the surface expression of the Matilands Fault represents a permeable subsurface pathway. A more realistic situation is that small spotted zones of permeability occur near (and not necessarily on) the fault boundary, inclusive of site MHS where active degassing occurs in a localised zone topographically higher (~100 m) than the Maitlands Fault (Figure 4.1). A schematic representation of gas and fluid migration through the ultramafic subsurface is presented in Figure 6.1, where field observations, relative locations and relevant chemical equations are provided. It is suggested that the Maitlands Fault acts as an interactive zone, concentrating gas-rich fluids and redirecting hydraulic flow (rather than acting as a direct conduit) allowing seepage of CH_4 and H_2 at site MHS.

Analyses of the surface waters in the Red Hills reveals three types of water, differentiated by cation concentrations (Figure 5.9) and isotopic signatures (Figure 5.10). These are described as surface waters, tarn waters and hyper-alkaline springs. As observed in previous geochemical modelling (e.g. Bruni et al. 2002), these water types can be further categorised into magnesium bicarbonate waters (Mg^{2+}-HCO_3^-) and calcium hydroxide (Ca^{2+}-OH^-) type waters.

Surface and tarn waters of the Red Hills are Mg^{2+}-HCO_3^- waters, with an average pH of 7.6 and an average Mg^{2+} concentration of 20.5 mg/L. These are comparable to surface waters in previous studies (Stamatis & Gartzos 1999; Etiope et al. 2013a; Neil & Barnes 1971; Barnes et al. 1978) regarding immature Mg^{2+}-HCO_3^- waters forming from the open system weathering of ultramafic rocks.

More specifically, the breakdown of forsterite (the magnesium olivine end-member) results in a Mg-rich fluid circulating within surface pathways from the equation:

$$\underset{\text{Forsterite}}{Mg_2SiO_4} + 4CO_2 + 2H_2O = \mathbf{2Mg^{2+}} + SiO_2 + \underset{\text{Bicarbonate}}{4HCO_3^-} \qquad \textbf{Eqn. 10}$$

Following this equation, in the absence of a notable CO_2 source (i.e. subsurface conditions) these waters may then evolve into ultrabasic waters such as those observed at site MHS. This has been observed in numerous ultramafic environments (e.g. Etiope et al. 2013b; Marques et al. 2008b). These hyper-alkaline waters, with a pH of 11.6 and a Ca^{2+} concentration of 43.2 mg/L, can be described as Ca^{2+}-OH^- type waters, representing a matured serpentinized fluid. The Ca^{2+} ions concentrated in these waters are likely liberated from the breakdown of pyroxenes within peridotites as observed in the equation:

$$\underset{\text{Diopside}}{3CaMgSi_2O_6} + 6H^+_{(aq)} = \underset{\text{Serpentine}}{Mg_3Si_2O_5(OH)_4} + \mathbf{3Ca^{2+}_{(aq)}} + H_2O + 4SiO_2 \qquad \textbf{Eqn. 11}$$

The Red Hills ultramafic mass contains very few Ca-bearing minerals (CaO: 0.06%, Table 3-1), therefore it is suggested that the concentration of Ca^{2+} cations in at site MHS requires long interaction times for disassociation to occur to such extents. These cations remain in solution because as they are not accommodated in the crystal lattice of serpentinite. In contrast, Mg^{2+} cations, which are abundant in the subsurface harzburgite (MgO: 37.7%, Table 3-1), are utilised during the formation of serpentine (Eqn. 11).

Reaction path modelling from Bruni et al. (2002) suggests this level of Ca^{2+} concentration can only occur in a system depleted in carbon (C), proposing that the concentration increase occurs in a system closed to CO_2. This implies the fluids at site MHS have circulated for a long time and at depths great enough to minimize atmospheric CO_2 inputs. Figure 6.1 shows a possible schematic scenario of subsurface and surface fluid movement at the Red Hills, complimented by key equations likely to occur during the chemical evolution of fluids.

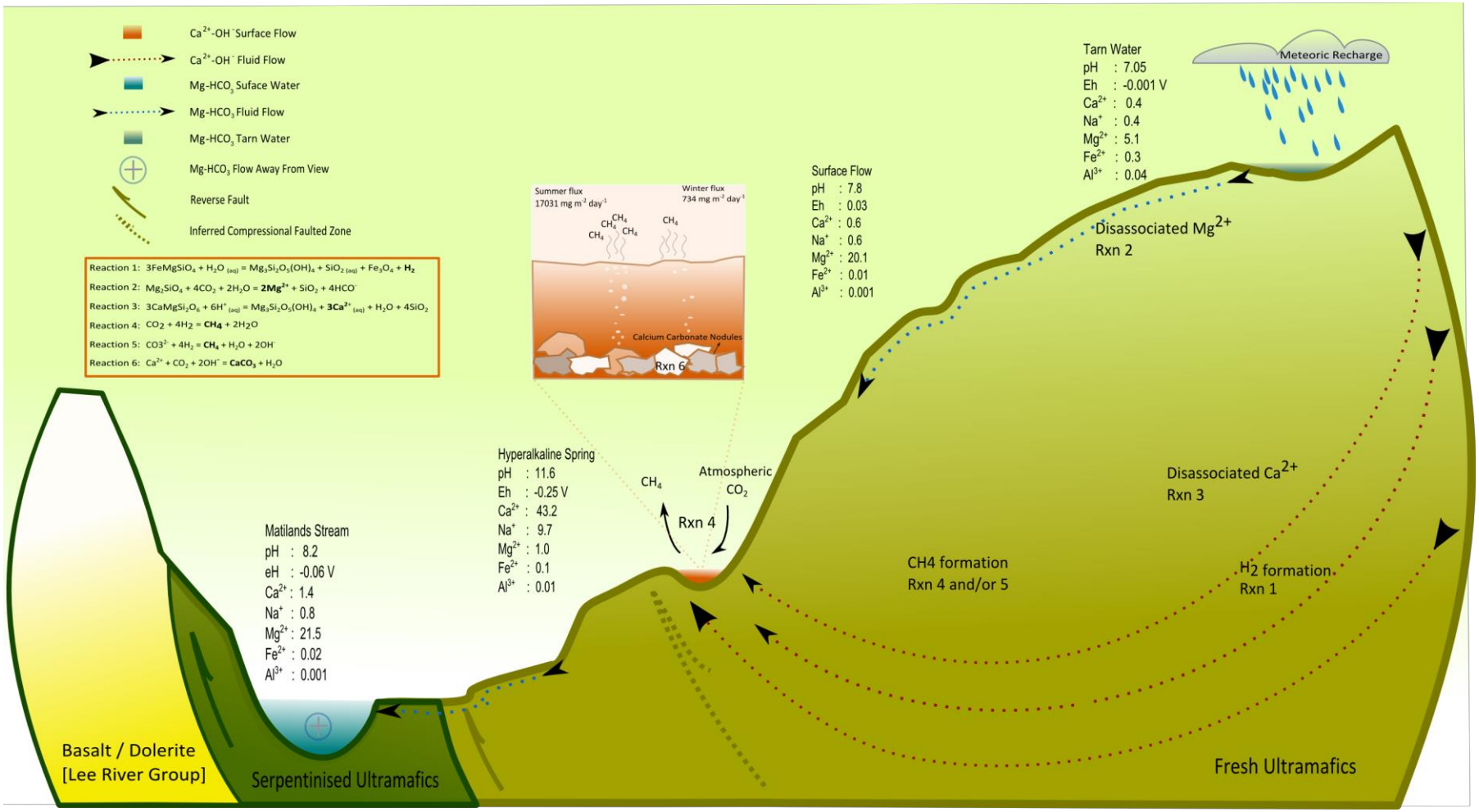

Figure 6.1: Schematic representation of fluid flow and gas chemistry in the Red Hills. The Maitlands stream, along with tarn and surface (tributary) streams are of Mg-HCO_3 type waters (coded in blue). The Hyper-alkaline spring displays notably different character, representing $Ca^{2+}OH^-$ type waters (coded in red). Diagram is not to scale.

The calcium hydroxide waters appear to originate from east of The Plateau, flowing slowly in the deep subsurface following hydraulic gradient. When they reach the inferred highly faulted and sheared zone, the fluids are redirected allowing seepage of CH_4-rich fluids at site MHS. Magnesium bicarbonate waters, representing a less mature fluid, flow mostly on the surface and eventually accumulate in the Maitlands Stream. The Maitlands stream has a marginally higher pH (8.2) and calcium concentration (1.4 mg/L) than its tributary streams (pH: 7.8, $[Ca^{2+}]$: 0.6), which is possibly an influence of runoff from the hyper-alkaline Ca^{2+} concentrated spring and potentially from other undiscovered springs.

The waters at site MHS are also concentrated in Na^+ ions (9.7 Mg/L), which is surprising when compared to the limited Na^+ available for breakdown with the harzburgite (NaO_2: 0.02 %, Table 3-1) and serpentinite (NaO_2: 0.01 %) of the subsurface. This once again suggests a prolonged interaction time between meteoric waters and the country rock at depth within the ophiolite, allowing the breakdown of albite within mafic geology (such as dikes and other intrusions) and encouraging disassociation of Na^+ cations for recirculation in meteoric fluids, similar to observations in Boschetti & Toscani (2008). An alternative origin of Na^+ is rain water, which in New Zealand contains ~ 4.7 Mg/L of Na^+ (Meder et al. 1991). These cations are not accommodated in any carbonate or serpentine precipitate and may therefore become concentrated in solution over long percolation periods.

As observed in Figure 5.10, all water samples originate from meteoric water, plotting on or very near the GMWL with the exception of two tarn water samples. These tarns are situated in exposed and for the most part, hydraulically isolated environments. This exposure results in greater evaporation rates and subsequent enrichment in heavier isotopes. The signature of hyper-alkaline spring waters at site MHS plot much nearer the GMWL, but in an isolated zone. They produce notably more negative $\delta^{18}O_{H2O}$ and δD_{H2O} values than surface and tarn waters. These values suggest the fluid is either much older and/or originates from a much higher altitude than other flows (Sharp 2007). This further supports that the hyper-alkaline spring water originates from a higher altitude east of The Plateau, and undertakes a slow, deep percolation in an environment with limited atmospheric CO_2 influence. Once these Ca saturated fluids reach the Maitlands fault, they resurface and are suddenly exposed to atmospheric CO_2, resulting in extensive carbonate precipitation.

6.2 Carbonate Formation

Carbonates commonly form in hyper-alkaline systems associated with serpenintization (Neil & Barnes 1971; Kelemen et al. 2011; Sanchez-Murillo et al. 2014; Clark et al. 1992; Boschetti & Toscani 2008). They are often observed as travertine terraces, calcite crusts, and as amorphous sludges in/near reduced water sources. In the Red Hills, two forms of carbonates precipitate upon a travertine terrace within Ca^{2+}-OH^- type fluid at site MHS; small nodules (i.e. Carbonate 1) and porous, weathered, blocky deposits (i.e. Carbonate 2). Also, a carbonate sludge with similar properties to magnesite forms within numerous Mg^{2+}-HCO_3^- surface streams, which are tributaries to the Maitlands Stream.

Calcite precipitation in neutral equilibrium systems generally occurs from Equation 12. In such environments, equal amounts of CO_2 are absorbed and formed resulting in a net zero influence on carbon emissions. In contrast, the hyper-alkaline Ca^{2+}-rich waters of site MHS promotes active carbonate precipitation during atmospheric CO_2 interaction from Equation 13. This process is unique to highly reducing conditions, where CO_2 is absorbed during calcite precipitation. In environments where CO_2 is limited (e.g. in the deeper subsurface) and fluids are reduced, CO_3^{2-} becomes the common source of carbon, as discussed in Etiope & Sherwood Lollar (2013).

$$Ca^{2+} + 2HCO_3^- = CaCO_3 + H_2O + CO_2 + H_2O \qquad \textbf{Eqn. 12}$$

$$Ca^{2+} + CO_2 + 2OH^- = CaCO_3 + H_2O \qquad \textbf{Eqn. 13}$$

The influence of precipitated carbonates within ultramafic systems has been illustrated in recent studies (Holm et al. 2014; Neubeck et al. 2014). Experimental results suggest that H_2 production is hindered by the precipitation of carbonates, which impact the effective reactionary surfaces of olivine, decreasing the dissolution rate in fluid. Carbonate oversaturated fluids at low temperature and pressure conditions were seen to produce less H_2 when compared with those reactions using carbonate under saturated fluids, due to the incorporation of Fe^{2+} into carbonates, silicates and metal hydroxides. This limited the available Fe^{2+} for oxidation into minerals such as magnetite, (a known catalyst to hydrocarbon synthesis) synchronously decreasing H_2 production (as observed in Eqn. 1). Theoretically, if carbonate precipitation and olivine dissolution all occurred in one stable system (as laboratory

experiments must assume) this experimental decrease in H_2 production may be observed; however the multistage process of ion disassociation in the Red Hills means that carbonate precipitation is likely to occur after the dissolution of olivine species. As a result, extensive carbonate precipitation at the surface site of MHS is not assumed to negatively affect H_2 production at depth in the Red Hills. If extensive carbonate precipitation occurs at depth, then it is likely that H_2 production is negatively impacted.

The two carbonate forms observed at site MHS vary in composition, as observed in Table 5-5 and Figure 5.16. Carbonate 1 (small nodule) can be classified as calcium carbonate ([CaO]: 99.2 %) with minor traces of magnesium ([MgO]: 0.07 %). The composition of Carbonate 2 (porous older deposit) is more complicated, displaying precipitation in layers of calcium carbonate and a forsterite-like silicate. As previously suggested, waters in the Red Hills have evolved through deep percolation and lengthy interaction from Mg^{2+} to Ca^{2+} rich fluids. This Mg silicate–bearing carbonate may be representative of surface mingling between Mg-HCO_3^- surface waters and Ca^{2+}-OH^- waters of deeper origin. This mingling is not evident in the present day system (i.e. no Mg^{2+}-HCO_3^- surface waters are flowing through or near site MHS), but precipitation textures suggest that the two water types have been in contact in the past. The term 'mingling' is used due to the lack of evidence supporting mixing of the two types of waters. It would be expected that if precipitates were formed in a system where Ca^{2+}-OH^- and Mg^{2+}-HCO_3^- waters mixed, the result would be a dolomite-type Ca^{2+}/Mg^{2+} deposit. In contrast, the layers evident in Figure 5.16 are chemically distinct.

Under current geochemical conditions at site MHS, a number of different minerals are theoretically supersaturated in the hyper-alkaline fluids. This is observed in Figure 6.2, where the saturation zones of different mineral species are plotted against pH as calculated using visual MINTEQ under conditions open to atmospheric CO_2 at 10.8 °C. At the present pH of the spring (i.e. pH: 11.6), hydromagnesite ($Mg_5(CO_3)_4(OH)_2 \cdot 4H_2O$), magnesite ($MgCO_3$), siderite ($FeCO_3$), hercynite ($FeAl_2O_4$) and calcite ($CaCO_3$) are all oversaturated. However, summarised results (e.g. SEM imaging, EDS and petrographic investigations) show strong evidence that the precipitates at this site are predominantly calcite, with very little evidence supporting the presence of other carbonate species. It is possible that the Mg and Fe species precipitate at a site downstream of the spring outflow, where $CaCO_3$ is a less dominant process.

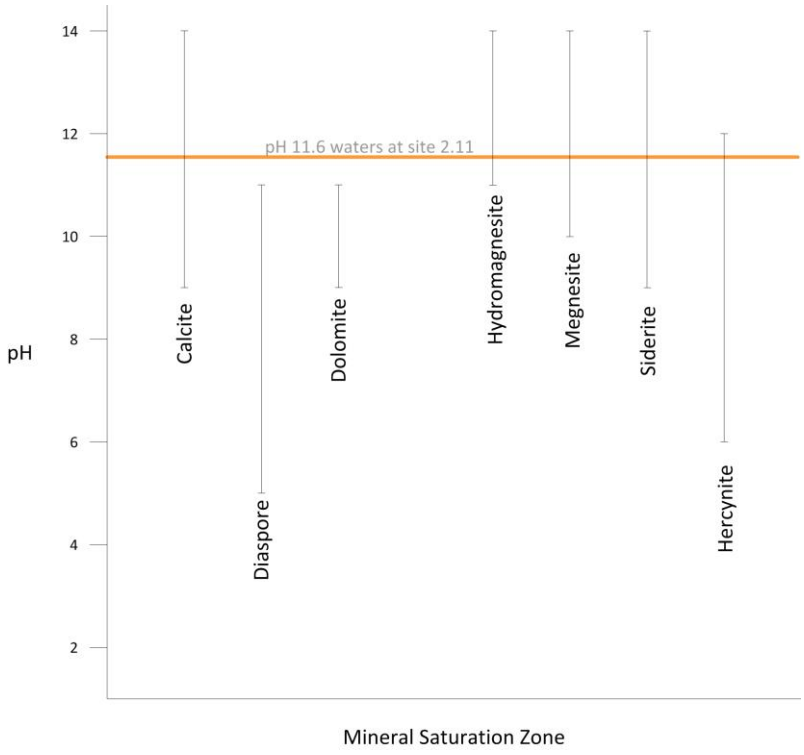

Figure 6.2: Saturation zones of different mineral precipitates, as calculated using Visual MINTEQ. The orange line represents the hyper-alkaline waters of site 2.11. Minerals crossing this line should, in theory, be precipitating in the system. System conditions entered were a water temperature of 10.8 °C, atmospheric CO_2 pressure of 0.00038 atm, and the cation concentrations of hyper-alkaline water as stated in **Table 5-3** (Al^{3+} : 0.008 mg/L, Ca^{2+} : 43.2 mg/L, Fe^{2+} : 0.14 mg/L, Mg^{2+} : 1.03 mg/L, Na^{+} : 9.7 mg/L). The one-parameter sweep function was used to model a variation in pH.

The stable carbon and oxygen isotopic composition of carbonate minerals in the Red Hills reflect the environment and conditions present at the time of carbonate formation. One of the key questions relevant to the interpretation of carbonate isotopic composition is: Did the carbonates form in isotopic equilibrium?

The isotopic composition of carbonates precipitating in hyper-alkaline fluids in the Red Hills are best explained as resulting from disequilibrium stable isotope fractionation. The $\delta^{13}C$ and $\delta^{18}O$ values of Carbonate 1 are 30.8 ‰ and 8.9 ‰ more negative than calcite formed under equilibrium conditions at 10 °C in the presence of meteoric waters from the Red Hills area (Table 6-1), assuming an atmospheric $\delta 13C_{CO2}$ value of -8.8 ‰ and a $\delta^{18}O_{H2O}$ value of -9.4 ‰ (http://www.esrl.noaa.gov). If, as suggested by Eqn. 12, the carbonates are formed from the uptake of atmospheric CO_2, the $\delta^{13}C$ and $\delta^{18}O$ values should fractionate in a similar manner to those of theoretical studies (Bottinga 1969; Bottinga 1966; Clark et al. 1992, see Eqn. 8 and 9). Calculated isotopic fractionation of $\delta^{13}C_{CO2}$ and $\delta^{18}O_{CO2}$ under equilibrium conditions should ideally result in a $\delta^{13}C_{CaCO3}$ value of 3.7 ‰ (V-PDB) and a $\delta^{18}O_{CaCO3}$ value of

21.8 ‰ (V-SMOW). The $\delta^{13}C_{CaCO3}$ and $\delta^{18}O_{CaCO3}$ values of the Red Hills Carbonate 1 average -26.1 ‰ (V-PDB) and 12.9 ‰ (V-SMOW).

Carbonate 2 shows a higher range of more positive values than Carbonate 1, but still displays large discrepancies from the predicted equilibrium values. The $\delta^{13}C$ and $\delta^{18}O$ values of Carbonate 2 are up to 25.5 ‰ (V-PDB) and 7.7 ‰ (V-SMOW) more negative than those predicted in an equilibrium system Table 6-1.

Table 6-1 : Summarised isotopic data from the Red Hills, with calculated idealised fractionation factors (using Eqn. 8 and 9) for comparison with systems in equilibrium.

Sample	$\delta^{13}C_{CaCO3}$ (V-PDB)	Fractionation Factor $\delta^{13}C_{CO2(g)}$-$\delta^{13}C_{CaCO3}$	$\delta^{18}O_{CaCO3}$ (V-SMOW)	Fractionation Factor $\delta^{18}O_{H2O(aq)}$-$\delta^{18}O_{CaCO3}$
Carbonate 1 (fresh nodule)	-27.1	-18.3	12.8	22.6
	-26	-17.2	13.4	23.1
	-25.3	-16.5	12.5	22.2
Carbonate 2 (porous older)	-11.6	-2.8	22	31.7
	-21.7	-12.9	14.2	23.9
	-17.9	-9.1	17.1	26.8
Atmospheric CO_2	-8.8			
H_20			-9.4	
Modelled Equilibrium Isotopic Conditions *	3.7	12.5	21.8	31.5

***** Calculated using the fractionation equations in Bottinga (1969) and Bottinga (1966). These used initial atmospheric $\delta^{13}C_{CO2}$ value of -8.8 ‰ and a $\delta^{18}O_{H2O}$ value of -9.4 ‰ (http://www.esrl.noaa.gov) at 10 °C.

These results demonstrate that carbonate precipitation at site MHS in the Red Hills represents disequilibrium stable isotopic fractionation. This disequilibrium likely results from aqueous kinetic effects enhanced by extremely reducing conditions (Clark et al. 1992; Cipolli et al. 2004). The hyper-alkaline waters encourage very rapid uptake of atmospheric CO_2 (with concurrent precipitation of $CaCO_3$), resulting in $\delta^{13}C$ depletions of up to 30.8 ‰ from theoretical equilibrium values. Additionally, the ^{18}O depleted values of the Red Hills carbonates are best explained by fractionation during hydroxylation (Clark et al. 1992).

The isotopic values plotted in Figure 5.17 display carbonates of hyper-alkaline ultramafic systems worldwide. The carbonates in the top right of the graph are from Mg^{2+}-HCO_3^- waters (Barnes et al. 1967; Neil & Barnes 1971) and are likely to have formed in equilibrium conditions. The markedly depleted values in the bottom left corner are thought to have formed in disequilibrium conditions within Ca^{2+}-OH^- hyper-alkaline waters. The 'scums and

sludges' of Northern California and the 'modern crusts' of Semail, Oman, represent an equivalent precipitate to Carbonate 1 (small nodules) and the 'fossil crusts' of Oman are considered equivalent to Carbonate 2 of the Red Hills.

The younger carbonates (i.e. Carbonate 1) at site MHS form in association with microorganisms, traces of which are observed in Figure 5.15. These microorganisms are abundant in the reducing conditions of the spring, and possibly gain energy from the high concentrations of dissolved CH_4 in fluid, classing them as methanotrophs (organisms which metabolise CH_4 as their sole source of carbon and energy). Another possibility is that the microorganisms are methanogenic (organisms which gain metabolic energy from the conversion of CO_2 to CH_4). These methanogens utilise the H_2 dissolved in serpentininzed fluids to create methane. As the isotopic signature of CH_4 emitting from this hyper-alkaline spring is distinctly abiotic (Figure 5.8), it is unlikely any biotic organism presently releases CH_4, reinforcing the presence of CH_4 consuming microorganisms (i.e. methanotrophs). This would therefore have the impact of decreasing CH_4 emissions at site MHS. Previous studies have seen a diverse spread of both methanogenic and methanotrophic organisms within the hyper-alkaline waters of low temperature ultramafic systems, such as those in Marqarin, Jordan (Pedersen et al. 2004), The Cedars, California (Suzuki et al. 2013), and at San Elena, Cost Rica (Sanchez-Murillo et al. 2014).

6.3 Amorphous Material, Microbes and Implications for Gas Emissions

The presence of amorphous material, which predominantly precipitate near Mg^{2+}-HCO_3 surface flows, has not yet been studied in relation to ultramafic environments. The biogeochemical nature of these deposits has been analysed to gain insight into their role in rock-water-gas interactions.

Three different forms of amorphous precipitates are observed to form in the Mg^{2+}-HCO_3 surface waters of the Red Hills, observed in Figure 5.3 as: 1) white/beige soft material, 2) black brittle precipitate and 3) red material with an oil-like sheen. The white/beige material precipitates in downstream terraces as observed in Figure 5.3 A. This material is likely to be a form of magnesite ($MgCO_3$), similar to those observed in Sanchez-Murillo et al. (2014).

These precipitates, as with those at the hyper-alkaline spring, absorb atmospheric CO_2 during formation from the reaction:

$$2\ Mg_3Si_2O_5(OH)_4 + 3\ CO_2 \rightarrow Mg_3Si_4O_{10}(OH)_2 + 3\ MgCO_3 + H_2O \qquad \textbf{Eqn. 11}$$

Serpentinite — Talc — Magnesite

The magnetic and mineralogical properties of the black precipitate observed in Figure 5.3, image C, suggest the presence of magnetite (Fe_3O_4) and/or chromite ($FeCr_2O_4$), which are common trace minerals in ultramafic environments. Both minerals display magnetic properties (although chromite is notably weaker), and are known catalysts to the H_2 producing serpentinization reactions (Neubeck et al. 2011; Mayhew et al. 2013).

The high concentration of chromium oxide (Cr_2O_3) in this precipitate, as observed in Table 5-8, is likely due to the breakdown of chromite spinels within the harzburgite protolith (Figure 5.11 E and F). These spinel grains show varying degrees of weathering/alteration in the unserpentinized harzburgite, but are for the most part quite resistant as observed in the elemental (SEM) maps of Appendix 4. It is likely that the Cr in this black magnetic precipitate is present in the less soluble and non-toxic trivalent form of Cr^{3+}. Although the precipitate is an amorphous deposit, it has not travelled far from source, as observed seeping from the soil horizons of eroded creek beds. The more soluble hexavalent Cr^{6+}, which is highly carcinogenic, is very likely the detectable Cr in surface waters ([Cr] ~ 0.0005 mg/L) and tarn waters ([Cr] ~ 0.002 mg/L) of the Red Hills. This has important biologic/ecologic implications for ultramafic waters, as the chemically mobile and bioavailable Cr^{6+} has the potential to induce toxic effects over a wide range of pH. The processes affecting oxidation from the relatively benign Cr^{3+} to the highly toxic Cr^{6+} in ultramafic environments is analysed in more detail in other studies (Oze 2003; Garnier et al. 2006; Garnier et al. 2013).

Active microorganisms habituate within this black brittle precipitate, as observed in Figure 5.18. Bacteria are also identified in the red amorphous material (Figure 5.19), which as suggested by data in Table 5-8 is a Cr-bearing iron oxide. These organisms are likely to survive on energy released during oxidation reactions, which occur during the precipitation of ionic metals in these environments. The shiny surface layers present on the red amorphous material are likely to be a result of lipids released by bacteria living within the substance. The biotic activity within the amorphous precipitates of Mg^{2+}-HCO_3 waters and those within the

carbonates of Ca^{2+}-OH^- waters provide insight into mechanisms of microbial survival in extreme environments. This microbial activity may provide insight to organisms thriving in similar conditions at depth within the lithosphere, as suggested by Proskurowski (2010).

The reactions directly or indirectly related to serpentinization in the Red Hills offer interesting implications regarding greenhouse gas sequestration. As observed in Eqn. 11, the formation of magnesite in Mg^{2+}-HCO_3 waters involves absorption of carbon dioxide. Also, CO_2 is absorbed during the precipitation of calcium carbonate in the Ca^{2+}-OH^- of site MHS as displayed by Eqn. 11. Finally, it is plausible that at least some of the CH_4 emissions at site MHS are absorbed by methanotrophic microbes thriving in the hyper-alkaline, H_2 and CH_4 rich conditions. These absorption mechanisms functioning effectively in nature offer useful and potentially innovative solutions toward minimising greenhouse gas emissions on Earth. This is especially applicable to industrial emissions, including the possibility of CO_2 sequestration at low temperatures.

Emissions of CH_4 in the Red Hills may provide insight to mechanisms of hydrocarbon formation in early Earth conditions, where geologic CH_4 production and accumulation was thought to play a key role in the evolution of Earth's atmosphere. These early emissions also played a key role in the development of primary proteins required as an energy source to the first methanogenic bacteria. In this sense, the biological processes occurring at surface conditions in the Red Hills may represent an analogous environment for potential life on other planets, such as Mars. The abiotic origin of CH_4 from terrestrial ophiolites such as the DMOB may also be representative of a similar source on Mars (Etiope et al. 2012; Etiope et al. 2011; Schoell & Etiope 2011).

7 Conclusions

Serpentinization and CH_4 production occurs at depth within the relatively unaltered chromite-bearing harzburgite of the Red Hills. Methane emissions from a hyper-alkaline (pH >11.6) and reduced (-243.4 mV) spring of calcium hydroxide (Ca^{2+}-OH^-) type waters near the Maitlands Fault were measured at 17,000 mg $m^{-2}day^{-1}$during summer and 730 mg $m^{-2}day^{-1}$ during winter. Variation in flux could be attributed to either climatic affects on soil permeability (i.e. permafrost conditions during winter) or simply sampling during quiescent periods of flux. The $\delta^{13}C$ and δD values of CH_4 emitting from this spring are consistent with CH_4 of abiotic origin (-32.7 ‰ VPDB, δD and -363 ‰ V-SMOW respectively). Hyper-alkaline fluids emitting from the spring are concentrated in dissolved CH_4 (2.2 mg/L) and H_2 (0.7 mg/L) and display $\delta^{13}C_{CH4}$ signatures consistent with other sites worldwide. Emissions of CH_4 above background were exclusive to Ca^{2+}-OH^- waters, in line with results of other recent studies (Etiope et al. 2013a, Etiope et al. 2013b).

The concentration of Ca^{2+} within hyperalkaline fluids is likely to have occurred during deep infiltration within the subsurface harzburgite in a system limited to CO_2 inputs (i.e. atmosphere). Upon resurfacing, atmospheric CO_2 becomes readily available and rapid reaction kinetics occur within the fluids. This results in the extensive precipitation of calcium carbonates, of which there are two distinguished types; fresh small nodules and older porous deposits. Isotopic evaluation of the smaller nodules shows evidence of extreme kinetic fractionation, with ^{13}C and ^{18}O depletions of up to 30.8 ‰ and 9.3 ‰ from equilibrium values. Older porous deposits display values indicative of a system closer to equilibrium. These porous, older carbonates (located on the outer edges of the hyper-alkaline spring) are possibly formed during interaction with between Mg^{2+}-HCO_3 and Ca^{2+}-OH^- hyper-alkaline waters. The disequilibrium between the mineralogy and interacting fluids and gases represent a potential habitable environment for microorganisms as well as offering potential insight towards low temperature CO_2 sequestration. Microorganisms form in association with the fresh small calcium carbonate nodules at site MHS. These microorganisms possibly gain energy from the high concentrations of dissolved CH_4 and H_2 in fluid. Additionally, various forms of Fe-rich amorphous material precipitate in association with Mg^{2+}-HCO_3 type waters at the Red Hills. The identification of bacteria and diatoms within this material offers

supporting information regarding microbial survival in metal-rich, reduced environments. This study demonstrates the importance of synthesizing theoretical, experimental, and field evidence in developing a greater comprehension for the complex nature of serpentinization in natural low temperature terrestrial environments.

Table 7-1 : Research questions and results

Research Question	Research Answer

Is there CH_4 and H_2 formation related to serpentinizaton in the Red Hills? If so, how much and what is its origin?	• Methane of abiotic origin seeps at a maximum of 17031.3 mg m^{-2} day^{-1} from site MHS in the Red Hills.
	  • Summer flux: 17031.3 mg m^{-2} day^{-1}
	  • Winter flux: 734 mg m^{-2} day^{-1}
	• Hyper-alkaline waters are concentrated in dissolved CH_4 and H_2, measuring 2.2 and 0.7 mg/L, respectively.

What are the potential mineralogical and structural controls on CH_4 release?	• Transects across fault lines showed no direct gas pathway was provided by these structures. • Alternatively faults may act more as mixing zone for deep fluids and old carbon during the formation of CH_4. • Gas permeable pathways are likely to exist in more localised zones (rather than linearly along the fault) as a result of faulting/shearing. • Chromite is present within the harzburgite substrate, which may act to catalyse CH_4 production.
How is serpentinization reflected in the geochemical character of the fluids at the Red Hills?	• Waters were categorised into two types; $Mg^{2+}HCO_3^-$ and Ca^{2+}-OH^- waters. The former occur in surface waters from the breakdown of harzburgite. The latter form from deep and prolonged interactions with harzburgite in a system with atmospheric CO_2 interaction. • Methane emissions only occur at Ca^{2+}-OH^- type waters and close to faulted/sheared areas. • The Ca^{2+}-OH^- waters are hyper-alkaline and reducing, with a pH of 11.6 and an Eh of -0.25 V. • Methane bearing waters seep from a localised area, isolated from magnesium-rich surface flows.
What are the temporal effects of gas flux and fluid movement? Is there seasonal variation?	• Seasonal variation exists with both gas and water character in the Red Hills. • Surface seepage may be affected by permafrost conditions during winter. • Precipitation varied largely between seasons, potentially affecting surface seepage by limiting hydraulic head in winter.
What is the nature of biologic and geologic precipitates?	• Three types of amorphous material are observed seeping actively from soil horizons near river edges in summer, and are less active in winter. Deposit types are red, black and beige in physical appearance. • XRF and other analyses determine the composition of amorphous material to be: Red material - iron oxide; black

	brittle material - chromium rich magnetite; beige soft amorphous material - most likely magnesite • Precipitates at site MHS are mostly calcium carbonates, with some layers in older deposits of forsterite-like silicates. • Biologic activity is present in all above deposits, as observed using SEM imaging and biologic culturing techniques. • The sequencing of bacteria within amorphous material determines different species present.
How does the flux and signature of gases in the Red Hills compare with previously investigated terrestrial ophiolite outcrops?	• The maximum flux (during summer) is comparable to those of other ophiolites (e.g. Chimaera, Turkey and Othrys, Greece), although few others have studied hydrocarbon flux specifically. Other characteristics of serpentinization such as the carbonate precipitation and hyper-alkaline fluids are very similar to those of The Cedars, California and of Santa Elena, Costa Rica. • Isotopic signatures are slightly more negative than international studies, and are almost identical to that of Poison Bay, Fiordland (NZ).
Is the vegetation in the Red Hills predominantly C_3 or C_4 type plants? Does this impact the isotopic signature of gases emitted?	• Species are indisputably of C_3 origin, and are unlikely to affect the isotopic signature of emitted gases at the Red Hills.

8 References

Abrajano, T. A., Murowchick, J. B., & Muehlenbachs, K. (1989). Serpentinization of the Acoje massif , Zambales ophiolite , Philippines : hydrogen and oxygen isotope geochemistry. *Tectonophysics*, *168*, 101–107.

Barnes, I., LaMarche Jr., V. C., & Himmelberg, G. (1967). Geochemical Evidence of Present-Day Serpentinization. *Science*, *156*(3776), 830–832.

Barnes, I., O'Neil, J., & Trescases, J. (1978). Present day serpentinization in New Caledonia, Oman and Yugoslavia. *Geochimica et Cosmochimica Acta*.

Bartholomew, J. W., & Mittwer, T. (1952). The gram stain. *Bacteriological Reviews*, *16*(1), 1.

Beeskow, B., Treloar, P. J., Rankin, A. H., Vennemann, T. W., & Spangenberg, J. (2006). A reassessment of models for hydrocarbon generation in the Khibiny nepheline syenite complex, Kola Peninsula, Russia. *Lithos*, *91*(1), 1–18.

Boschetti, T., Etiope, G., & Toscani, L. (2013). Abiotic Methane in the Hyperalkaline Springs of Genova, Italy. *Procedia Earth and Planetary Science*, *7*, 248–251.

Boschetti, T., & Toscani, L. (2008). Springs and streams of the Taro–Ceno Valleys (Northern Apennine, Italy): Reaction path modeling of waters interacting with serpentinized ultramafic rocks. *Chemical Geology*, *257*(1-2), 76–91.

Bottinga, Y. (1966). Calculation of Fractionation Factors for Carbon and Oxygen Isotopic Exchange in the System Calcite-Carbon Dioxide-Water. *The Journal of Physical Chemistry*, *287*(1).

Bottinga, Y. (1969). Calculated fractionation factors for carbon and hydrogen isotope exchange in the system. *Geochimics et Cosmochimica*, *33*, 49–64.

Bruni, J., Canepa, M., Chiodini, G., Cioni, R., Cipolli, F., Longinelli, A., … Vetuschi, M. (2002). Irreversible water – rock mass transfer accompanying the generation of the neutral, Mg – HCO 3 and high-pH, Ca – OH spring waters of the Genova province , Italy. *Applied Geochemistry*, *17*, 455–474.

Cardace, D., & Hoehler, T. M. (2014). Serpentinizing Fluids Craft Microbial Habitat Dawn. *Northeastern Naturalist*, *16*(5), 272–284.

Castaldi, S., & Tedesco, D. (2005). Methane production and consumption in an active volcanic environment of Southern Italy. *Chemosphere*, *58*, 131–139.

Charlou, J. L., Donval, J. P., Fouquet, Y., Jean-baptiste, P., & Holm, N. (2002). Geochemistry of high H 2 and CH 4 vent fluids issuing from ultramafic rocks at the Rainbow hydrothermal field (36° 14'N, MAR). *Chemical Geology*, *191*, 345–359.

Chiodini, G., Vesuviano, O., Manzoni, V. A., Cioni, R., Guidi, M., Raco, B., … Europa, C. (1998). Soil CO2 Fux Measurements in Volcanic and Geothermal Areas. *Applied Geochemistry*, *13*(5), 543–552.

Christensen, N. I. (1984). Structure and origin of the Dun Mountain ultramafic massif, New Zealand. *Geological Society of America Bulletin*, *95*(5), 551.

Cipolli, F., Gambardella, B., Marini, L., Ottonello, G., & Vetuschi Zuccolini, M. (2004). Geochemistry of high-pH waters from serpentinites of the Gruppo di Voltri (Genova, Italy) and reaction path modeling of CO2 sequestration in serpentinite aquifers. *Applied Geochemistry*, *19*(5), 787–802.

Clark, I. D., Fontes, J.-C., & Fritz, P. (1992). Stable isotope disequilibria in travertine from high pH waters: Laboratory investigations and field observations from Oman. *Geochimica et Cosmochimica Acta*, *56*(5), 2041–2050.

Cody, G. D., Boctor, N. Z., Filley, T. R., Hazen, R. M., Scott, J. H., Sharma, A., & Yoder, H. S. (2000). Primordial carbonylated iron-sulfur compounds and the synthesis of pyruvate. *Science*, *289*(5483), 1337–1340.

Conrad, M. E., Mayhew, L. E., Christensen, J. N., Bill, M., & Templeton, A. S. (2013). Isotopic signatures of H2 and CH4 at the Cedars : Implications for temperatures and mechanisms of serpentinization at the site. *Goldschmidt Abstracts*, (1988), 2014.

Davis, T. E., Johnston, M. R., Rankin, P. C., & Stull, R. J. (1979). The Dun Mountain ophiolite belt in East Nelson, New Zealand. In *Ophiolites. Proceedings of the International Ophiolite Symposium, Cyprus* (pp. 480–496).

Etiope, G. (1997). Evaluation of a micro gas chromatographic technique for environmental analyses of CO2 and C1–C6 alkanes. *Journal of Chromatography A*, *775*(1-2), 243–249.

Etiope, G. (2012). Methane uncovered. *Nature Geoscience*, *5*(June), 373–374.

Etiope, G., Ehlmann, B., & Schoell, M. (2012). Low temperature production and exhalation of methane from serpentinized rocks on Earth : A potential analog for methane production on Mars. *Icarus*, *224*, 276–285.

Etiope, G., Fridriksson, T., Italiano, F., Winiwarter, W., & Theloke, J. (2007). Natural emissions of methane from geothermal and volcanic sources in Europe. *Journal of Volcanology and Geothermal Research*, *165*(1-2), 76–86.

Etiope, G., & Ionescu, A. (2014). Low-temperature catalytic CO 2 hydrogenation with geological quantities of ruthenium: a possible abiotic CH 4 source in chromitite-rich serpentinized rocks. *Geofluids*, 1–15.

Etiope, G., Oehler, D. Z., & Allen, C. C. (2011). Methane emissions from Earth's degassing: Implications for Mars. *Planetary and Space Science*, *59*(2-3), 182–195.

Etiope, G., & Schoell, M. (2014). Abiotic Gas: Atypical, But Not Rare. *Elements*, *10*(4), 291–296.

Etiope, G., Schoell, M., & Hosgörmez, H. (2011). Abiotic methane flux from the Chimaera seep and Tekirova ophiolites (Turkey): Understanding gas exhalation from low temperature serpentinization and implications for Mars. *Earth and Planetary Science Letters*, *310*(1-2), 96–104.

Etiope, G., & Sherwood Lollar, B. (2013). Abiotic Methane On Earth. *Reviews of Geophysics*, *51*(2012), 276–299.

Etiope, G., Tsikouras, B., Kordella, S., Ifandi, E., Christodoulou, D., & Papatheodorou, G. (2013). Methane flux and origin in the Othrys ophiolite hyperalkaline springs, Greece. *Chemical Geology*, *347*, 161–174.

Etiope, G., Vance, S., Christensen, L. E., Marques, J. M., & Ribeiro, I. (2013). Methane in serpentinized ultramafic rocks in mainland Portugal. *Marine and Petroleum Geology*, *45*, 12–16.

Fritz, P., Clark, I. D., Fontes, J.-C., Whiticar, M. J., & Faber, E. (1992). Deuterium and 13C evidence for low temperature production of hydrogen and methane in a highly alkaline groundwater environment in Oman. *Water-Rock Interaction*, 793–796.

Frost, B. R., & Beard, J. S. (2007). On silica activity and serpentinization. *Journal of Petrology*, *48*, 1351–1368.

Frost, B. R., Evans, K. a., Swapp, S. M., Beard, J. S., & Mothersole, F. E. (2013). The process of serpentinization in dunite from New Caledonia. *Lithos*, *178*, 24–39.

Fruh-green, G. L., Connolly, J. A. D., Plas, A., Kelley, D. S., Grobety, B., & Früh-Green, G. L. (2004). Serpentinization of oceanic peridotites: Implications for geochemical cycles and biological activity. In *The Subseafloor Biosphere at Mid-Ocean Ridges* (Vol. 144, pp. 119–136).

Früh‐Green, G. L., Connolly, J. A. D., Plas, A., Kelley, D. S., & Grobety, B. (2004). Serpentinization of oceanic peridotites: implications for geochemical cycles and biological activity. *The Subseafloor Biosphere at Mid-Ocean Ridges*, 119–136.

Garnier, J., Quantin, C., Martins, E. S., & Becquer, T. (2006). Solid speciation and availability of chromium in ultramafic soils from Niquelandia , Brazil. *Journal of Geochemical Exploration*, *88*, 206–209.

Garnier, J., Quantin, C., Mendes, E., Vantelon, D., Montargès-pelletier, E., & Becquer, T. (2013). Geoderma Cr (VI) genesis and dynamics in Ferralsols developed from ultramafic rocks : The case of Niquelândia , Brazil. *Geoderma*, *193-194*, 256–264.

Giggenbach, W. F. (1997). Relative importance of thermodynamic and kinetic processes in governing the chemical and isotopic composition of carbon gases in high-heatflow sedimentary basins. *Geochimica et Cosmochimica Acta*, *61*(17), 3763–3785.

Giggenbach, W. F., & Lyon, G. L. (1990). *Composition and origin of the hydrogen-rich gas seep, Poison Bay, and of two other natural gases from Fiordland, New Zealand*. Nuclear Sciences Group, DSIR Physical Sciences.

Holm, N. G., & Charlou, J. L. (2001). Initial indications of abiotic formation of hydrocarbons in the Rainbow ultramafic hydrothermal system, Mid-Atlantic Ridge. *Earth and Planetary Science Letters*, *191*(191), 1–8.

Holm, N. G., & Neubeck, A. (2009). Reduction of nitrogen compounds in oceanic basement and its implications for HCN formation and abiotic organic synthesis. *Geochemical Transactions*, *10*, 9.

Holm, N., Mousis, O., Oze, C., Waite, H., & Guilbert-Leputre, A. (2014). *Serpentinization on celestial bodies (plnaets, moons, comets)*.

Horibe, Y., & Craig, H. (1995). D/H fractionation in the system methane-hydrogen-water. *Geochimica et Cosmochimica Acta*, *59*(24), 5209–5217.

Huber, C., & Wächtershäuser, G. (1997). Activated acetic acid by carbon fixation on (Fe,Ni)S under primordial conditions. *Science (New York, N.Y.)*, *276*(5310), 245–7.

Hunter, H. W. (1977). Geology of the Cobb Intrusives, Takaka Valley, North-West Nelson, New Zealand. *New Zealand Journal of Geology and Geophysics*, *20*(3), 469–501.

Hyndman, R. D., & Peacock, S. M. (2003). Serpentinization of the forearc mantle. *Earth and Planetary Science Letters*.

Jacquemin, M., Beuls, A., & Ruiz, P. (2010). Catalytic production of methane from CO2 and H2 at low temperature: Insight on the reaction mechanism. *Catalysis Today*, *157*(1-4), 462–466.

Johnston, M. R. (1982). Sheet N28BD-Red Hills Geological Map of New Zealand 1: 50 000. Map (1 sheet) and notes. *Wellington. Department of Scientific and Industrial Research*.

Johnston, M. R. (1990). Geology of the St Arnaud District, Southeast Nelson (Sheet N29). In L. A. Reay, M B., Redmond (Ed.), . *Lower Hutt: New Zealand Geological Survey*.

Kelemen, P. B., Matter, J., Streit, E. E., Rudge, J. F., Curry, W. B., & Blusztajn, J. (2011). Rates and Mechanisms of Mineral Carbonation in Peridotite: Natural Processes and Recipes for Enhanced, in situ CO 2 Capture and Storage. *Annual Review of Earth and Planetary Sciences*, *39*(1), 545–576.

Kelley, D. S., & Frtih-green, G. L. (1999). Abiogenic methane in deep-seated mid-ocean ridge environments: Insights from stable isotope analyses. *Journal of Geophysical Research*, *104*(B5), 10,439–10460.

Kelley, D. S., Karson, J. A., Früh-Green, G. L., Yoerger, D. R., Shank, T. M., Butterfield, D. A., … Proskurowski, G. (2005). A serpentinite-hosted ecosystem: the Lost City hydrothermal field. *Science*, *307*(5714), 1428–1434.

Klein, F., Bach, W., & McCollom, T. M. (2013). Compositional controls on hydrogen generation during serpentinization of ultramafic rocks. *Lithos*, *178*, 55–69.

Lauder, W. R. (1965). The geology of Dun Mountain, Nelson, New Zealand. *New Zealand Journal of Geology and Geophysics*, *8*(3), 475–504.

Lee, J., Brooks, R. R., Reeves, R. D., & Boswell, C. R. (1975). Soil Factors Controlling a New Zealand Serpentine Flora. *Plant and Soil*, *42*, 153–160.

Lee, W. G., & Hewitt, A. E. (1982). Soil changes associated with development of vegetation on an ultramafic scree, northwest Otago, New Zealand. *Journal of the Royal Society of New Zealand*, *12*(3), 229–241.

Lewicki, J. L., Bergfeld, D., Cardellini, C., Chiodini, G., Granieri, D., Varley, N., & Werner, C. (2005). Comparative soil CO2 flux measurements and geostatistical estimation methods on Masaya volcano, Nicaragua. *Bulletin of Volcanology*, *68*(1), 76–90.

Livingston, G. P., & Hutchinson, G. L. (1995). Enclosure-based measurement of trace gas exchange : applications and sources of error. *Biogenic Trace Gases: Measuring Emissions from Soil and Water*, 14–50.

Malahoff, A. (1965). Gravimetric and Geologic Studies of an Ultramafic Mass in New Zealand. *Americal Geophysical Union Transactions*, *46*, 159–160.

Marques, J. M., Carreira, P. M., Carvalho, M. R., Matias, M. J., Goff, F. E., Basto, M. J., … Rocha, L. (2008). Origins of high pH mineral waters from ultramafic rocks, Central Portugal. *Applied Geochemistry*, *23*(12), 3278–3289.

Mayhew, L. E., Ellison, E. T., McCollom, T. M., Trainor, T. P., & Templeton, a. S. (2013). Hydrogen generation from low-temperature water–rock reactions. *Nature Geoscience*, *6*, 478–484.

McCollom, T. M. (2013). Laboratory Simulations of Abiotic Hydrocarbon Formation in Earth's Deep Subsurface. *Reviews in Mineralogy and Geochemistry*, *75*(1), 467–494.

McCollom, T. M., & Bach, W. (2009). Thermodynamic constraints on hydrogen generation during serpentinization of ultramafic rocks. *Geochimica et Cosmochimica Acta*.

Mccollom, T., & Seewald, J. (2006). Carbon isotope composition of organic compounds produced by abiotic synthesis under hydrothermal conditions. *Earth and Planetary Science Letters*, *243*(1-2), 74–84.

Meder, R., Hunter, K. a., & Peake, B. M. (1991). Trans-Tasman tropospheric transport of acid rain. *Journal of the Royal Society of New Zealand*, *21*(2), 137–142.

Morrill, P. L., Kuenen, J. G., Johnson, O. J., Suzuki, S., Rietze, A., Sessions, A. L., … Nealson, K. H. (2013). Geochemistry and geobiology of a present-day serpentinization site in California: The Cedars. *Geochimica et Cosmochimica Acta*, *109*, 222–240.

Neil, J. R. O., & Barnes, I. (1971). C13 and 018 compositions in some fresh-water carbonates associated with ultramafic rocks and serpentinites : western United States *. *Geoclrimica et Cosmochimica Act*, *35*, 687–697.

Neubeck, A., Duc, N. T., Bastviken, D., Crill, P., & Holm, N. G. (2011). Formation of H 2 and CH 4 by weathering of olivine at temperatures between 30 and 70 ° C. *Geochemical Transactions*, *12*(6), 1–10.

Neubeck, A., Thanh, N. ., Hellevang, H., Oze, C., Bastviken, D., & Bacsik, Z. (2014). Olivine alteration and H2 production in carbonate-rich, low temperature aqueous environments. *Planetary and Space Science*, *96*, 51–61.

Nyyssönen, M., Hultman, J., Ahonen, L., Kukkonen, I., Paulin, L., Laine, P., … Auvinen, P. (2014). Taxonomically and functionally diverse microbial communities in deep crystalline rocks of the Fennoscandian shield. *The ISME Journal*, *8*(1), 126–38.

Oze, C. (2003). *Chromium Geochemistry Of Serpentinites And Serpentine Soils*. Doctoral dissertaion, Stanford University.

Oze, C., Fendorf, S., Bird, D. K., & Coleman, R. G. (2004). Rocks And Serpentine Soils From The Franciscan Complex Of California, *304*, 67–101.

Oze, C., Jones, L. C., Goldsmith, J. I., & Rosenbauer, R. J. (2012). Differentiating biotic from abiotic methane genesis in hydrothermally active planetary surfaces. *Proceedings of the National Academy of Sciences*.

Oze, C., & Sharma, M. (2005). Have olivine, will gas: Serpentinization and the abiogenic production of methane on Mars. *Geophysical Research Letters*, *32*(10), L10203.

Oze, C., & Sharma, M. (2007). Serpentinization and the inorganic synthesis of H2 in planetary surfaces. *Icarus*, *186*(2), 557–561.

Parkin, T., Mosier, A., Smith, J., Venterea, R., Johnson, J., Reicosky, D., … Venterea, R. (2003). USDA-ARS GRACEnet chamber-based trace gas flux measurement protocol. *USDA-ARS, Washington DC*, 1–28.

Pedersen, K., Nilsson, E., Arlinger, J., Hallbeck, L., & O'Neill, A. (2004). Distribution, diversity and activity of microorganisms in the hyper-alkaline spring waters of Maqarin in Jordan. *Extremophiles : Life under Extreme Conditions*, *8*(2), 151–64.

Proskurowski, G. (2010). Handbook of Hydrocarbon and Lipid Microbiology.

Proskurowski, G., Lilley, M. D., Kelley, D. S., & Olson, E. J. (2006). Low temperature volatile production at the Lost City Hydrothermal Field, evidence from a hydrogen stable isotope geothermometer. *Chemical Geology*, *229*(4), 331–343.

Robinson, B. H., Brooks, R. R., Kirkman, J. H., Gregg, P. E. H., & Gremigni, P. (1996). Plant-available elements in soils and their influence on the vegetation over ultramafic ("serpentine") rocks in New Zealand. *Journal of the Royal Society of New Zealand*, *26*(4), 457–468.

Sachan, H. K., Mukherjee, B. K., & Bodnar, R. J. (2007). Preservation of methane generated during serpentinization of upper mantle rocks: Evidence from fluid inclusions in the

Nidar ophiolite, Indus Suture Zone, Ladakh (India). *Earth and Planetary Science Letters*, *257*(1-2), 47–59.

Sanchez-Murillo, R., Gazel, E., Schwarzenbach, E. M., Crespo-Medina, M., O. Schrenk, M., Boll, J., & Gill, B. C. (2014). Geochemical evidence for active tropical serpentinization in the Santa Elena Ophiolite, Costa Rica: An analog of a humid early Earth? *Geochemistry, Geophysics, Geosystems*, 1783–1800.

Schoell, M., & Etiope, G. (2011). Ophiolites as Source of Abiotic Methance on Earth: Analogue Mission Potential Sites for Methane Flux Measurements on Mars. *LPI Contributions*, *1612*, 1–4.

Schulte, M., Blake, D., Hoehler, T., & Mccollom, T. (2006). Serpentinization and Its Implications for Life on the Early Earth and Mars. *ASTROBIOLOGY*, *6*(2), 364–376.

Schwarzenbach, E. M., Früh-Green, G. L., Bernasconi, S. M., Alt, J. C., & Plas, A. (2013). Serpentinization and carbon sequestration: A study of two ancient peridotite-hosted hydrothermal systems. *Chemical Geology*, *351*, 115–133.

Sharp, Z. (2007). *Principles of stable isotope geochemistry*. Pearson education Upper Saddle River, NJ.

Shock, E. L. (1990). Geochemical Constraints On The Origin Of Organic Compounds In Hydrothermal Systems. *Origins of Life and Evolution of the Biosphere*, *20*, 331–367.

Sivell, W. J., & McCulloch, M. T. (2000). Reassessment of the origin of the Dun Mountain Ophiolite, New Zealand: Nd-isotopic and geochemical evolution of magma suites. *New Zealand Journal of Geology and Geophysics*, *43*(2), 133–146.

Stamatis, G., & Gartzos, E. (1999). The silica supersaturated waters of northern Evia and eastern central Greece Abstract : *Hydrological Processes*, *13*(April), 2833–2845.

Suda, K., Ueno, Y., Yoshizaki, M., Nakamura, H., Kurokawa, K., Nishiyama, E., … Maruyama, S. (2014). Origin of methane in serpentinite-hosted hydrothermal systems: The CH4–H2–H2O hydrogen isotope systematics of the Hakuba Happo hot spring. *Earth and Planetary Science Letters*, *386*, 112–125.

Suzuki, S., Wu, A., Cheung, A., Tenney, A., Wanger, G., & Kuenen, J. G. (2013). Microbial diversity in The Cedars, an ultrabasic, ultrareducing, and low salinity serpentinizing ecosystem. *PNAS*, *110*(38), 15336–15341.

Thampi, K. R., Kiwi, J., & Graetzel, M. (1987). Methanation and photo-methanation of carbon dioxide at room temperature and atmospheric pressure. *Nature*, *327*(6122), 506–508.

Walcott, R. I. (1968). Geology of the Red Hill Complex, Nelson, New Zealand. *Transactions of the Royal Society of New Zealand, Earth Sciences*, *7*(5), 57–88.

Wang, X., Ouyang, Z., Zhuo, S., Zhang, M., Zheng, G., & Wang, Y. (2014). Serpentinization, abiogenic organic compounds, and deep life. *Science China Earth Sciences*, *57*(5), 878–887.

Wellman, H. W. (1948). The Outline of the Geology of New Zealand. *New Zealand Geological Survey*, 47.

Whiticar, M. J. (1999). Carbon and hydrogen isotope systematics of bacterial formation and oxidation of methane. *Chemical Geology*, *161*(1-3), 291–314.

Wood, B. L. (1972). Metamorphosed ultramafites and associated formations near Milford Sound, New Zealand. *New Zealand Journal of Geology and Geophysics*, *15*(1), 88–128.

Wray, J. J., & Ehlmann, B. L. (2011). Geology of possible Martian methane source regions. *Planetary and Space Science*, *59*(2-3), 196–202.

Yuce, G., Italiano, F., D'Alessandro, W., Yalcin, T. H., Yasin, D. U., Gulbay, a. H., … Walia, V. (2014). Origin and interactions of fluids circulating over the Amik Basin (Hatay, Turkey) and relationships with the hydrologic, geologic and tectonic settings. *Chemical Geology*, *388*, 23–39.

9 Appendix

Table 9-1: Methods of methanogenesis.

Occurrence	Temperature	Mechanism of system	Principle reaction	Example	Reference
Magmatic / Hydrothermal	500-1500 ºC	1. High temperature mantle hydrolysis / hydrogenation of metal carbides.	$Al_4C_3 + 12H_2O = 3CH_4 + 4Al(OH)_3$ $Fe_3C + 4H^+ = 3Fe + CH_4$	Khibiny inclusions	(Beeskow et al. 2006)
	500-1500 ºC	2. High temperature mantle reduction of carbon species with H_2O	$8FeO + CaCO_3 + 2H_2O = 4Fe_2O_3 + CH_4 + CaO$	East Pacific Rise	(Holm & Neubeck 2009)
	<500-600 ºC	3. Evolution of CO_2 to CH_4 during cooling of magma	$CO_2 + 2H_2O = CH_4 + 2O_2$	New Zealand, Gulf of Thailand, SW Indian Ridge gabbro inclusions, South West Indian Ridge Gabbros	(Giggenbach 1997; Kelley & Frtih-green 1999)
	~200 ºC	4. Oxidation of Iron in pyrrhotite to pyrite and magnetite Oxidation of fayalite to magnetite	$2\ FeS + 4/3\ H_20 = FeS_2 + 1/3\ Fe_30_4 + 4/3\ H_2$ $3\ Fe_2SiO_4 + 2\ H_20 = 2\ Fe_3Q + 3\ SiO_2 + 2\ H_2$ (may be followed by rxn 9 to form CH_4)	Basalt hosted submarine hydrothermal systems	(Shock 1990)
	400-500ºC	5. High temperature post magmatic reactions	$8FeO + 2H_2O + CO_2 = 4Fe_2O_3 + CH_4$	Geothermal systems in Japan, New Zealand	(Castaldi & Tedesco 2005)
Gas – water – rock interactions	<400 ºC	6. Graphite reduction with H_2O	$Mg_3Si_4O_{10}(OH)_2 + 3CaCO_3 + 6C + 5H_2O = 3CaMg(CO_3)_2 + 4SiO_2 + 3CH_4$	Meteorites	(McCollom 2013)
	300 ºC	7. Iron carbonate decomposition, siderite decomposition with H_2O	$3FeCO_3 + wH_2O = Fe_3O_4 + xCO_2 + yCO + zH_2 + HCs$ (may be followed by rxn 9 to form CH_4)	Meteorites	(McCollom 2013)
Serpentinization	250-870 ºC	8. Direct reduction (without CO_2) to CH_4. Carbonate methanation.	$CaCO_3 + 4H_2 = CH_4 + Ca(OH)_2 + H_2O$ $MgCO_3 + 4H_2 = CH_4 + Ca(OH)_2 + H_2O$ $FeCO_3 + 5H_2 = CH_4 + FeO + 2H_2O$	Thermal decomposition of carbonates.	(Oze & Sharma 2005; Boschetti et al. 2013)

Serpentinization	25 – 500 ºC	9. Fischer Trope Type (FTT) reactions. Hydrogenation of CO_2 - catalysed by surface minerals: Gas phase Aqueous phase	One-step methanation (Sabatier) : $CO_2 + 4H_2 = CH_4 + 2H_2O$ Two-steps reverse water-gas shift and Fischer Trope: $CO_2 + H_2 = CO + H_2O$ $CO + 3H_2 = CH_4 + H_2O$ In aqueous solution: $CO_3^{2-} + 4H_2 = CH_4 + H_2O + CO_3 + 2OH^-$	Mid ocean ridges, continental volcanoes serpentinized ultramafic rocks at sea floor and ophiolites, alkaline igneous intrusions.	(McCollom 2013; Etiope & Lollar 2013)
		10. Serpentinization of Olivine Forsterite Fayalite	 $Mg_2SiO_4 + 3/2H_2O = 1/2Mg_3Si_2O_5(OH)_4 + 1/2Mg(OH)_2$ Forsterite Serpentinite Brucite $Fe_2SiO_4 + 2/3H_2O = 2/3Fe3O_4 + SiO_2 + 2/3H_2$ (may be followed by rxn 9 to form CH_4)	Ophiolites In New Zealand, Greece, Italy	(Oze & Sharma 2007) (Frost & Beard 2007)
		11.Olivine / pyroxene alteration into serpentine minerals such as serpentinite and brucite Reduced iron from above reaction oxidised to magnetite	$Fe_2SiO_4 + 5Mg_2SiO_4 + 9H_2O = 3Mg_3Si_2O_5(OH)_4 + Mg(OH)_2 + 2Fe(OH)_2$ Fayalite Forsterite Serpentinite Brucite Iron Hydroxide $3Fe(OH)_2 = Fe_3O_4 + 2H_2O + H_2$ (may be followed by rxn 9 to form CH_4)		(Schulte et al. 2006)
	25 - 300 ºC	12. Serpentinization and hydration of ultramafic minerals (fayalite) with aqueous CO_2 creating magnetite and CH_4	$6Fe_2SiO_4 + CO_2(aq) + 2H_2O = 6SiO_{2[Quartz]} + 4Fe_3O_4 + CH_4$ Or: $24(Mg, Fe)_2SiO_4 + 26H_2O + CO_2 \rightarrow 12(Mg,Fe)_3 Si_2O_5(OH)_4 + 4Fe_3O_4 + CH_4$		(Oze & Sharma 2005; Sachan et al. 2007; Etiope et al. 2013a; Suda et al. 2014)
		13. Ferrosilite (pyroxene) hydrolysis	$12FeSiO_3 + 2H_2O + CO_{2(aq)} = 4Fe_3O_4 + CH_4 + 12SiO_{2[Amorphous]}$	Peridotite hosted geothermal systems	(Charlou et al. 2002)
		14. Serpentinization of olivine to form molecular hydrogen (H_2); or Mg 50%, Fe 50%.	$3FeMgSiO_4 + 3H_2O = Mg_3Si_2O_5(OH)_4 + SiO_2 + Fe_3O_4 + H_2$ (may be followed by rxn 9 to form CH_4)		(Wang et al. 2014; Oze & Sharma 2007)

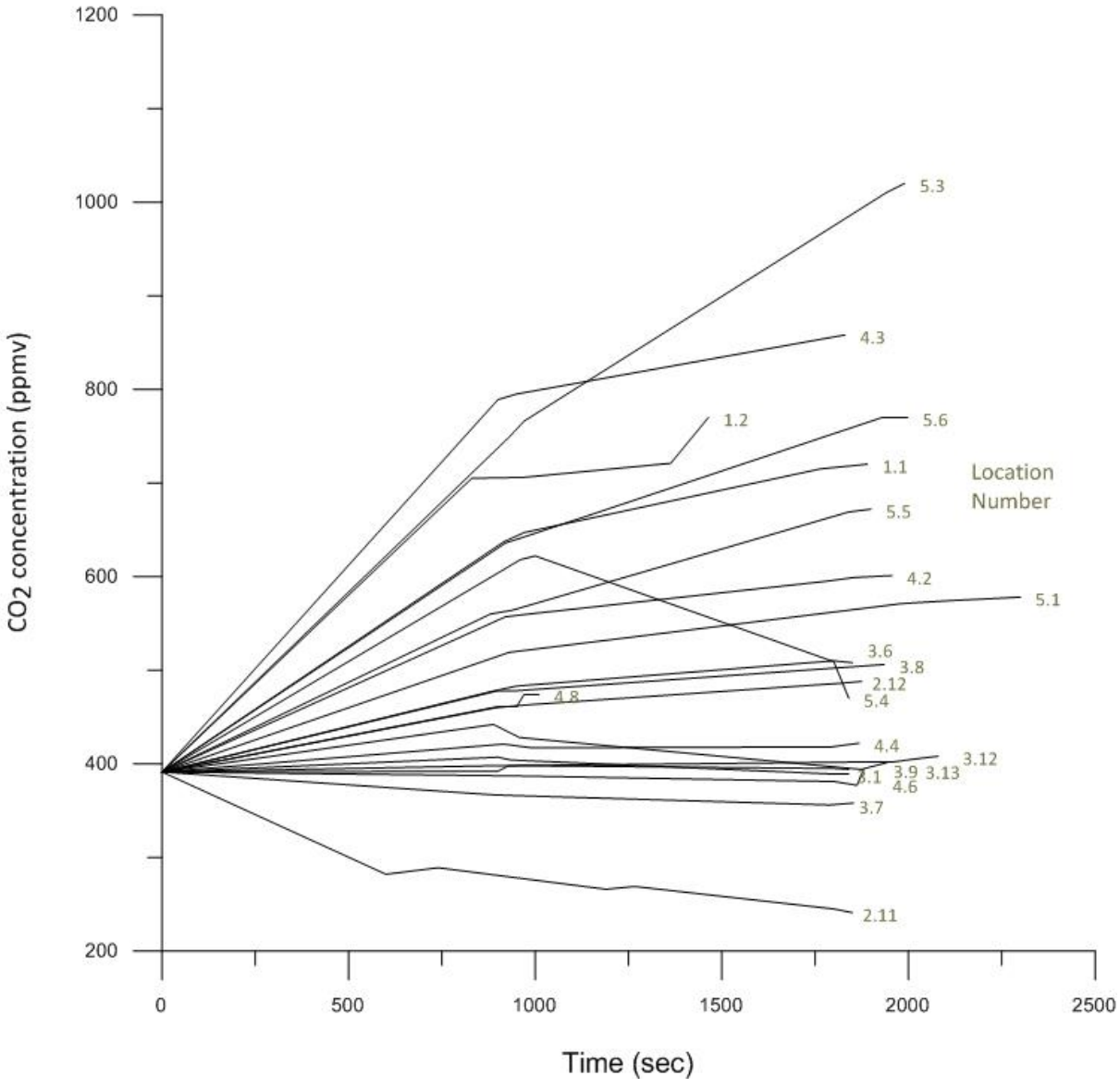

Appendix 1: Carbon dioxide flux from all measured locations in the Red Hills.

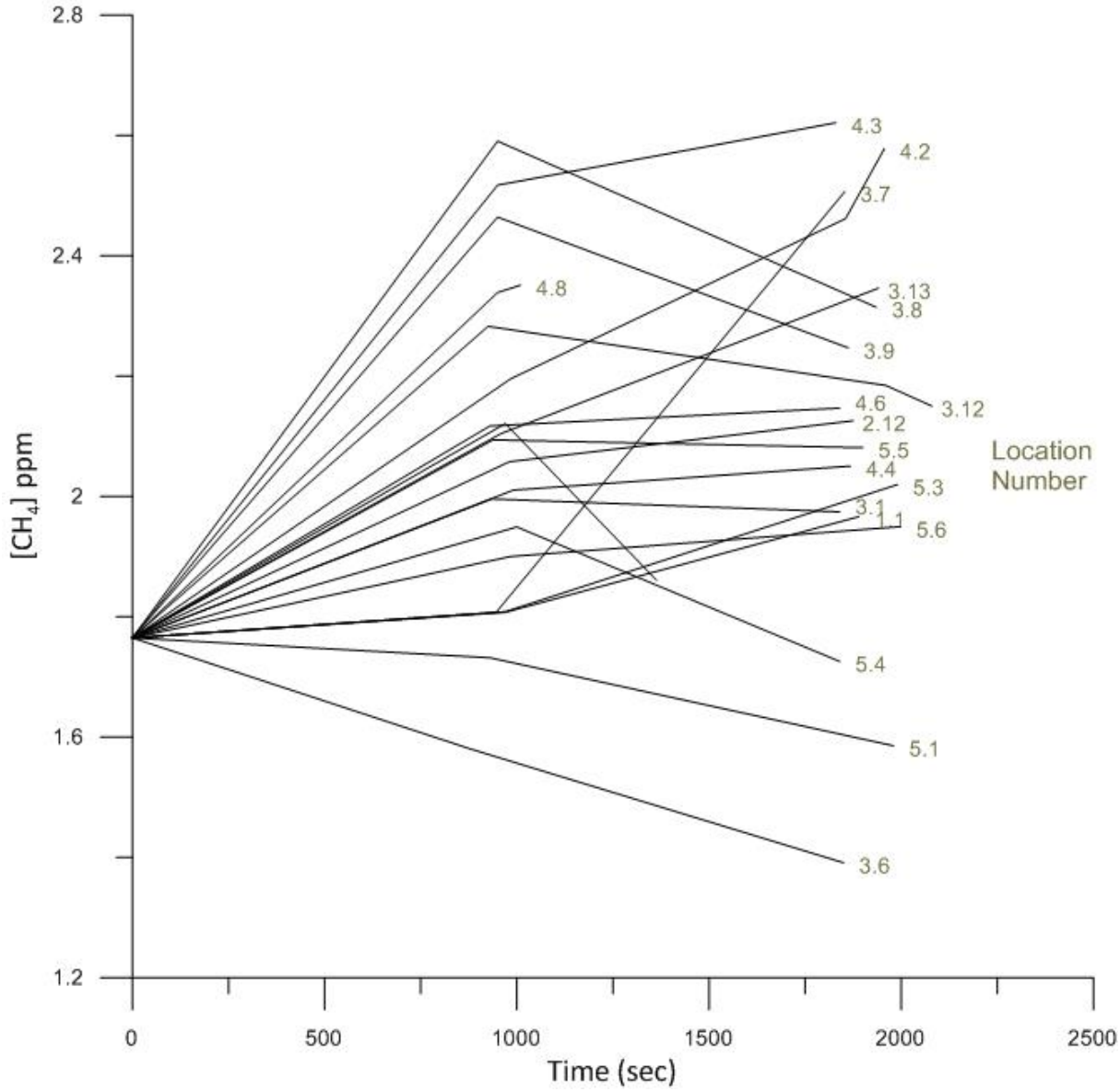

Appendix 2: Methane flux from all sample locations in the Red Hills.

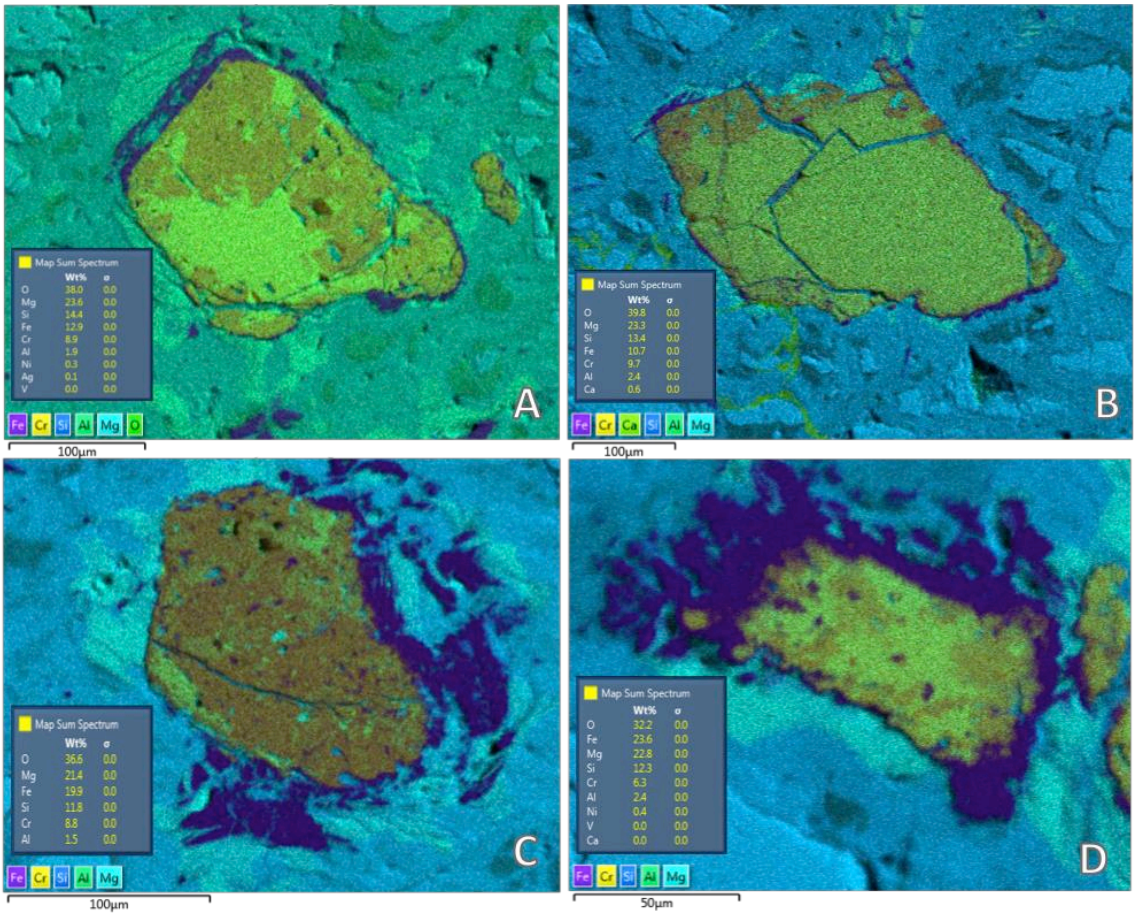

Appendix 3: Elemental mapping using SEM techniques of chromite grains and elemental abundances within the Red Hills harzburgite. Within a forsterite matrix, grains C and D are altered to a much higher degree, with concentrated iron bands surrounding the grain, representing 19.9 and 23.6 weight % of the mapped area respectively. Grains A and B display less iron alteration and represent a much fresher chromite crystal.

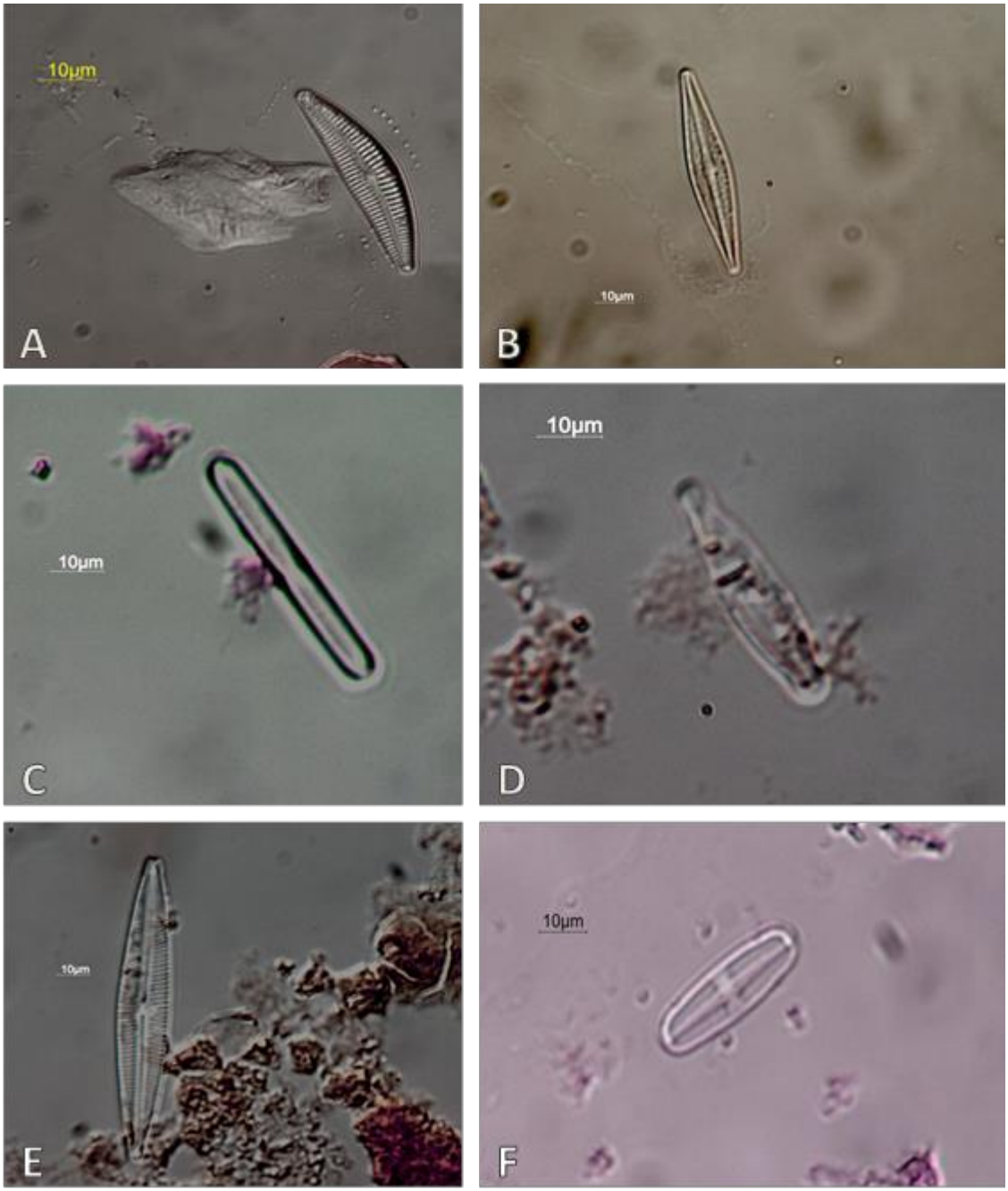

Appendix 4: Diatoms present within the red amorphous material observed in Figure 5.3B. Genus names are; A: *Amphora*, B: *Navicula cryptocephala*, C *Tryblionella* / *Fragilaria exigua*, D: *Navicula*, E: *Navicula cryptocephaloides*, *F:Achnanthes subatomoides*.

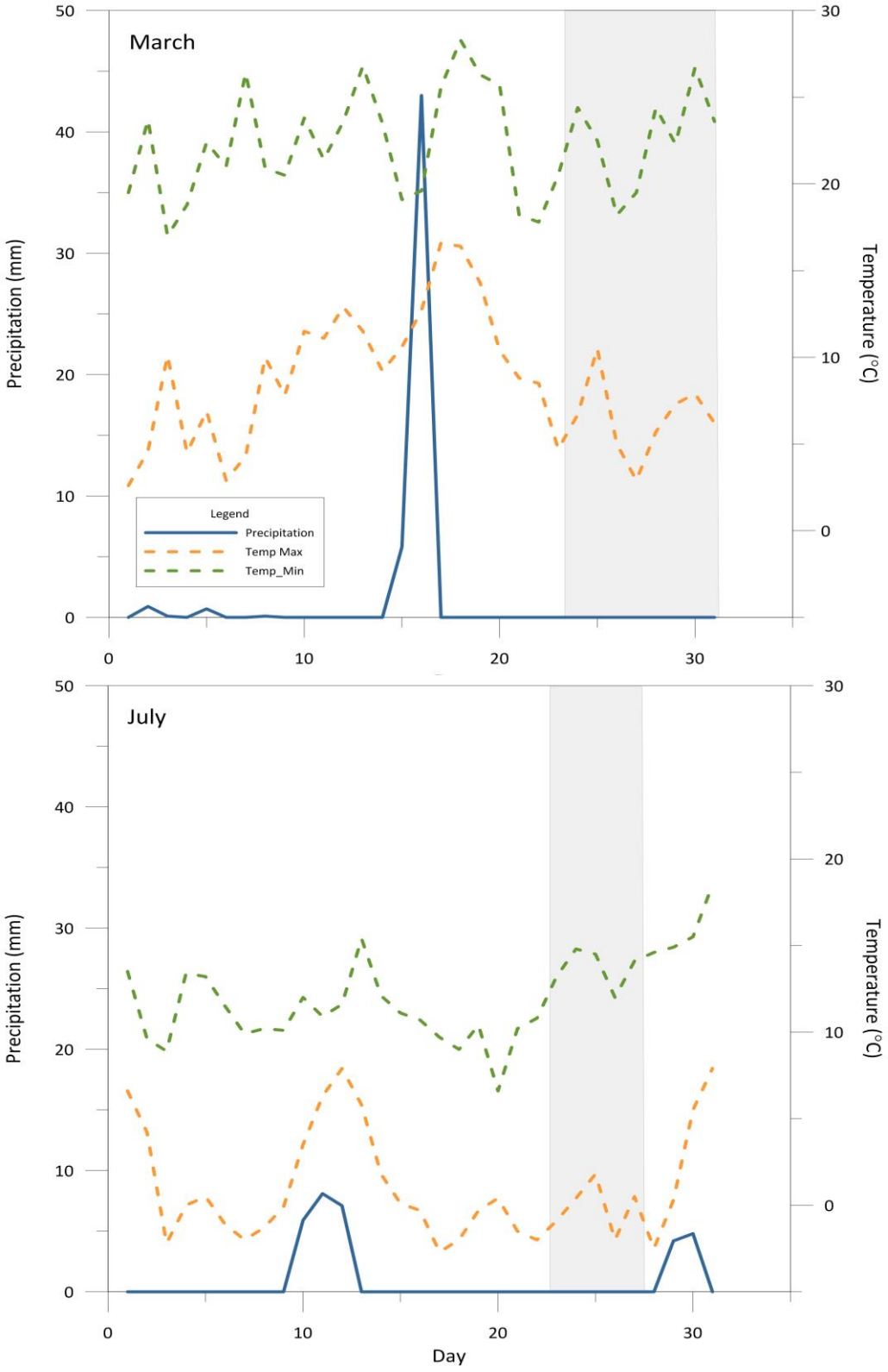

Appendix 5: Climate variables during summer (March) and winter (July) field sampling. Permafrost conditions during winter may affect surface seepage of CH_4 and hydrogen. The timing and duration of field sampling is highlighted in the grey area.

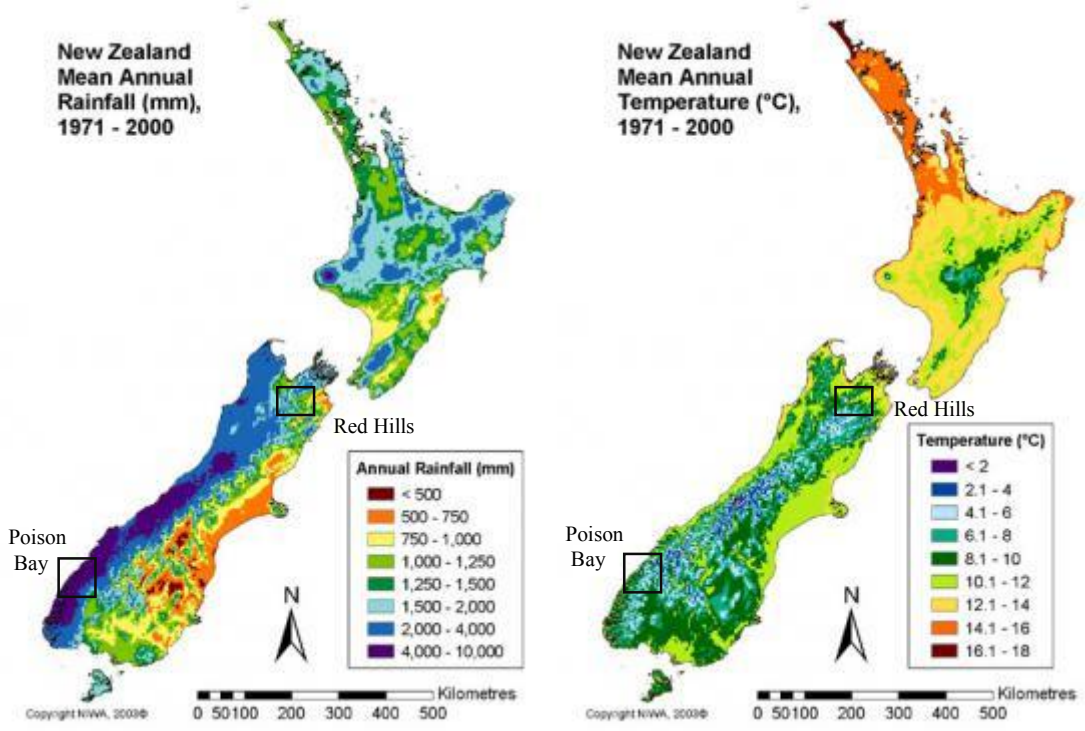

Appendix 6: Precipitation and temperature variation between the Red Hills (St Arnaud, Nelson Lakes) and Poison Bay (Fiordland). Difference in isotopic signature from CH_4 can be attributed to differences in climate and coastal proximity between sites.

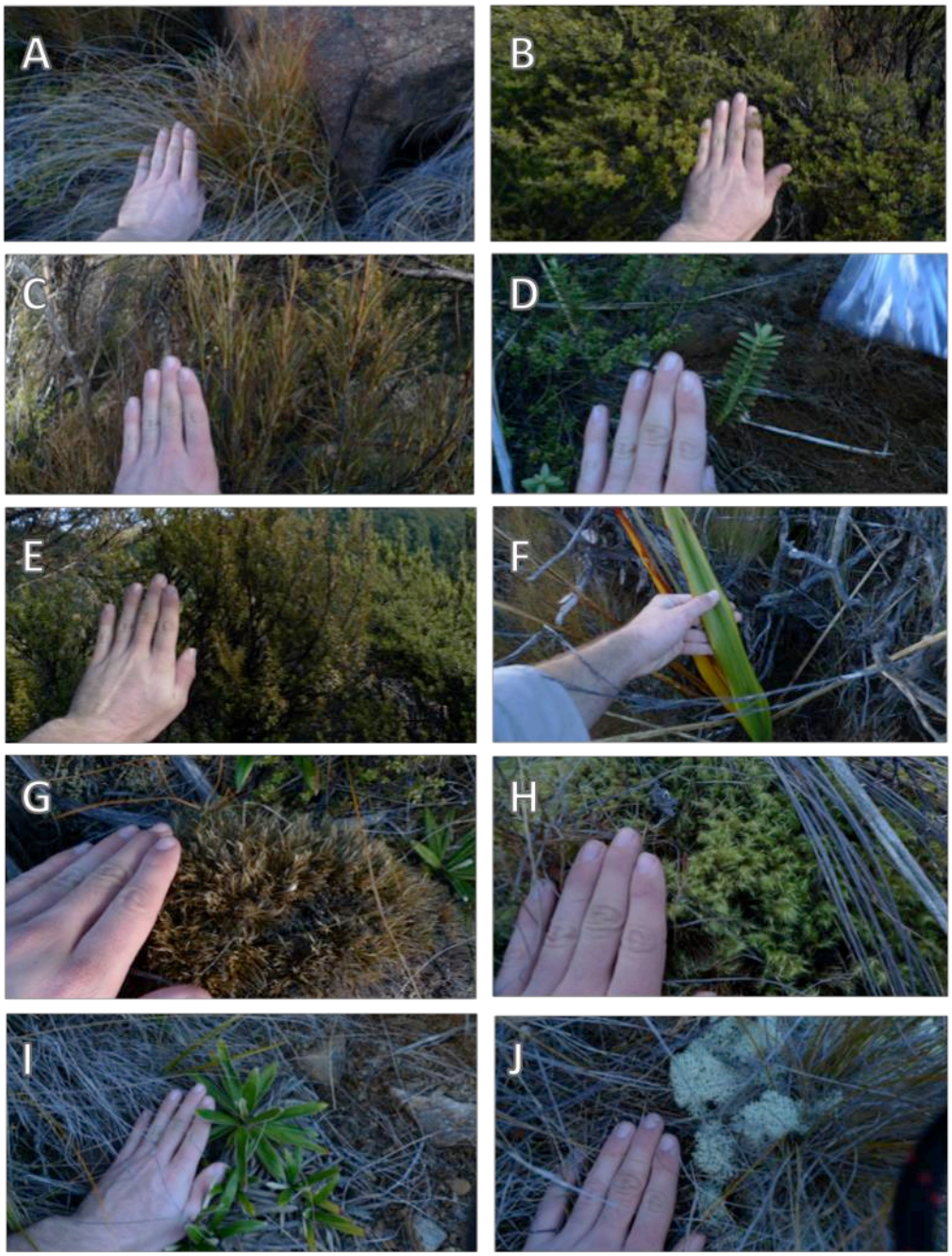

Sample	$\delta^{13}C$ (‰ V-PDB)	Sample	$\delta^{13}C$ (‰ V-PDB)
A	-28.09	F	-25.40
B	-29.94	G	-32.12
C	-29.43	H	-31.42
D	-26.86	I	-30.49
E	-29.76	J	-29.50

Appendix 7: Plant species dominant in the Red Hills, with associated $\delta^{13}C_{CO2}$ values. All species fit within the C_3 plant type, from referenced isotopic values in Sharp (2007).